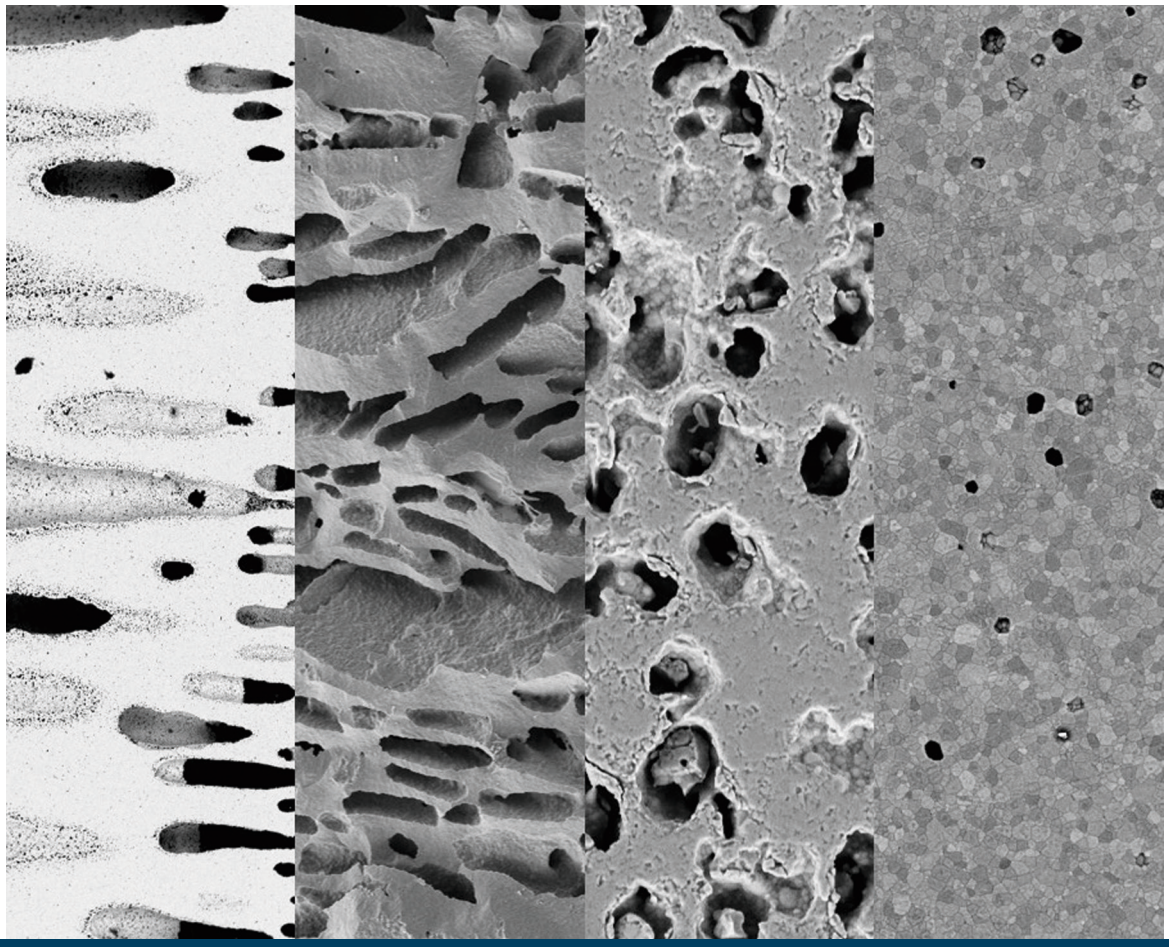

Microstructure and Thermomechanical Properties of $SrTi_{1-x}Fe_xO_{3-\delta}$ Oxygen Transport Membranes and Supports

Rafael Oliveira Silva

Energie & Umwelt / Energy & Environment
Band / Volume 450
ISBN 978-3-95806-381-5

Mitglied der Helmholtz-Gemeinschaft

JÜLICH
Forschungszentrum

Schriften des Forschungszentrums Jülich
Reihe Energie & Umwelt / Energy & Environment Band / Volume 450

Forschungszentrum Jülich GmbH
Institut für Energie- und Klimaforschung
Werkstoffstruktur und -eigenschaften (IEK-2)

Microstructure and Thermomechanical Properties of $SrTi_{1-x}Fe_xO_{3-\delta}$ Oxygen Transport Membranes and Supports

Rafael Oliveira Silva

Schriften des Forschungszentrums Jülich
Reihe Energie & Umwelt / Energy & Environment Band / Volume 450

ISSN 1866-1793 ISBN 978-3-95806-381-5

Bibliografische Information der Deutschen Nationalbibliothek.
Die Deutsche Nationalbibliothek verzeichnet diese Publikation in der
Deutschen Nationalbibliografie; detaillierte Bibliografische Daten
sind im Internet über http://dnb.d-nb.de abrufbar.

Herausgeber und Vertrieb:	Forschungszentrum Jülich GmbH Zentralbibliothek, Verlag 52425 Jülich Tel.: +49 2461 61-5368 Fax: +49 2461 61-6103 zb-publikation@fz-juelich.de www.fz-juelich.de/zb
Umschlaggestaltung:	Grafische Medien, Forschungszentrum Jülich GmbH
Druck:	Grafische Medien, Forschungszentrum Jülich GmbH
Copyright:	Forschungszentrum Jülich 2019

Schriften des Forschungszentrums Jülich
Reihe Energie & Umwelt / Energy & Environment, Band / Volume 450

D 82 (Diss., RWTH Aachen University, 2018)

ISSN 1866-1793
ISBN 978-3-95806-381-5

Vollständig frei verfügbar über das Publikationsportal des Forschungszentrums Jülich (JuSER)
unter www.fz-juelich.de/zb/openaccess.

Contents

CHAPTER 1 Motivation and scope of the work

The increase in energy demand associated with an economy still based on the usage of fossil fuels and derived materials has directed the attention in recent years towards means to reduce CO_2 emissions that are known to be the main reason for current global warming effects. Furthermore, a range of new technologies for large scale and green power supply will require pure oxygen as feed, such as oxy-fuel combustion process and partial oxygen reactors [1, 2]. The aforementioned future energy conversion routes should hence convert natural gas, oil, coal, biomass, or biogas into syngas containing H_2 and CO [3, 4], which is an important input for diverse chemical processes [5, 6]. More important, these new technologies aid the reduction of CO_2 emissions and enable its utilization towards the production of important fuels and chemicals [7-9].

Therefore, usage of ion-conducting membranes emerged as one of the most efficient technologies in this context, since they can combine the separation process of one or more in/output products directly with chemical reactions for syngas production. The process becomes more efficient since it combines the ideal conditions for reaction and separation steps (high temperature and pressure gradients) [10]. Moreover, membrane reactors might offer a large range of applicabilities that goes from the production of chemical commodity chemicals, energy carriers, and synthetic fuels, as illustrated in Figure 1-1.

However, ion-conducting membranes face some challenges to become cost effective and industrially applicable. Dense ceramic membranes for gas separation must fulfill requirements with respect to mechanical and chemical integrity at the required elevated operation temperatures and under oxygen partial pressure gradient exposures and, in addition, with respect to functionality, require high ionic-electronic conductivity. Accordingly, insight into relations among materials properties is essential and criteria for materials selection are desired to aid these upcoming systems.

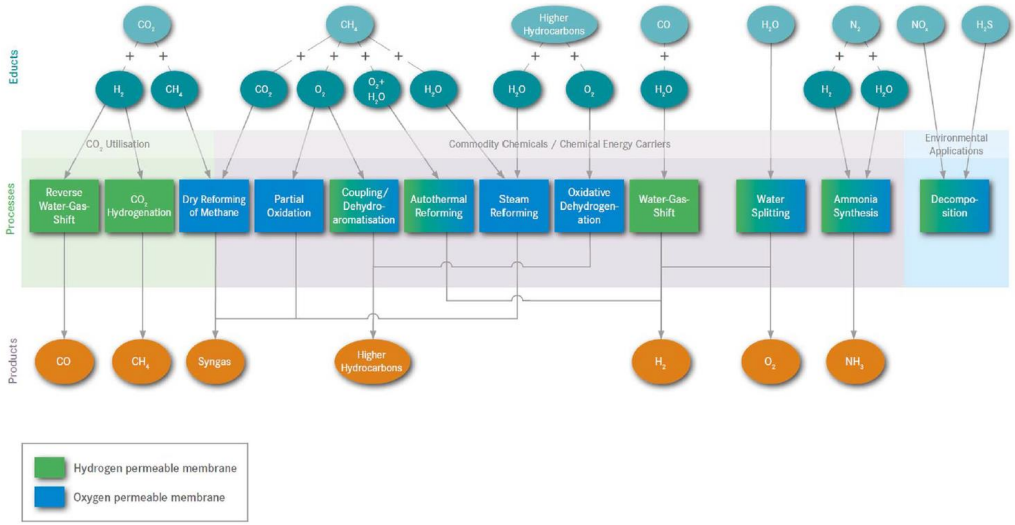

Figure 1-1 – Summary of selected processes where oxygen and hydrogen transport membranes are applicable [10].

Hence, the overall objective of the work is to investigate a promising particular novel materials class as candidate for membranes applications with respect to mechanical and functional properties and its relationship to the materials' microstructures. The studied compositions are based on the system **$SrTi_{1-x}Fe_xO_{3-\delta}$ (STF-X) with x = 0.25, 0.35 and 0.5**. The high stability of the perovskite structure linked with favorable permeation make STF-X compatible candidates for OTM application [11]. In addition to the targeted oxygen permeation flux (at least 1 ml/cm² min [3]), the required stability with respect to mechanical properties is to be achieved by an asymmetric design, where a thin membrane layer is to be supported by a porous substrate. Consequently, this work concentrates on the preparation of dense STF-X materials through industry relevant processes, here solid state-reaction and tape casting for powder and sample manufacturing respectively, and aims towards a systematic mechanical characterization of dense STF-X.

The porous substrate, on the other hand, requires large porosity (above 30% [12]) combined with low tortuosity (minimum gas molecule path). These characteristics, though enhancing the gas transport, limit the mechanical stability. Hence, conventional porous ceramic

manufacturing such as tape casting, which provides a randomly distributed spherical or plate like porosity, may be substituted by advanced techniques such as freeze-drying and phase inversion tape casting. These methods produce bulks with hierarchically aligned channel- and finger-like porosity.

Mechanical characteristics such as elasticity, fracture toughness, and fracture behaviour are fundamental in order to assess the material's functionality and warrant the long-term reliability of the membrane components. Within this frame, also strength degradation, caused by environmentally assisted crack growth, needs to be investigated, since it leads to early failure and reduced lifetime. In addition, mechanical stability at relevant operation temperature has a key function in the membrane application. Accordingly, creep deformation mechanisms that might take place at high temperatures play an important role, since they can compromise the mechanical integrity of the membrane components. Overall, the determination of the mentioned properties aims towards deriving durability and stability limits to adjust the membrane structure regarding process needs.

CHAPTER 2 Fundamentals

This section primarily concentrates on a literature review and relevant theoretical background for the present work. Here, a concerned understanding of the ceramic technology applied to oxygen transport membranes is reported. Therefore, this chapter is divided in three major segments: the first one is addressed to the functionality and application of oxygen transport membranes; the second part focuses on ceramic manufacturing techniques, and the third part relates to the pertinent mechanical characteristics investigated within the framework of this study.

2.1 Oxygen transport membranes

The concept of using ionic conductors for gas separation was introduced more than 30 years ago in works of Cales and Baumard [1, 13, 14], where they anticipated that mixed ionic-electronic conducting oxides could be used as oxygen semi-permeable membranes. Indeed, dense ceramic membranes promise infinite selectivity, if only oxygen diffuses through the structure to the permeate side [1]. The so-called Oxygen Transport Membrane (OTM) technology has therefore emerged, aiming towards higher efficiency than the currently used industrial procedures for oxygen separation, like cryogenic distillation or Pressure Swing Adsorption (PSA) [2, 15].

Contrary to these prevalent methods, the new process is based on gas separation at elevated temperatures delivering high economic viability, which is achieved since the heat that is converted into power in an electricity park may be also used for oxygen separation. Indeed, more than 50% gain in input energy can be obtained by OTM small scale systems to produce the same amount of pure oxygen and energy which a combined PSA and a small power plant, based on natural gas combustion turbines, would produce. A comparison between OTM and PSA is presented in Figure 2-1 [2].

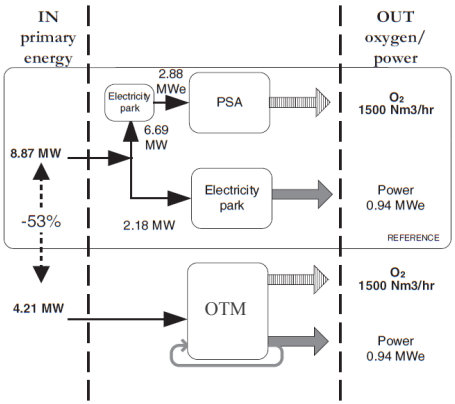

Figure 2-1 - Comparison between PSA and OTM small-scale system for 100% oxygen purity, modified from [2]. The electricity park considered in this comparison is a state-of-the art STAG (steam ang gas turbine).

OTMs are also attractive due to their applicability as membrane reactors for conversion of natural gas or coal into synthetically produced H_2 and CO, i.e. syngas. This product is an important input for the chemical industry, since it can be further transformed into liquid fuels, reducing the usage of oil resources [16, 17]. The use of ceramic membranes offers a better control of the oxygen stream, avoiding total oxidation of the input chemicals, since oxygen can be added to the reaction though the OTM. A schematic membrane reactor and the chemical reactions for syngas production are portrayed in Figure 2-2.

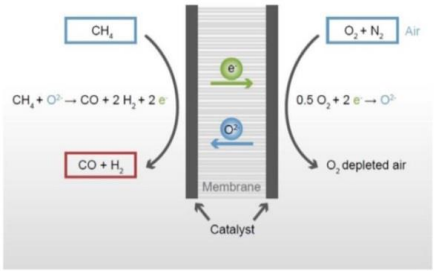

Figure 2-2 – Schematic membrane reactor for syngas production from partial methane oxidation [10].

The challenges in producing a cost effective and reliable membrane are the combination of the following characteristics [1, 18]:

i) High ambipolar conduction.
ii) Chemical, mechanical and structural stability at the process operational conditions.
iii) High catalytic oxygen reduction activity.
iv) Supports with high mechanical strength and sufficient gas transport.
v) Compatibility with other system components.
vi) Easy processing.
vii) Economically viable.

Furthermore, it has been indicated that membranes must withstand a maximal tensile stress of around 30 MPa (conditional to the chosen design), which can be easily reached depending on the gas pressure difference [19] and should also not creep more than 1% per year [20], aiming for sustainable operation. Although great effort has been invested into studies of viable candidates for oxygen transport membranes [1, 5, 10-12, 18, 21-45], not all features discussed above are currently completely fulfilled by the studied materials.

2.1.1 Oxygen transport

The criterion for oxygen separation via mixed ionic-electronic conducting membranes is based on solid diffusion of some ionic specimens through the material. The direct transport of oxygen molecules from one side of the membrane to the other is not possible, since OTMs are gas tight. Still, adsorbed oxygen at the membrane surface is ionized and permeates selectively balanced with a counter flux of electrons, i.e. an internal shortcut. The driving force is a chemical potential that is created if a difference in oxygen partial pressure in the opposite sides of the membrane is present, which establishes the driving force for the oxygen transport. Indeed, a change in oxygen partial pressure establishes an electrochemical potential in the solid that is necessary for creation or annihilation of vacancies [46], which are usually temperature dependent. Thus, the following reaction takes place [46, 47]:

$$\frac{1}{2}O_{2(g)} + V_O^{\cdot\cdot} + 2e' \leftrightarrow O_O^{\times} \tag{2.1}$$

The flux of oxygen transport through a mixed ionic-electronic conductor can be described for low oxygen partial pressure differences using the Wagner equation for diffusion in solids [1]:

$$j_{O_2} = \frac{RT}{16F^2L} \int_{p''_{O_2}}^{p'_{O_2}} \sigma_{amb} d\ln(p_{O_2}) \tag{2.2}$$

where j_{O_2} is the oxygen permeation flux, R the universal gas constant, T the absolute temperature, F the Faraday's constant, L the membrane thickness, p'_{O_2} and p''_{O_2} are the oxygen partial pressures at the feed and permeate side respectively, and σ_{amb} is the ambipolar conductivity of the solid, expressed by:

$$\sigma_{amb} = \frac{\sigma_{electronic} \cdot \sigma_{ionic}}{\sigma_{electronic} + \sigma_{ionic}} \tag{2.3}$$

Single-phase ceramics capable of mixed ionic-electronic conduction usually show defined structures similar or derived from perovskite, fluorite and brownmillerite [34, 48-50]. Among these, significant oxygen permeation rates were observed especially in the case of perovskite-like ceramics at temperatures above 800 °C [51], which led to more attention towards this class of materials. A typical perovskite has the general chemical formula ABO_3, where A and B are cations with distinct sizes. The ideal cubic symmetry structure has the A cation in octahedral coordination, while B is surrounded by an octahedron of oxygen ions in a 6-fold coordination. Such a typical perovskite structure is showed in Figure 2-3.

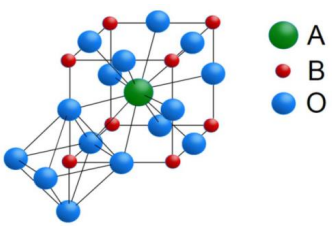

Figure 2-3 - Perovskite structure [52].

The crystal structure of an ABO_3 perovskite alone does not allow oxygen ion conductivity, and doping with cations of different valence and radii at the A side to introduce oxygen vacancies is necessary. Also, the lattice distortion created by this way increases the mobility of ions and vacancies, collaborating for enhanced diffusion. B-site doping, on the other hand, improves the stability of the perovskite structure, leading to $AB_{1-x}M_xO_{3-\delta}$, where δ is the under-stoichiometry of oxygen, i.e. the amount of vacancies influenced by the doping and presence of transition metal cations [53-55]. Some perovskites studied as candidates for oxygen transport membranes may also include doping on the A-site, which increases the ionic conductivity and might improve the physical properties of the structure. Accordingly, the systems $Ba_{1-x}Sr_xCo_{1-y}Fe_yO_{3-\delta}$ and $La_{1-x}Sr_xCo_{1-y}Fe_yO_{3-\delta}$ were studied in great detail regarding their promising application as OTM material [11, 12, 25-27, 32, 36, 38-40, 44, 56-58].

2.1.2 Asymmetric design

Apart from the material's electrical properties, the permeation is governed by process and design parameters: temperature, oxygen partial pressure and membrane geometry (thickness), as indicated by equation (2.2). Accordingly, decreasing the membrane thickness may intensively enhance the gas permeation until a characteristic thickness $> L_c$, at which surface exchange kinetics start to dominate the transport. For this reason, the interfacial oxygen exchange term was introduced later by Bouwmeester et al. into the Wagner equation [59]:

$$j_{O_2} = \frac{1}{(1 + 2L_c/L)} \frac{RT}{16F^2L} \int_{p''_{O_2}}^{p'_{O_2}} \sigma_{amb} d\ln(p_{O_2}) \tag{2.4}$$

where $L_c = D/k$, D is the oxygen diffusion coefficient and k is the surface exchange coefficient. However, a dense thin ceramic oxygen transport membrane (in the range of 10 μm thickness) does not possess the required mechanical properties to withstand the boundary conditions imposed by operational environment and thermo-mechanical loads. Therefore, a high performance membrane relies on an asymmetric design, which consists of a thin dense ceramic layer supported by a porous substrate [60]. An example of asymmetric design is shown below.

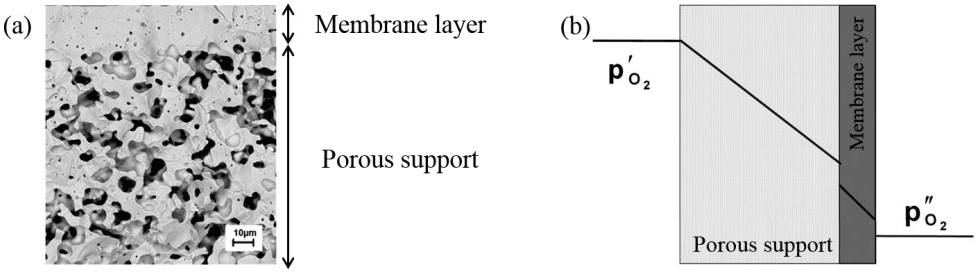

Figure 2-4 – (a) $Ba_{0.5}Sr_{0.5}Co_{0.8}Fe_{0.2}O_{3-\delta}$ asymmetric membrane and (b) driving force drop across an asymmetric membrane, modified from [12].

Asymmetric membranes were investigated with respect to their functionally, which revealed that oxygen permeation is influenced by several limiting mechanisms, such as kinetic of surface exchanges and concentration polarization of the gas in the pores [12, 35, 36, 38, 60]. In such cases, when concentration polarization is present, the driving force at the membrane surface for the permeation is reduced, causing the oxygen flow to decrease. Therefore, to increase the permeation flow in asymmetric membranes, the support should be designed in such way that the pores have a low tortuosity and large diameter, providing optimal gas exchange.

2.1.3 $SrTi_{1-x}Fe_xO_{3-\delta}$

$SrTi_{1-x}Fe_xO_{3-\delta}$ ($0 \leq x \leq 1$) (denoted STF-X in the following) perovskite materials have been studied for application as oxygen sensors and also as possible cathode for oxide fuel cells [61, 62]. Recently they were also considered for usage as a membrane material for gas separation [11]. STF-X compositions can be formed based on solid solution of the two end perovskites $SrTiO_3$ and $SrFeO_3$, while strontium titanate provides high chemical stability with almost insignificant levels of electronic and ionic conductivity, strontium ferrite introduces high values of mixed ionic-electronic conductivity, but with poor chemical stability especially under oxygen partial pressure gradients [63, 64]. In fact, $SrFeO_{3-\delta}$ possesses one of the highest ionic conductivities among the perovskites, with $\sigma_{ionic} \approx 0.2$ S/cm and $\sigma_{electronic} \approx 100$ S/cm at 850 °C [63]. The oxygen non-stoichiometry of $SrFeO_{3-\delta}$ lies within the range of $0 \leq \delta \leq 0.5$ due to variation ratio of Fe^{3+}/Fe^{4+} as function of temperature and oxygen partial pressure. Any change in δ can lead to changes in the crystal structure symmetry, which can cause internal stresses and mechanical instability [65-67].

On the other hand, pure $SrTiO_3$ exists in a perfect cubic perovskite structure with absence of oxygen vacancies. Even with the partial substitution of Ti^{4+} for Fe^{3+} the cubic symmetry in the system $SrTi_{1-x}Fe_xO_{3-\delta}$ can be kept [64, 66, 68-70]. This occurs due to the tetrahedral coordination of Fe^{3+}, which promotes oxygen release from the lattice leading to the formation of oxygen vacancies. In consequence, a higher iron content increases the ionic and electronic conductivity in these systems [63], since an increase in the iron amount is followed by an increase in the concentration of oxygen vacancies ($V_O^{\cdot\cdot}$) and electronic holes $h^{\cdot}$ [62, 69].

However, the chemical stability of the $SrTi_{1-x}Fe_xO_{3-\delta}$ system is reduced in different atmospheres for higher iron contents [11]. The instability can be related to the release of oxygen from the structure and creation of additional oxygen vacancies, resulting in a chemical expansion with increasing temperature. In particular, the dominant mechanisms of mixed conductivity may change with increasing oxygen partial pressure due to electronic and ionic disorders in the oxygen sublattice [63], as illustrated in Figure 2-5. However, no phase transition was observed in tests at distinct oxygen partial pressures and iron contents (x = 0.01, 0.05, 0.1, 0.2, 0.35, 0.5 and 1), which represents an advantage for STF-X as membrane material.

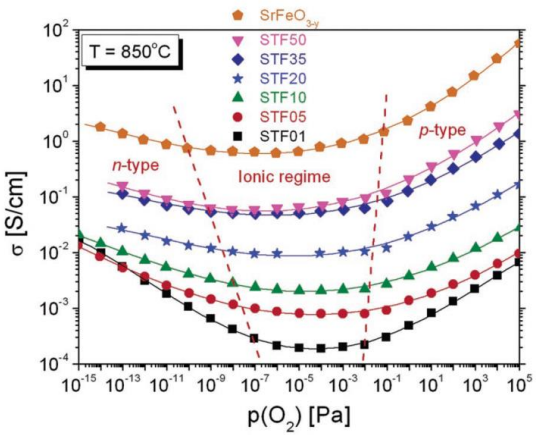

Figure 2-5 - Electrical conductivity at T = 850 °C as a function of oxygen partial pressure for different STF-X compositions [63].

2.2 Manufacturing of ceramic structures

2.2.1 Tape casting

Tape casting is a process frequently used in the fabrication of thin ceramic bodies through depositing a ceramic suspension or slurry onto a carrier material (tape), yielding thicknesses range from 5 μm to 1 mm. The method was introduced more than 70 years ago by Glenn Howatt [71], who patented the manufacturing process of ceramic sheets for capacitors. The technique has then been implemented further and developed in industrial processes, since it has low cost, high productivity and is relatively simple compared to other ceramic processing methods [71].

Currently, tape casting is used in industry to produce multilayered capacitors, piezoelectric components, fuel cells and lithium ion batteries; cases where large, flat and thin ceramic bodies are needed [72]. However, the technique is still in focus of research by many groups that aim towards an optimization in traditional and advanced ceramics production procedures [72, 73]. In addition, compared to dry pressing, tape casting can offer a more homogeneous structure and contribute thereby to an enhanced mechanical strength [72].

The basic principles of the technique are illustrated in Figure 2-6. The process set-up consists of one reservoir, one height adjustable doctor blade, a carrier surface and a drying chamber. With the motion of either the carrier or the doctor blade, a thin slurry film is formed, which consists the green tape after the drying step and, later, the ceramic body after shaping and sintering.

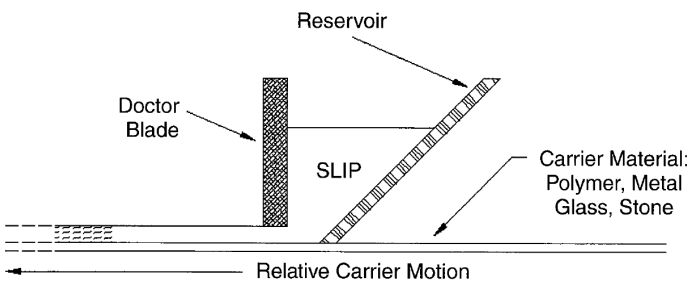

Figure 2-6 – Basic principles of the tape casting process [71].

However, it is the materials selection and slurry composition that predetermines the quality of the green tape. Hence, the chosen binders, plasticizers, solvers and other organic additives in combination with the ceramic powder will contribute to yield a strong and flexible tape. In addition, the organics must be easily and cleanly burned off during the sintering process to facilitate the formation of the ceramic body [71]. To summarize, the following characteristics are indispensable to the tapes [71]:

i) Absence of large defects after drying.
ii) Possibility to further shape and manipulate the green tape, e.g. cutting, stamping, laminating.
iii) Clean burn off of organics at pre-sintering.
iv) Homogeneous microstructure and good mechanical characteristics after sintering.

2.2.2 Ice templating

In recent years, possibility to produce tailored porous ceramics has drawn attention towards the potential application of such structures, since they can combine lightweight, high tolerable strain and their porosity can act as filters or enhance the surface activity [74]. To achieve all these advantages, the amount, size and shape of pores must be controlled [74], and, therefore, in particular the freeze casting technique has become interesting for the development of substrates with hierarchical porosity [30, 74-77].

The process resides on freezing a liquid ceramic suspension and sublimating the solidified phase afterwards under reduced temperature and pressure, followed by sintering to consolidate the ceramic body. The final structure consists of oriented and unidirectional porous channels, which are a copy of the solvent crystals [74]. Indeed, the particles present in the ceramic suspension are rejected from the solidification front to the slurry and accumulate between the growing crystals. Figure 2-7 shows the four steps of the freeze casting process.

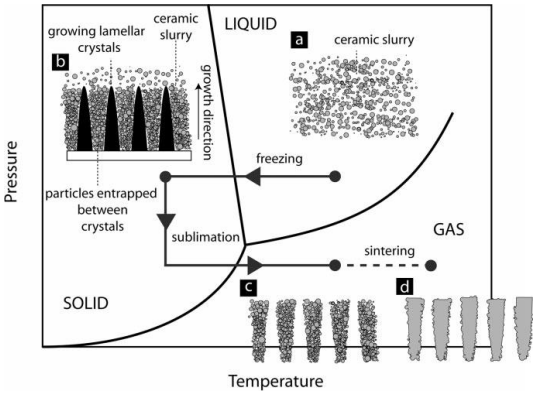

Figure 2-7 - Steps of freeze-casting: slurry preparation, solidification, sublimation and sintering [74].

The first step consists of the ceramic slurry preparation and it doesn't differ very much from other manufacturing techniques in which suspensions are used. The powders must be well dispersed in the solvent to guarantee homogeneity; for this reason, dispersants and plasticizers are often used. Furthermore, binder is also required to give the green body the necessary strength to be handled after the solvent sublimation and before sintering, since the solvent, which also works as structural agent and pore former, is removed later in the process [74, 75].

The slurry is then cooled down in a recipient for solidification. The container must accommodate properly the volume changes when the solvent solidifies (positive in case of water, negative in almost all other systems). In addition, the cooling conditions will determine how the crystals will grow and reject the ceramic particles, therefore, controlling the final structure. Afterwards, the sample is kept at low temperature while the system pressure is reduced, so that the solvent can sublimate. Pores will arise where the solvent crystals existed, remaining a replica of the solidified solvent structure [74].

After the complete solvent removal, the green body is sintered following the characteristic conditions for the used ceramic powder. During sintering, the micro-porosity will be removed, while the obtained channels will remain in the structure. The final microstructure of a sintered freeze-dried specimen can be divided in three distinct zones, as portrayed in Figure 2-8. The first zone is characterized by a rather dense layer obtained in the region closest to the cold source during freezing. Once the ice crystal nucleation begins in this region, the porosity left behind due

to ice sublimation is very fine and may lead to absence of porosity after sintering. In zone 2 a cellular porous structure is observed. The random oriented morphology of the pores portrays the inconsistent movement of the solidification front. At last, the third zone is characterized by a lamellar pore structure, which aligned along the ice growth direction [77]. The pores in this region have low tortuosity, which makes it interesting for application as porous supports for asymmetric membranes.

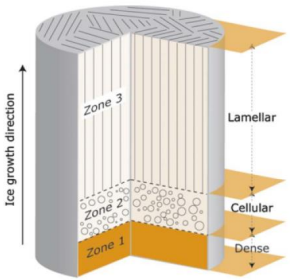

Figure 2-8 - Typical microstructure of an ice-templated sample [77].

A recent study [30] showed that freeze casting can be used to fabricate the substrate in asymmetric membranes with tailored porosity, enhancing their oxygen permeation compared with samples produced by other techniques. Gaudillere et al. [30] reported in their work an oxygen flux of 6.8 $mL \cdot min^{-1} \cdot cm^{-2}$ at 1000 °C for a $La_{0.6}Sr_{0.4}Co_{0.2}Fe_{0.8}O_{3-\delta}$ asymmetric membrane produced by the successive screen printing of a membrane layer on the freeze cast substrate. The result obtained is remarkably higher than previous results for the same material processed by other techniques. Figure 2-9 presents the top view of a $Ba_{0.5}Sr_{0.5}Co_{0.8}Fe_{0.2}O_{3-\delta}$ freeze cast substrate, where oriented pores can be observed.

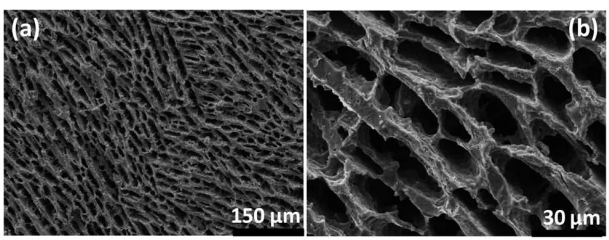

Figure 2-9 – Top view of a disc shaped (Ø 14 × 1 mm²) $Ba_{0.5}Sr_{0.5}Co_{0.8}Fe_{0.2}O_{3-\delta}$ porous support [30].

2.2.3 Phase inversion

The phase inversion tape casting is an adaption from a standard method used to produce asymmetric polymer membranes [78, 79]. The technique is based on a thin film of a polymer solution that enters in contact with a second liquid that cannot solve the polymer, but mix up with the polymer solvent. With the exchange of solvent/non-solvent, an asymmetric structure can be formed at the separation interface. Hence, a fine pored layer is formed at the top of the film, while the bottom layer remain dense. The pore length can be controlled by the bath time, once it achieves the nucleation and growth of the pores [79].

Indeed, a polymeric solution containing ceramic particles can be cast as a temporary substrate and transferred to a bath holding a second non-solvent liquid for the tape formation. Thus, at the bath the mentioned exchange will occur and the solution separates into two phases: polymer-rich and polymer-deficient. The polymer-rich region solidifies into the green tape, which can be afterwards handled to obtain samples through the conventional burning and sintering processes [80, 81]. The formed structure is generally composed of an open porosity gradient (finger-like pores) that decreases until the dense top layer, as presented in Figure 2-10. Such structure favors the surface exchange kinetics, permeation and catalytic reduction activity of oxygen within the membrane [78-80, 82]. Another advantage of the phase inversion technique is that it can also be combined with tape casting for mass production [81].

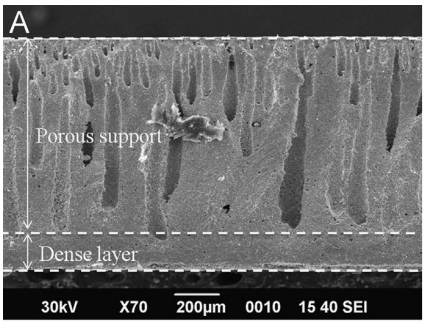

Figure 2-10 - Structure of a YSZ-LSM sample prepared via phase inversion tape casting [80].

2.3 Thermo-mechanical properties of ceramic materials

2.3.1 Elastic behavior

The elastic behavior of a material relates directly to the atomic bond energy and the corresponding deformation represents then the uniform separation among the atoms. Thus, the elastic deformation under an applied stress is directly proportional to the stress, following Hook's law [83]:

$$\sigma = E \cdot \epsilon \tag{2.5}$$

where σ is the normal stress, E the Young's modulus (also called elastic modulus), and ϵ the strain.

In a two phase material, the Young's modulus lies between the high and low-modulus of the constituent phases. In the case of porous materials, the porosity can be considered as a second phase with elastic modulus zero. Therefore, the porosity will always reduce the elastic modulus in the case of a porous material compared to its dense form. Some attempts to evaluate empirically the influence of the porosity on the elastic modulus can be found in the literature [84-90]. For example, Huang et al. [91] investigated the effect of porosity on the elastic modulus for yttrium doped $SrTiO_3$ and suggested as best fit an equation based on the following model [90]:

$$E = E_0 \cdot \exp(-a \cdot P) \tag{2.6}$$

where E is the elastic modulus of a bulk with the porosity P, E_0 is the elastic modulus of this bulk with zero porosity, and a is a constant. In case of [91], E_0 = 230 GPa and a = 4.4.

In addition, the elastic modulus typically tends to decrease slightly and rather linearly with increasing temperature for single crystals and most polycrystalline ceramics [92, 93]. This behavior is expected since the lattice constant increases with the temperature and hence also the distance between the atoms. However, some polycrystalline ceramics show a non-linear decrease of the elastic modulus above a certain temperature attributed to phase transformation, magnetic transitions or grain boundary sliding [92]. The elastic moduli of some membrane materials are summarized in Table 2-1.

Table 2-1 - Elastic moduli of some membrane materials.

Membrane Material	*E* [GPa]	Temperature [°C]	Testing method	Ref.
$Ba_{0.5}Sr_{0.5}Co_{0.8}Fe_{0.2}O_{3-\delta}$ (porosity 5%)	72	RT	Indentation	[94]
	63	RT	Ring-on-ring	
	48	800		
$Ba_{0.5}Sr_{0.5}Co_{0.8}Fe_{0.2}O_{3-\delta}$ (porosity 38%)	38	RT	Microindentation	[40]
	33	RT	Ring-on-ring	
	27	800		
$La_{0.5}Sr_{0.5}Co_{0.5}Fe_{0.5}O_{3-\delta}$	115	RT	Resonance ultrasound spectroscopy	[95]
$La_{0.58}Sr_{0.4}Co_{0.2}Fe_{0.8}O_{3-\delta}$	70	RT	Ring-on-ring	[96]
$SrTiO_3$	225	RT	Nanoindentation	[97]
$SrTi_{0.7}Fe_{0.3}O_{3-\delta}$	164	RT	Microindentation	[98]
$SrTi_{0.5}Fe_{0.5}O_{3-\delta}$	157	RT		
$SrTi_{0.3}Fe_{0.7}O_{3-\delta}$	186	RT		
$SrFeO_3$	171	RT	FP-LMTO*	[99]

*full-potential linear muffin-tin orbital calculation (atomic modelling)

2.3.2 Anelasticity

The classical mechanics describes the properties of solids as analogy to the Hook's law, in which strain is directly proportional to stress and independent of the stress and/or strain rate. However, some materials exhibit a dependence on time for the elastic deformation characterized by a non-instantaneous recovery. This behavior is defined as anelasticity, once it features together solid-like and liquid-like characteristics [83, 100].

Therefore, it is expected for anelastic materials that the strain increases gradually under constant stress flow, while some elastic energy is stored and may recover partially the deformation when the stress is removed. On the other hand, if the strain is kept constant, the stress required to maintain it reduces with time [100]. Furthermore, under periodic stress, anelastic materials show a particular characteristic: the strain will lag in time behind the stress. In other words, for a periodic applied stress varying with a frequency ω, the mechanical response (strain) is delayed by some loss angle θ (see Figure 2-11). Thus, for a periodic stress fluctuating in time t in the form:

$$\sigma = \sigma_0 \sin \omega t \tag{2.7}$$

And the strain is:

$$\varepsilon = \frac{\sigma_0}{E} \sin(\omega t - \theta) \tag{2.8}$$

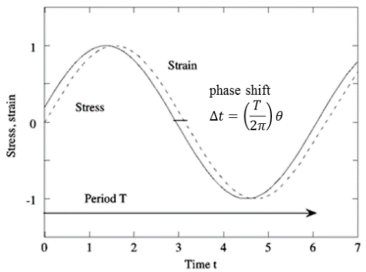

Figure 2-11 - Dynamic loading of a anelastic material: the strain and stress are lagged by a phase shift [101].

Using trigonometry identities, equation (2.8) may be written as:

$$\varepsilon = \frac{\sigma_0}{E} \sin \omega t \cdot \cos \theta - \frac{\sigma_0}{E} \cos \omega t \cdot \sin \theta \tag{2.9}$$

Here we observe that the strain consists of two different components: one in phase with the stress and magnitude $\frac{\sigma_0}{E} \cos \theta$, and the other out of phase with magnitude $\frac{\sigma_0}{E} \sin \theta$. As a result, the dynamic elastic modulus can be written as a complex number:

$$E^* = E_1 + iE_2 \tag{2.10}$$

where $E_1 = \left(\frac{\sigma_0}{\varepsilon}\right) \cos \theta$, which measures the energy stored and recovered in each cycle, and $E_2 = \left(\frac{\sigma_0}{\varepsilon}\right) \sin \theta$, which is also defined as the loss modulus and relates to the energy dissipated per cycle [100]. The ratio of energy lost and recovered per cycle is given by:

$$\frac{E_1}{E_2} = \tan\theta = Q^{-1} \tag{2.11}$$

where $\tan\theta$ is called the loss tangent and related to the internal friction Q^{-1}.

Anelastic behavior in ceramic materials may be caused by different reasons. For glass-ceramic, for instance, at temperatures close to the glass transition, a viscous phase in the vicinity of the crystals is formed and viscoelastic deformation may occur. Anelasticity was also observed in silicate glasses containing one type of alkali at temperatures below the glass transition. For these materials, two mechanical loss peaks ($\tan\theta$) were reported. The first one occurs at -32°C and is assigned to the stress-induced motion of the alkali ions. The second loss peak takes place at 182°C and may be related to non-bridging oxygen ions [83].

Matsuzawa et al. [102] investigated the anelasticity of distinct stabilized zirconia ceramics. The authors suggested that the time-dependent strain behavior of these ceramics may be associated with the concentration of oxygen vacancies, which enable the shift of structural ions when stress is applied. Super-elastic softening caused by anelastic relaxation was also reported for perovskites including $LaAlO_3$, $KMn_{1-x}Ca_xO_3$ and $SrTiO_3$ as function of temperature. Here, the softening originates from the movement of innumerous ferroelastic twin boundaries in reaction to applied stress; also known as ferroelasticity [103, 104].

Although the ferroelastic domain interactions for $SrTiO_3$ are notable at temperatures below 105 K, where a phase transition occurs (tetragonal to cubic) [104], anelastic relaxation was also reported for the range of temperatures between 200-700K [105]. In this case, the relaxation is associated to oxygen vacancy hopping induced by the application of an external stress. Therefore, it can be expected that the elastic energy loss increases with the temperature, once the concentration of oxygen vacancies may also grow. The same effect is also expected under reductive atmospheres, where the understoichiometry of structural oxygen in these materials raises.

However, Cordero et al. [105] suggested that, for a small concentration of dopants substituting Ti (such as Fe_{Ti} causing the formation of V_O), the vacancy hopping may occur at distinct mean rates: Γ_f for sites far away from the dopants and Γ_t close to the dopant. Thus, a jumping V_O may become entrapped by the same structural defect hopping with another rate in the

opposite direction. Consequently, peaks of anelastic relaxation may occur at a range of temperatures related to the distinct types of jumps and their respective mean rates. In addition, recent studies on stress-strain behavior of $SrTiO_3$ single crystals showed that dislocation movement is already identified at low temperatures (in the range between 78 and 1050 K), suggesting a plastic behavior [106]. The existence of plasticity in $SrTiO_3$ single crystals is, however, still not associated with the reported anelastic behavior.

2.3.3 Fracture stress and reliability

The fracture in brittle solids occurs usually once a critical stress is exceeded, which is required to both form and propagate a crack. In other words, the fracture strength of a ceramic body is the stress necessary to separate it in two parts and consequently, create new surfaces. Accordingly, the fracture strength σ_f is expected to be proportional to the surface energy γ of the two new surfaces formed during fracture [83]:

$$\sigma_f \propto 2\gamma \tag{2.12}$$

Flaws inherent to the materials act as stress concentrators and, therefore, limit the strength of brittle materials [107]. For this reason, the strength of brittle materials has a statistical nature and the material's strength depends on the probability that, under an applied stress, a flaw capable of initiating fracture exists. Hence, a rather large scatter of fracture stresses is commonly observed for many ceramic materials.

Granted that, many statistical theories were developed to describe the behavior of fracture in brittle solids [83], the most known and used is the one developed by Weibull based on the existence of a "weakest link" [108]. According to his work, the probability of rupture P_f is a function of stress σ and the volume of the specimen v:

$$P_f = \int_v f(\sigma) dv \tag{2.13}$$

Weibull also assumed for his theory that:

$$f(\sigma) = \left(\frac{\sigma}{\sigma_0}\right)^m \tag{2.14}$$

where σ_0 is a characteristic strength that depends on the best fitting distribution function of the data and m, also called Weibull's modulus, is a constant associated with the specimen's homogeneity. The integration over a volume V_0 under applied load results then in [108]:

$$P_f(V_0) = 1 - exp\left[-\left(\frac{\sigma}{\sigma_0}\right)^m\right] \tag{2.15}$$

Hence, if m tends to zero, the probability of failure will approximate 1 for any value of σ, which means that the material can fail if any stress is applied. On the other hand, if m tends to infinity, the fracture will occur only if σ equals to σ_0. In other words, the Weibull modulus describes the scattering of the fracture stress of a material, i.e. for high Weibull modulus, the fracture stress distribution becomes narrow. In addition, if $\sigma = \sigma_0$, then $P_f(V_0)$ is approximately 0.632, meaning that the so-called characteristic strength σ_0 corresponds to a probability of failure of 63.2%. Moreover, the fracture strength is influenced by the sample's geometry, volume, porosity, method of manufacturing, etc. [83]. For this reason, a comparison among materials must be carried out carefully to avoid misleading conclusions.

The average fracture stress is usually determined by the mean value of the fracture stresses measured for a sample containing a finite number of specimens. In this case, it is suitable to display the uncertainty as a standard deviation of the mean value, which represents the dispersion of the data. On the other hand, the fracture stress can also be arranged in a probability distribution, following equation (2.15). Also, it is possible to estimate an interval, within which the distribution of probabilities is included with a certain confidence level. In other words, this confidence interval consists of an upper and lower bound that limit, with a certain probability (confidence level), the range where the data are included.

In this case, a 95% confidence interval of the probability-failure distributions has a probability of 95% that the real values of the characteristic strength and the Weibull modulus are included between the lower and upper confidence bounds. Accordingly, the confidence interval may be used to describe the experimental uncertainty of the obtained experimental results. The

lower and upper confidence bounds of the characteristic strength, C_l and C_u, respectively are obtained by the equations (2.16) and (2.17) according to DIN EN 843-5 [109]:

$$C_l = \sigma_0 \exp\left(-\frac{t_l}{m}\right) \tag{2.16}$$

$$C_u = \sigma_0 \exp\left(-\frac{t_u}{m}\right) \tag{2.17}$$

where σ_0 is the characteristic strength, m is the Weibull modulus, and t_l and t_u are constants that depend on the chosen confidence interval and number of tested specimens. Similarly, the lower D_l and upper D_u confidence bounds for the Weibull modulus are estimated by equations (2.18) and (2.19):

$$D_l = \frac{m}{l_l} \tag{2.18}$$

$$D_u = \frac{m}{l_u} \tag{2.19}$$

where l_l and l_u are constants. The constants t_l, t_u, l_l, and l_u can be obtained in tables that are included in the standard DIN EN 843-5 [109].

The graphic representation of the confidence interval is done by combining the upper and lower confidence bonds of the characteristic strength and Weibull modulus. This means, the graphic upper confidence bound contains all possible Weibull distributions, where the characteristic strength is equal to C_u and the Weibull modulus is contained in the range from D_L und D_U. The same is done for the lower confidence bound, where the characteristic strength is equal to C_L. A schematic representation of the confidence interval of an arbitrary Weibull distribution is presented in Figure 2-12.

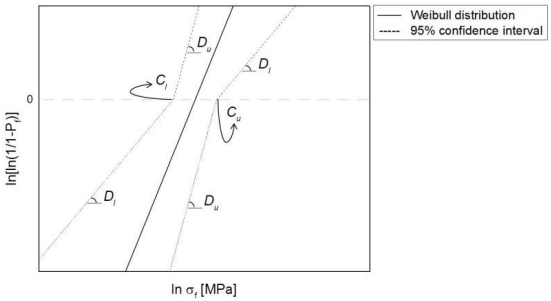

Figure 2-12 - Schematic representation of a 95% confidence interval of an arbitrary Weibull distribution.

The fracture strengths of some membrane materials at room temperature are summarized in Table 2-2. Data on the fracture strength of STF-X ceramics is still not available in the literature, however, for the plastic deformation reported for $SrTiO_3$ single crystals at room temperature, the derived critical flow stress lies between 100 and 120 MPa [106].

Table 2-2 - Fracture strengths of some membrane materials.

Membrane Material	σ_f [MPa]	Test	Temperature	Ref.
$Ba_{0.5}Sr_{0.5}Co_{0.8}Fe_{0.2}O_{3-\delta}$ (porosity 5%)	100	Ring-on-ring	RT	[110]
	79		800	
$Ba_{0.5}Sr_{0.5}Co_{0.8}Fe_{0.2}O_{3-\delta}$ (porosity 38%)	34	Ring-on-ring	RT	[40]
	52		800	
$La_{0.58}Sr_{0.4}Co_{0.2}Fe_{0.8}O_{3-\delta}$	70	Ring-on-ring	RT	[39]
	132		800	

2.3.4 Fracture Toughness

A first attempt to understand the fracture propagation was carried out by Griffith. He considered that the free energy of a cracked body under stress should decrease if the crack grows [107]. Therefore, fracture occurs when the criterion below is satisfied:

$$\sigma_f = \sqrt{\frac{2E\gamma}{\pi c^*}} \tag{2.20}$$

where σ_f the fracture stress, c is half of the crack size, E the elastic modulus, and γ the surface energy. The Griffith's approximation is associated with ideal brittle fracture, in which just the elastic energy and the energy required to create a new surface are involved. However, it has been observed that other forms of energy dissipation can take place during fracture, such as plastic deformation, heat generation, sound emission, or atomic interactions [111]. For this reason, Irwin [83] used a different approach, considering the stress fields in the vicinity of the crack. Hence, for each crack loading mode, there is a stress intensity factor K that indicated the magnitude of the stress close to the crack tip:

$$K_i = \sigma Y \sqrt{c} \tag{2.21}$$

where Y is a dimensionless factor that considers crack geometry and loading mode i (I, II or III as presented in [111]). Generally, brittle ceramic materials fail in loading mode I, and in terms of crack geometries as considered by Griffith, $Y = \sqrt{\pi}$.

Thus, fracture will occur when K_I reaches a critical value called the fracture toughness or K_{IC} and can be assessed by the following equation:

$$K_{IC} = \sigma_f \sqrt{\pi c} \tag{2.22}$$

Therefore, if the fracture toughness of a material is known, the crack size that it can tolerate under a given stress can be calculated. Similarly, the critical flaw size can be derived based on this relation if both fracture toughness and fracture strength are determined beforehand. Table 2-3 summarizes fracture toughness values of some perovskite OTM materials. It can be observed in the results included in Table 2-3 that the fracture toughness of these distinct perovskites are rather low and comparable to highly brittle materials, as soda-lime glass [83].

Table 2-3 – Indentation fracture toughness of some membrane materials.

Membrane Material	K_{IC} [MPa·m$^{1/2}$]	Ref.
$Ba_{0.5}Sr_{0.5}Co_{0.8}Fe_{0.2}O_{3-\delta}$	0.74 ± 0.02	[112]
$La_{0.5}Sr_{0.5}Co_{0.5}Fe_{0.5}O_{3-\delta}$	1.2	[95]
STF0 ($SrTiO_3$)	0.89	[97, 113]
ST30	0.93 ± 0.04	[98]
STF50	0.89 ± 0.02	[98]
STF70	0.95 ± 0.09	[98]

2.3.5 Subcritical crack growth

In some cases a crack can nucleate and grow even under stress levels much lower than predicted by the fracture toughness. Therefore, kinetic phenomena have to be considered in these cases, since it was perceived that a crack can grow assisted by chemical corrosion [111]. Indeed, the crack tip is in constant interaction with the environment and chemical substances can lead to breaking of atomic bonds and propagation of a crack. This phenomenon is called subcritical crack growth (SCG). The correlation between the fracture stress and constant stress rate $\dot{\sigma}$ can be expressed by [114]:

$$\sigma_f = D(\dot{\sigma})^{1/(n+1)} \tag{2.23}$$

where D is a constant and n is the SCG exponent. For this reason, the characteristic fracture strength obtained in a mechanical test is governed by the stress rate used if the material is affected by subcritical crack growth. Executing mechanical tests with distinct stress rates is one direct method to assess the material's sensitivity to subcritical crack growth [114].

Moreover, the investigation of subcritical crack growth aids an estimation of lifetime of ceramic components under a specific load. Therefore, the probability of failure is incorporated together with time dependence and stress in so-called stress-probability-time (SPT) diagrams [115]. An example of a SPT diagram is shown in Figure 2-13, where the lifetime for a membrane

candidate (here $Ba_{0.5}Sr_{0.5}Co_{0.8}Fe_{0.2}O_{3-\delta}$) can be predicted. It can be observed that, to warrant a probability of failure of 1% in 40 years, the applied stress should be below 25 MPa [116].

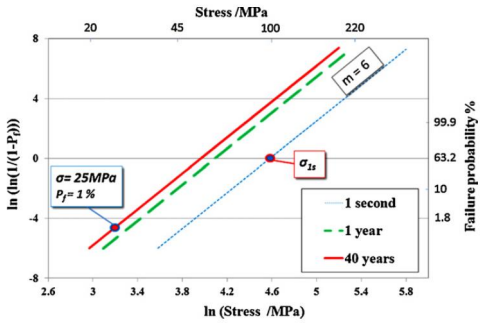

Figure 2-13 - Stress-probability-time diagram for $Ba_{0.5}Sr_{0.5}Co_{0.8}Fe_{0.2}O_{3-\delta}$ [116].

Hence, the lifetime prediction under a static load can be carried out once the fracture strength under dynamic load is converted to an equivalent stress that causes failure under static load. Granted that the characteristic failure strength σ_0, determined under a specific stress rate $\dot{\sigma}$, can be transformed in an equivalent stress, under which failure will occur in 1 second with probability of 63.2% with help of the equation below [115, 117]:

$$\sigma_{1s} = \sigma_0 \left(\frac{\sigma_0}{\dot{\sigma}(n+1)} \right)^{1/n} \tag{2.24}$$

Thus, the SPT diagram can be constructed taking the stress calculated by the equation above as first data point and the slope is then equal to the Weibull modulus. In order to obtain the characteristic strength for distinct times, the following relation can be used:

$$\frac{t_2}{t_1} = \left(\frac{\sigma_1}{\sigma_2} \right)^n \tag{2.25}$$

where σ_i is the characteristic strength in a time t_i (i = 1, 2).

2.3.6 Creep

During the study of the thermo-mechanical properties of oxygen transport membranes, considerable interest is given to creep. This interest relates to the membrane operation conditions that may require temperatures above 800 °C and pressure gradients to increase the oxygen permeation flux. Under these circumstances, the membrane components suffer a continuing irreversible deformation over time (creep), which may damage the structural integrity of the system [24-26, 29, 33, 42, 118, 119]. In this section, the creep mechanisms are revised. Besides, the modeling of creep in porous materials and creep behavior of oxygen transport membranes materials are reviewed.

2.3.6.1 Creep mechanisms

Creep is defined as a slow permanent deformation that occurs in materials submitted to elevated temperatures under an applied stress. The typical creep deformation for ceramic materials occurs in three stages as depicted in Figure 2-14 [83, 111, 120, 121]. In the initial stage, defined as primary or transient creep, the strain rate decreases over time. This phenomenon may arise from changes in the microstructure, for instance, substructure development or increase in the dislocation density, which causes hardening and deaccelerate the deformation rate [111, 120]. Also, at high temperatures, internal stresses may be redistributed, contributing to the slowing effect observed at the initial stage [111].

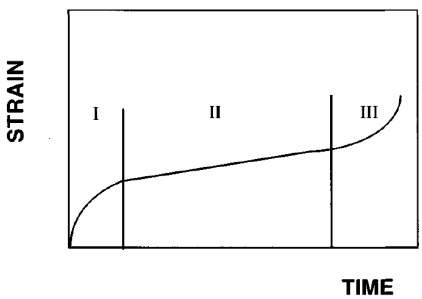

Figure 2-14 - Typical creep curve [111].

The following stage (secondary creep or steady-state creep) is characterized by a linear increase of the strain as function of time. Consequently, the strain rate reaches its minimum and remains constant over time. At this stage, microstructure hardening mechanisms are balanced by softening processes, meaning that creep results from the deformation of an invariable microstructure. In the third and final stage, the deformation rate accelerates rapidly and is associated with the beginning of failure, where cracks initiate and grow.

Although many mechanisms contribute to the plastic deformation at high temperatures and shape the creep curve, more importance has been given to the secondary creep, since it is the stage that takes place for longer time. Indeed, the creep rate on the steady-state creep depends on complex relationship among temperature, applied stress, mobility (diffusion), and microstructure [83]. It has been proposed that the creep rate at this stage may be predicted by [120]:

$$\dot{\varepsilon} = A\left(\frac{1}{d}\right)^{p} \sigma^{n} \exp\left(\frac{-E_a}{RT}\right) \tag{2.26}$$

where A is a dimensionless constant, d the grain size, p and n are the inverse grain size and stress exponents, respectively, E_a is the activation energy, T the temperature, and R is the gas constant.

The proposed mechanisms controlling creep rate in polycrystalline materials may be categorized into lattice and boundary controlled according to Cannon et al. [120]. The lattice mechanisms depend on the intergranular movement of dislocations, once their motion occurs by the jump of atoms into the dislocation line [83, 120]. For this reason, the activation energy relates to the lattice self-diffusion and since these mechanisms are unconnected to the grain boundary, the inverse grain size exponent p is equal to zero, i.e. the strain rate is independent on the grain size. To this category belong dislocation climb or glide and dissolution of dislocation loops.

On the other hand, creep governed by boundary mechanisms involves the presence of grain boundaries. As a result, the alongside grains become dislocated from their original positions relative to each other. The boundary mechanisms differentiate by two types:

i) Grain boundary sliding: grain boundary sliding may arise from the flow of a viscous phase present in the grain boundary or diffusion accommodated by formation of voids in the grain boundaries and folds in triple points.

ii) Mechanisms, at which displacement is followed by grain elongation in the tensile direction: in this case, also referred as diffusional creep, deformation results from diffusional flow of ions from those boundaries where the chemical potential is high (normal compressive stress) to boundaries submitted to normal tensile stresses. The flow is then balanced by a counter-flow of vacancies in the opposite direction, causing grain elongation. This occurs because the concentration of vacancies on the tensile side increases, since the creation of this type of defect reduces the net formation energy, while in the compressive side, the vacancy concentration is reduced.

When diffusional creep takes place, the creep rate is linearly correlated with the stress and, therefore, $n \sim 1$. Nabarro and Herring proposed that if the steady state creep is controlled by the motion of atoms or ions through the lattice, the creep rate may be expressed as [122, 123]:

$$\dot{\varepsilon} = \frac{13.3\Omega D_L \sigma}{kTd^2} \tag{2.27}$$

where Ω is the vacancy concentration and D_L is the lattice diffusivity. If the diffusion occurs at the grain boundaries, the steady-state creep may be estimated by the relationship proposed by Coble [124]:

$$\dot{\varepsilon} = \frac{47\Omega\delta D_G \sigma}{kTd^3} \tag{2.28}$$

where D_G is the diffusivity along the grain boundary and δ is the grain boundary width. A schematic representation of diffusional creep is displayed in Figure 2-15.

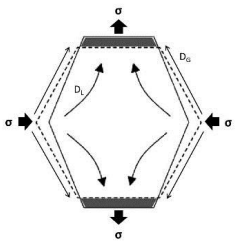

Figure 2-15 – Atoms motion to the grain boundaries with lower chemical potential (tensile stress) and consequent grain elongation; adapted from [125].

The complexity of ceramic materials and their structures restrict the clear designation of the experimentally measured creep parameters to one of the mechanisms discussed in this section. Indeed, the measured creep behavior may be a relationship of the distinct processes and their interaction if more than one mechanism is active. For processes that take place independent and simultaneously, the creep rate will be the sum of all creep rates of each individual mechanism. However, if one mechanism operates considerably faster than the others, than the experimental measured creep parameters are most exclusively related to the fastest mechanism [126]. A summary of the creep parameters and their relation to a controlling creep mechanism is displayed in the Appendix A.

2.3.6.2 Creep behavior for oxygen transport membranes

The creep behavior of oxygen transport membrane candidates has been intensively investigated, since it represents the parameter that defines the lifetime and stability of the membrane components [24-26, 29, 33, 41, 42, 118, 119]. For a high oxygen flux, membrane operation at high temperatures and under oxygen partial pressures is required. Therefore, the membrane material must preserve its structural and geometrical stability over long application time. For example, it has been suggested that, in order to warrant the long term performance, a maximum tolerable creep should not surpass 1% per year [127].

In addition to the parameters discussed in sections 3.1 and 3.2, oxygen partial pressure gradient, which is the driving force for oxygen separation, may also influence the creep rate of the mixed ionic-electronic conductors. Indeed, some oxide stoichiometries show a high dependence on the oxygen partial pressure, since it may govern the equilibrium of defects inward the crystals. Since doping can distort the lattice and disturb the stoichiometry, vacancies can be created as a form to keep electrical neutrality [47]. Oxygen vacancies generated this way are in constant equilibrium with the ambient oxygen partial pressure. For this reason, if the pressure is altered, a new equilibrium in the system is required, reached by creation or annihilation of oxygen vacancies.

Since the alteration in the vacancy concentration may interfere in the molar volume of the crystal structure, direct influence is observed in the case of diffusional creep. It is expected that the raise in the oxygen vacancy concentration will increase the lattice parameter (chemical expansion), and consequently increase creep rates at the stationary state, where a cation

interstitial diffusion might be possible [128]. The effect of the oxygen partial pressure on the creep mechanism can be analyzed for a given microstructure using the following relationship [129]:

$$\dot{\varepsilon} = A(P_{O_2})^m \sigma^n \exp\left(-\frac{E_a}{RT}\right) \tag{2.29}$$

where P_{O_2} is the oxygen partial pressure and m is its exponent. The term $(P_{O_2})^m$ in the equation (2.29) is associated to the influence on the auto-diffusion coefficient for oxides and represents here the chemical activity of oxygen.

Creep studies on the reference OTM material $Ba_{0.5}Sr_{0.5}Co_{0.2}Fe_{0.8}O_{3-\delta}$ (BSCF) were carefully conducted under distinct compressive loads and in different atmospheres [26, 130]. According to the experimental results, BSCF undergoes diffusional creep and the dominating mechanism was attributed to be lattice cation diffusion. Moreover, under decreased oxygen partial pressure the BSCF's creep rate is one order of magnitude higher than as measured in air and, for the fitted experimental studies, m is equal to 0.63. Higher creep rates were also reported for $La_{0.58}Sr_{0.4}Co_{0.2}Fe_{0.8}O_{3-\delta}$ (LSCF) under reduced oxygen partial pressures [118]. Furthermore, due to a phase transition, the activation energy for LSCF increases from 80 kJ/mol at 800 °C to approximately 480 kJ/mol at 850 °C, while the stress exponent remains constant.

Ten Donkelaar et al. [42] studied the compressive creep behavior of STF-X (x = 0.3, 0.5, and 0.7) in a temperature range of 850 – 900 °C and stresses from 30 to 63 MPa. Creep in these materials is reported to be mainly governed by cation diffusion, although stresses exponents from between 2 and 3 were also experimentally obtained for STF30. This may indicate that dislocations movement may have a role on the creep mechanism of STF-X compositions containing less amount of iron. Unlike LSCF, STF-X remains structurally stable and only a cubic perovskite phase is found in the materials before and after creep tests. The creep rates investigated for STF-30 and STF-50 compositions in air and under vacuum [42, 98], indicated a small dependence on the oxygen partial pressure, confirming the oxygen vacancy concentration stability proposed by Rothschild et al. [63].

Literature data on steady-state creep at 30 MPa of distinct oxygen transport membrane candidates is summarized in Figure 2-16. It can be observed that the creep rates of the studied

structures surpass the 1% strain per year limitation highlighted above. Therefore, new materials that present a higher resistance to creep in addition to the required functional properties are necessary.

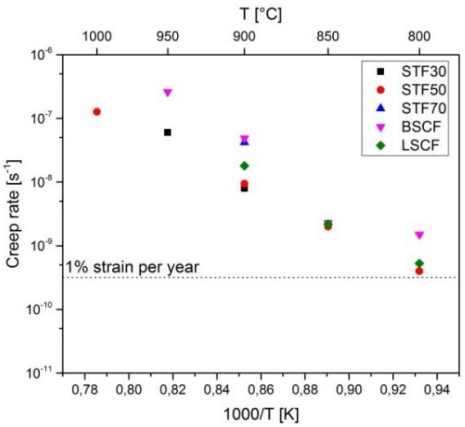

Figure 2-16 – Creep rates at 30 MPa of different oxygen transport membrane candidates [24, 26, 42, 118].

CHAPTER 3 Experimental

3.1 Powder synthesis

The method chosen for the powder preparation was solid state reaction; first, since it is a relatively simple process for large scale production of oxides and second, since it does not require expensive and/or toxic precursors. For each desired composition, the amount of former oxides was calculated to obtain a stoichiometric composition. The materials information and the amount of each precursor are presented in Table 3-1and Table 3-2.

Table 3-1 - Precursors information.

	Company	Particle Size	Assay
SrO	Alfa Aesar	< 150 μm	> 90%*
TiO_2	VWR Chemicals	Not specified	99.4%
Fe_2O_3	Sigma Aldrich	< 5 μm	≥ 99%

*may contain $Sr(OH)_2$ as impurity (< 10%).

Table 3-2 - Powder synthesis precursors for 500g of STF-X powder.

	$SrTi_{0.75}Fe_{0.25}O_{3-\delta}$	$SrTi_{0.65}Fe_{0.35}O_{3-\delta}$	$SrTi_{0.5}Fe_{0.5}O_{3-\delta}$
SrO	279.32 g	278.12 g	276.36 g
TiO_2	161.52 g	139.39 g	106.55 g
Fe_2O_3	53.81 g	75.01 g	106.47 g
Ethanol	494.65 g	492.52 g	489.38 g

The listed components were mixed in a polyethylene jar containing a number of zirconia milling balls (diameter 5 mm) equal three times the weight of solids. The content was then milled for 24 hours at the speed of 120 rotations per minute. Afterwards, the formed slurry was dried and sieved in a 1 mm mesh.

The dried powders were calcined at 1100 ºC for 5 hours; the heating and cooling rates used were 5 K/min. After that, the obtained powders were then comminuted and sieved in a 400 μm mesh and then wet milled in ethanol for 72 hours (proportion powder/ethanol/milling balls

equal to 1:1:2). Furthermore, the powders were characterized concerning their crystallographic phases, morphology and sintering behavior. The methods used to evaluate the powder properties are described in section 3.3.

3.2 Samples Manufacturing

3.2.1 Tape Casting

The tape casting process was used in order to produce specimens for mechanical characterization of STF-X materials. The slurries for the tape casting were prepared according to the desired composition and porosity, as summarized in Table 3-3. In these compositions, ethanol and methyl-ethyl-ketone (MEK) were used as solvent in the volume proportion 34:66. Nuosperse FX9086 was used as dispersant, while corn starch worked as pore former for the desired porous samples. Polyvinyl butyral 98 (PVB 98) was used as binder and S-2075 and polyethylene glycol 400 (PEG-400) were applied as lubricant and plasticizer, respectively.

Table 3-3 – STF-X tape compositions

	Materials	**$SrTi_{0.75}Fe_{0.25}O_3$ dense (g)**	**$SrTi_{0.75}Fe_{0.25}O_3$ porous (g)**	**$SrTi_{0.65}Fe_{0.35}O_3$ (g)**	**$SrTi_{0.50}Fe_{0.50}O_3$ (g)**
1st Part	Ceramic powders	100.00	100.00	100.00	100.00
	Ethanol	12.75	13.50	12.75	12.04
	MEK	23.78	26.21	23.78	23.37
	Corn starch	-	30.00	-	-
	Nuosperse FX9086	3.00	3.00	3.00	3.00
	ZrO_2 milling balls (Ø5 mm)	50.00	50.00	50.00	50.00
2nd Part	S-2075	6.00	8.00	6.00	8.00
	PEG-400	3.00	6.00	3.00	6.00
	PVB 98	7.00	8.00	7.00	8.00

For all tapes, components of this first portion were mixed together in plastic bottle type containments for 24 hours in a tumble mixer. Afterwards, the materials of the second portion were added and mixed once more in the tumble mixer for more 24 hours. Then the slurries were removed from the mixer and left in repose for 48 hours, so that air bubbles incorporated during the procedure could rise to the surface.

After this resting time, the slurries were placed in a vacuum chamber, at 200 mbar for 10 minutes, for degasification. Then, the suspensions were cast with the aid of a Doctor Blade equipment upon a polyester film (mylar) with an opening of 3 mm. The tapes were then dried in air and at room temperature for 3 days. Afterwards, samples were sintered at temperatures selected on the basis of the dilatometry tests described in section 3.3.4. The selection criterion was the temperature at which the dilatometry specimen reached its maximum densification rate. The dwell time, on the other hand, was chosen to obtain a dense microstructure after sintering. The sintering parameters are summarized in Table 3-4.

Table 3-4 – STF-X sintering parameters.

Material	Sintering temperature [°C]	Dwell time
STF25 (dense)	1400	5 h
STF25 (porous)	1300	5 h
STF35	1300	30 min
STF50	1250	3 h

Dense and porous tape cast specimens were produced in order to investigate the mechanical properties (elasticity, fracture toughness and fracture stress) as a function of the composition, i.e. iron doping, and porosity effects. The influence of subcritical crack growth on the long-term reliability of these materials was also assessed. Furthermore, elasticity and fracture stress at relevant operation temperatures was investigated for dense tape cast STF25 specimens.

3.2.2 Freeze Drying

In the current work, slurries for freeze drying were prepared via mixing 21.67 g of solvent (water) and 1.00 g of binder (PEG 4000) in a planetary mixer at 1500 rpm for 2 minutes. Afterwards 0.80 g of dispersant (Dolapix CE64) was added and mixed again in the planetary mixer for additionally 2 min at 1500 rpm. Finally, 40.00 g of STF25 powder was added and mixed for 4 min at 1500 rpm for fully dispersion.

The slurry was cast in cylindrical copper/Teflon® molds, which bottom was immersed in liquid nitrogen for freezing. The used mold is illustrated in Figure 3-1. The mold design creates a temperature gradient, which causes the slurry to freeze in one direction, allowing the ice crystals to nucleate at the bottom and grow to the top. After freezing, the molds were taken to a vacuum

chamber where they remained under 1 mbar for 24 h at -22°C, allowing the solvent to sublimate. Afterwards, the vacuum chamber temperature was increased to 30°C to permit evaporation of the remaining solvent. The green specimens were sintered at 1300°C for 5 h, heating and cooling rates were 1 K/min, respectively. After that, the samples were characterized via scanning electronic microscopy and the open porosity was estimated using Archimedes method.

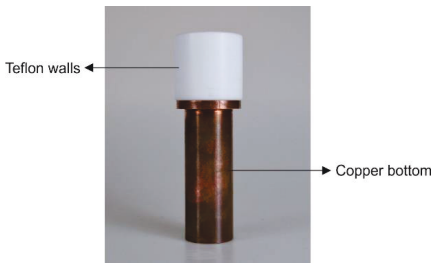

Figure 3-1 - Freeze drying molds.

For the mechanical characterization, the specimens were cut into small bars (6 × 6 × 4 mm^3) via water beam cutting. A schematic representation of the sample's machining is given in Figure 3-2. In addition, mercury intrusion porosimetry (Fisions Instruments, Pascal 440) was conducted on the machined samples in order to characterize pore size and distribution. The specimens for flexural tests were, on the other hand, prepared by grinding the surfaces of the as-received samples in order to minimize roughness and gradient of porosity.

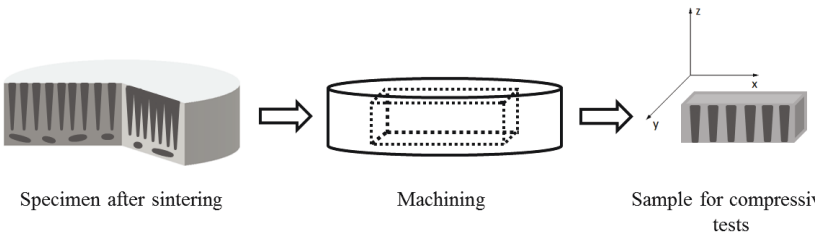

Figure 3-2 - Schematic representation of the sample's machining and the selected directions for the mechanical tests, here represented as a coordinate system.

3.2.3 Phase inversion casting

First, STF25 powder was dispersed in N-Methyl-2-pyrrolidone (NMP) for 48 hours in a volumetric balloon with help of a mechanical stirrer in the weight ratio 10:4.25. Afterwards, grinded polyethersulfone (PES) was added to the mixture in the ratio 1:10 in relation to the ceramic powders and mixed for another 24 hours. The slurry was cast with help of a Doctor Blade with an opening of 2 mm on glass plates and then immersed in water bath for 24 hours, so the phase inversion process could take place.

After that, specimens were punched out of the green tape and sintered at 1300°C for 5 hours. Heating and cooling rates were 1 K/min. The specimens were characterized according to their pore structure via laser scanning confocal microscopy and SEM. Elastic modulus and average fracture stress were assessed via ring-on-ring bending tests.

3.3 Powder and specimen characterization methods

3.3.1 X-ray diffraction

X-ray diffraction is a phenomenon by which the atoms of a crystal, due to their uniform spacing, cause an interference pattern in X-ray propagating waves. This technique can be used to determine the crystallographic structure of a material, once the atoms make the incident X-ray beam diffract in distinct but specific directions. In other words, every atom linearly ordered in the crystal structure act as reflection center for the incident X-ray waves, where the interaction of the incident X-ray produces a constructive interference once the condition below is satisfied:

$$n\lambda = 2d \cdot \sin\theta \tag{3.1}$$

where n is an integer number and represents the order of reflection, λ is the x-ray wave length, d is the distance between 2 piled atomic plans, and θ is the reflection angle [131]. Equation (3.1) means that for a crystal with an inter-planar spacing d and for a determined wave length λ, the reflection will occur only for precise values of θ. In any other angle, the reflection is very poor due to negative interference among the waves. By scanning a crystal through X-ray in a range of angles, it is possible to acquire all diffraction directions that satisfy equation (3.1) and obtain the set of *d*-spacings, allowing an identification of the crystalline structure.

X-ray diffraction was used in the current work to evaluate the crystalline structure of the manufactured STF-X powders, as well as the lattice parameters. The obtained data were compared to X-ray diffraction patterns of pure $SrTiO_3$, which has similar structure to the studied materials. The equipment used for X-ray diffraction is from the company Bruker AXS, type D4 Endeavour, and uses a Cu-K_α X-ray generator.

3.3.2 Laser diffraction

The laser diffraction is used to determine the distribution of particle sizes of a powder. The method is based on the diffraction of an incident light beam by the dispersed particles in a medium, since light is diffracted in different angles according to the particle size. Large particles tend to diffract the light in small angles, whereas small particles diffract the light at higher angles. The intensity and angular diffraction spectrum obtained by scanning the sample through laser are used to determine the particle size distribution according to the Mie's theory and Fraunhofer's approximation for light scattering [132].

The particle size analysis was conducted during the milling procedure described in section 3.1, at which samples of the slurry were removed occasionally to evaluate the average particle size and its distribution as a function of time. For this analysis the D_{90}, D_{50}, and D_{10} are important properties of the powder, since they represent the particle size below which 90, 50 or 10% of the population is located, respectively. The measurement was done in an equipment of the company Horiba, type LA950V2, and permits to identify particles in the range from 0.1 to 3000 μm.

3.3.3 Brunauer-Emmett-Teller method for surface area determination

The Brunauer-Emmett-Teller (BET) theory describes the physical adsorption of gas molecules into a solid surface and can be used to measure the surface area of a material [133]. Accordingly, the physical adsorption is related to the weak interaction forces between adsorbate (gas molecules) and adsorbent (material's surface) and the volume of adsorbed gas is a function of the pressure variations due to the adsorption processes. The volume of adsorbed gas on the material's surface is used to estimate its specific surface area.

For this procedure, pure nitrogen is usually used due its limited interaction with most solids and also because it is inert. The determination of a powder's specific surface area is done

by physio-adsorption of nitrogen at its condensation temperature (77 K) in order to obtain detectable amounts of gas adsorption. The specific surface area was obtained for STF-X powders by the BET method using a device from the company Ströhlein, type AreaMeter.

3.3.4 Dilatometry

The dilatometric analysis was carried out in order to investigate the behaviour of STF-X compacts during sintering. For this method, small pellets (diameter 8 mm, height approximately 10 mm) were uniaxially pressed under 20 MPa for 1 minute. The samples were heated up in a dilatometer (Netzsch, DIL 402 C) at the rate of 1 K/min from room temperature to 1400 °C followed by a hold time of 3 hours. The specimen's linear displacement is measured by an inductive sensor coupled with the specimen's surface. The linear expansion and shrinkage as function of the temperature $\varepsilon(T)$ is determined by:

$$\varepsilon(T) = \frac{l(T) - l_0}{l_0} \tag{3.2}$$

where $l(T)$ is the specimen's length in function of temperature and l_0 the specimen's initial length.

3.3.5 Mercury intrusion porosimetry

Mercury intrusion porosimetry enables the determination of the pore diameter distribution based on the pressure/volume variation during penetration of a porous material by mercury. Since mercury has very low wettability in relation to most of the materials, it does not penetrate spontaneously in open voids or pores unless a pressure is applied to it. The pore radius r_p can be estimated by the following relationship:

$$r_p = \frac{2\sigma \cdot \cos\gamma}{p} \tag{3.3}$$

where σ is the mercury surface tension, γ is the contact angle between material and mercury and p is the applied pressure. The method was carried out in a device from Fisions Instruments (Pascal 440) and measures the equivalent pore radius of the porous specimens.

3.3.6 Confocal laser scanning microscopy

The confocal microscopy is utilized to enhance the contrast of a microscopic image and build up three-dimensional images. Due to the use of a pinhole, a high resolution in planes that are thicker than the focal plane can be realized. In a confocal laser scanning microscope, a laser is used as light source and is focused by a scanner, line by line, in the specimen's surface. The laser as light source has the advantage of being monochromatic, coherent, concentrated, and intense, permitting a high resolution.

The optical mechanism of a confocal laser microscope works with a pair of lenses, where the specimen is placed on the focus of the closest objective and the image is formed in the focal point of the other, as represented in Figure 3-3. Therefore, only a small portion localized on the focal point of the closest objective is captured, achieved by the use of a pinhole. A control in vertical axis allows the acquisition of images in distinct sections and, with this, high resolution images of piled-up focal planes can be obtained and used to reconstruct the three-dimensional topography of the sample.

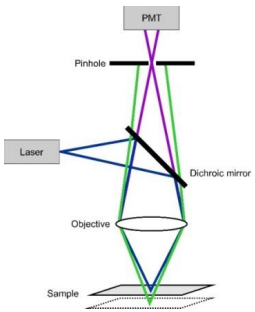

Figure 3-3 - Schematic representation of a confocal laser scanning microscope, modified from [134].

Due to the advantage of acquiring images on very irregular surfaces, confocal laser electronic microscopy (Keyence, VK-9700K) was used to investigate the fracture surface of the produced specimens, especially after the mechanical tests. An imaging software (VK-Viewer) was used to reconstruct the three-dimensional topography of these specimens.

3.3.7 Scanning electron microscopy

A scanning electron microscope (SEM) is a type of electron microscope capable of producing high resolution images of a specimen's surface by scanning it with a focused electron beam. Due to the way the images are created and captured, SEM images have usually a three-dimensional aspect and reveal information about the superficial structure of the investigated sample, i.e. high depth of field. The electron beam is generated by a cathode and accelerated through an anode. Magnetic lenses are used to focus the created electron beam on the sample's surface. The SEM also has distinct detectors that are responsible to detect the different signals generated by the interaction electrons/sample.

The interaction of a fine electron beam focused upon the specimen's surface generates a series of signals that may be used to characterize the sample's properties, such as composition, topography, crystallography, etc. The most important signals are related usually to images of secondary electrons, backscattered electrons, and characteristic X-rays. In addition, the complete orientation of each single crystal of a polycrystalline material can be obtained by the electron backscattered diffraction technique (EBSD). This method is based on the diffraction of a high-energy electron beams by the single crystals in all possible directions within the specimen. Some of the diffracted electrons that have virtually the same initial energy of the beam can be detected and used to generate an EBSD pattern. These patterns can be categorized according to the materials and allow the investigation of crystal orientation, texture, grain size/grain boundary characterization, etc.

The scanning electron microscopy is used to study and evaluate the microstructure of the materials produced via the distinct manufacturing procedures described in section 3.2. The analysis of cross-sections was conducted on samples prepared by ceramography. For that, the specimens were embedded in epoxy resin, grinded with silicon carbide abrasive paper and polished with diamond suspensions. For the grain size analysis, the specimens were chemically etched for 10 seconds in a 75 mL H_2O / 5 mL HCl / 2 mL HF solution. The microstructure analysis was conducted in scanning electron microscopes from the company Zeiss, types Merlin and SUPRA 50VP.

3.3.8 Microstructure analysis

The graphic analysis of grain size, porosity and pore size was conducted with the aid of the imaging software AnalySIS Pro ®. The average grain size was estimated from the obtained SEM images based on the circular intercept segment method recommended by ISO 14250:2000 [135] and the results are displayed as an equivalent circular diameter (ECD). In this case, the ECD represents the diameter of a circle with the same area as the measured particle. Porosity was measured by setting the threshold values of contrast in order to identify the pores on the image and dividing the occupied image area by pores by the total image area. Pore average size, width, length, and aspect ratio of hierarchically porous specimens were obtained by the detection method of the software set with the same threshold values mentioned before. The software ImageJ was used to estimate the pore wall thickness of freeze-dried specimens by the local thickness filter available in the software tools.

3.4 Mechanical characterization

3.4.1 Depth-sensitive indentation

The indentation technique can be used to evaluate hardness, elasticity and fracture toughness of materials. The currently used equipment permits to assess the depth of penetration of an indenter (in this work diamond square pyramidal Vickers and triangular pyramidal Berkovich) as a function of the applied load, yielding elastic modulus and hardness [115]. The indenter tip loads the specimen's surface resulting in elastic-plastic deformation followed by an elastic unloading, see Figure 3-4.

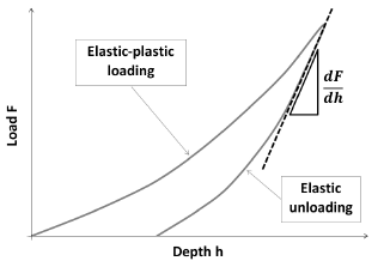

Figure 3-4 - Schematic load-displacement curve for a Vickers' depth-sensitive test.

Thus the unloading stage can be used to estimate the elastic modulus of the material according to the following equation [136]:

$$E_r = \frac{dF}{dh} \cdot \frac{1}{2} \cdot \sqrt{\frac{\pi}{A}} \tag{3.4}$$

where dF and dh are the difference in the force applied and depth, respectively, during the elastic unloading, and A is the contact area. The above equation includes the elastic moduli of the specimen material and the indenter, which also experiences elastic deformation during the experiment. Thus, the sample's elastic modulus E_{IT} can be estimated using the relation:

$$\frac{1}{E_r} = \frac{1-\nu^2}{E_{IT}} + \frac{1-\nu_i^2}{E_i} \tag{3.5}$$

where ν and ν_i are the Poisson ratios of specimen and indenter tip, respectively. The indentation hardness H_{IT} is estimated according to the following relationship [137]:

$$H_{IT} = 1.8544 \frac{P_{max}}{d^2} \tag{3.6}$$

where P_{max} is the maximum load and d^2 is the imprint's diagonal length.

Depth sensitive nano-indentation

The depth-sensitive nano-indentation can be used to investigate the mechanical properties, such as elasticity and hardness, in small volumes one of a material, a method that is being widely applied to determine the properties of thin films, coatings and superficial layers. Due to the very small tested material volume, it is possible to map the spatial distribution of the surface mechanical properties with high resolution. Similar to the micro-indentation technique introduced below, the nano-indenter applies a load to a diamond tip with a determined geometry onto the material's surface. Based on the penetration depth as a function of loading/unloading, the elastic modulus can be obtained.

In the current work, the experiments were conducted on the same specimens used for depth-sensitive micro-indentation. The used equipment is a nano-indenter from the company CSM Instruments with a Berkovich tip. In essence, 20 indentations were performed per specimen with a continuous multicycle mode, i.e. 10 loading/unloading cycles, where the maximum load increases linearly at each cycle. For that, the maximum applied load at the first cycle and at last cycle were 5 mN and 50 mN, respectively, with partial unloading down to 5% of the maximum load in each cycle. For very small loads, the influence of the materials flaws, such as porosity, inclusions, impurities, etc. may be avoided, deriving mechanical properties tending towards the single crystal properties [138]. The maximum elastic moduli obtained with this technique (single indentation) are assumed to be the property of the pure material and are used to evaluate the influence of iron doping on the elastic properties of STF-X compositions. Also, for this purpose, the Poisson ratio for all compositions was considered to be equal to 0.232, see pure $SrTiO_3$ [97].

Depth-sensitive micro-indentation

For the micro-indentation tests, one sample of each tape of dense STF-X was grinded and polished with diamond suspensions. The polished surface must be flat and parallel to achieve the best experimental precision. The elastic modulus and indentation hardness were measured (Fischer HC100) with a Vicker's diamond tip and load of 1N within a matrix of 8 × 3 indentation points in tape cast STF-X specimens. The fracture toughness can be estimated from the size of cracks induced by the indentation test, i.e. when the applied loads/stresses are large enough to initiate and propagate cracks. Figure 3-5 is a schematic representation of the geometry of indentation cracks.

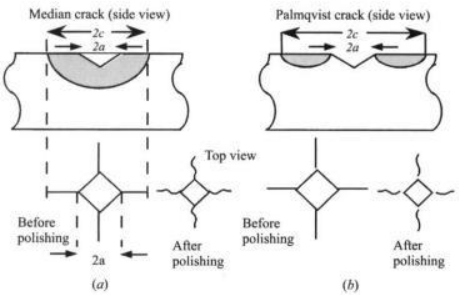

Figure 3-5 - Schematic of cracks introduced during the Vicker's indentation test: (a) median crack and (b) Palmqvist crack [115].

If a and c can be measured, then the fracture toughness for well-developed median crack patterns ($c \geq 2a$) can be estimated by the empirical equation [139]:

$$K_{IC} = 0.016 \cdot \left(\frac{E}{H}\right)^{1/2} \cdot \left(\frac{P}{c^{3/2}}\right) \tag{3.7}$$

where E is the Young's modulus and H the indentation hardness of the material, P the indentation load, and c the crack length. Even though has been discussed as not reliable for absolute values once the crack system induced by indentation is complex and has considerable residual stresses [140], it was used in the current work due to compare the material's behaviour and relate to reference values from literature.

The fracture toughness was estimated from the size of cracks induced by the indentation test at an applied load of 3 N (Micromet, Buehler LTD.). Here, the 3 N load is utilized once it is large enough to initiate and propagate median cracks. In particular the equation proposed by Anstis [139] (equation (3.7)), boundary conditions for radial crack type were satisfied in all cases) was used in the fracture toughness determination of STF-X materials in the literature [97, 98, 113] and, for better comparison, the same relationship was applied in the present work.

3.4.2 Ring-on-ring bending tests

The ring-on-ring test is a bending experiment used in the current work to derive elastic modulus, fracture strength, and reliability of the investigated materials, as well as to assess the sensitivity of the materials with respect to subcritical critical growth. The test set-up is presented in Figure 3-6. The experiments were performed in an electromechanical machine (INSTRON 1362) with a 1000 N load cell (Lebow) and the sample's displacement during the test was measured with a ceramic extension rod connected to a linear variable differential transformer (Solartron Metrology).

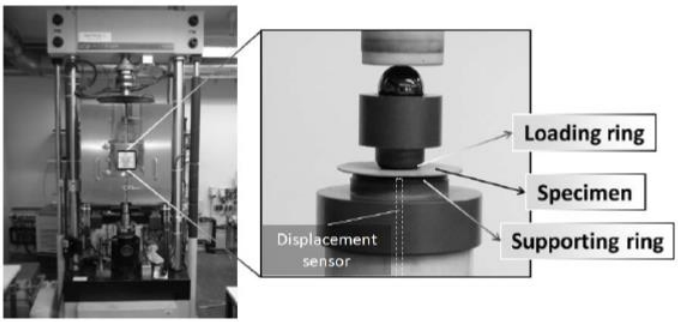

Figure 3-6 - Ring-on-ring test set-up in IEK-2.

In the course of the test, the specimen bends due to the load applied by the loading ring, while the supporting ring restrains the sample movement. The stress within the sample can be estimated by the linear bending theory and the maximal stress is expected to be constant in the area inscribed by the loading ring as long as the deflection is smaller than half specimen thickness, a condition that was satisfied in the current work. The elastic modulus is calculated as designated in ASTM C1499-05 [141] based on the following equation:

$$E = \frac{3 \cdot \Delta F \cdot r_1^2 \cdot (1-\nu^2)}{2\pi \cdot \Delta s \cdot h^3} \cdot \left[\left(\frac{r_2}{r_1}\right)^2 - 1 - \ln\left(\frac{r_2}{r_1}\right) + \frac{1}{2}\left(\frac{1-\nu}{1+\nu}\right) \cdot \left(\frac{r_2^2 - r_1^2}{r_3^2}\right) \cdot \left(\frac{r_2}{r_1}\right)^2 \right] \tag{3.8}$$

where ΔF and Δs are the difference in force and displacement, respectively, derived from the linear part of the displacement curve, r_1, r_2 and r_3 are the radius of the loading ring, supporting

ring and sample, respectively, h is the specimen's thickness, and ν is the Poisson's ratio, here considered to be 0.232 for all compositions, the same value as reported for pure $SrTiO_3$ [97].

The maximum stress in the center area of the sample can be calculated by:

$$\sigma = \frac{3 \cdot F \cdot (1+\nu)}{2\pi \cdot h^2} \cdot \left[ln\left(\frac{r_2}{r_1}\right) + \left(\frac{1-\nu}{1+\nu}\right) \cdot \left(\frac{r_2^2 - r_1^2}{2 \cdot r_3^2}\right) \right] \tag{3.9}$$

where F is the applied force. Once brittle fracture occurs, the material's fracture stress is derived from the equation above considering the maximum load applied by the test machine caused the sample to fail.

The tests were performed at distinct loading rates for samples produced by tape casting, freeze-drying, and phase inversion tape casting as described previously. The number of samples, their dimensions, and test conditions are summarized at Table 3-5. The results were used as basis for a statistical analysis (Weibull distribution) according to ASTM C1239-07 [142] and Weibull modulus and characteristic strength were determined via linear regression of the results obtained by the test at 100 N/min load rate. Although the specimen number was smaller than the 30 suggested in the standard for a Weibull analysis, the analysis was carried out here to serve as a guide for materials' development. For other loading rates (subcritical crack growth analysis) specimen numbers very even smaller and hence only average fracture stresses were considered. For the linear regression analysis, natural logarithms of both sides of the equation 2.9 are taken as follows:

$$ln\left[ln\left(\frac{1}{1-P_f(V_0)}\right)\right] = m \cdot ln\,\sigma_f - m \cdot ln\,\sigma_0 \tag{3.10}$$

which corresponds to a linear function with the form $y = ax + b$. The values of the individual fracture stresses σ_f are then ranked in ascending order and related to specific probability P_i:

$$P_i = \frac{i}{(k+1)} \tag{3.11}$$

where i is the rank number and k is the number of tested specimens [143]. In addition, the subcritical crack growth sensitivity and the stress-time-probability diagrams were also assessed with the method described in Chapter 2 for dense tape cast STF-X specimens.

Table 3-5 - Summary of ring-on-ring samples.

Material	Manufacturing method	Porosity [%]	Dimension [mm²]	Load Rate [N/min]	Number of Samples
STF25	Tape casting	1.9	Ø14 × 0.7	1	6
				10	7
				100	13
				1000	8
	Tape casting	32.0	Ø15 × 1.0	100	12
	Freeze-drying	45	Ø21 × 1.5	100	11
	Phase inversion	28	Ø16 × 0.7	100	12
STF35	Tape casting	2.0	Ø15 × 0.8	1	6
				10	6
				100	14
				1000	6
STF50	Tape casting	5.5	Ø15 × 0.6	1	5
				10	5
				100	13
				1000	5

In order to investigate the subcritical crack growth effect at high temperature and/or a possible anelastic effects, 5 tape cast dense specimens of the composition STF25 were heated up to 900 °C and afterwards loaded at 1 N/min until fracture. The same procedure was repeated for another 5 specimens of the same batch, but with a loading rate of 100 N/min. In case of subcritical crack growth occurrence, the fracture stress should increase with increasing loading rate.

3.4.3 Uncertainty calculation of the subcritical crack growth exponent and the lifetime predictions

Estimation of the subcritical crack growth exponent and its uncertainty

It was demonstrated in section 2.3.4 that the fracture stress has a correlation to the stress rate in case of existence of a subcritical crack growth phenomenon, according to:

$$\log \sigma_f = \frac{1}{(n+1)} \log \dot{\sigma} + \log D \tag{3.12}$$

which has the linear form $y(x) = \alpha x + \beta$. If linear regression is performed for the logarithm of the fracture stress data as function of logarithm of the stress rate, the slope of the obtained curve is equal to $\alpha = 1/(n+1)$ and the intercept equal to $\beta = \log D$. For the linear fitting, York's method might also be applied to estimate the deviation of the slope and intercept, since it considers the standard deviation of the measurements. This method uses the experimental uncertainty as weight and approximates the best linear fitting with cubic equations, differently from the least-square linear regression, in which the fitting methods are done by square equations [143].

However, the slope deviation does not represent directly the uncertainty of n and, once York's method is based on numerical solutions, an equation for the direct uncertainty of n is not trivial. Thus, it is suggested here that the lowest n^- and highest n^+ value for the subcritical crack growth exponent (worst and best case) may be obtained from the slope deviation:

$$n^- = \frac{1}{\alpha - \delta\alpha} - 1 \tag{3.13}$$

$$n^+ = \frac{1}{\alpha + \delta\alpha} - 1 \tag{3.14}$$

where $\delta\alpha$ is the slope uncertainty obtained by York's method. It can be observed from equations (3.13) and (3.14) that the deviation of the subcritical crack growth exponent is asymmetric.

Uncertainty of lifetime predictions

The uncertainty of the lifetime predictions should include the error propagation of every equation used to derive the stress-time-probability diagram. Therefore, in order to derive the accuracy of the method, the 95% confidence interval in the Weibull distribution is transferred to stress-time-probability diagrams in the form of best and worst case scenarios. Here, a combination of best and worst properties derives an interval of probabilities, in which the real case will be included.

It can be assumed that the worst case scenario will be the one where the lowest bound of the characteristic strength has the lowest subcritical crack growth exponent, i.e. n^- obtained with equation (3.13). The same may be valid for the best case, where the upper bound of the characteristic strength has the highest subcritical crack growth exponent, in this case, n^+ estimated by equation (3.14). The derivation of the worst and best cases intervals follows the same procedure for the 95% confidence interval of the Weibull distribution, as explained in section 2.3.2. For this, it is also assumed that the Weibull modulus does not have a dependence on time.

3.4.1 Impulse excitation technique

The impulse excitation method is a non-destructive mechanical test that enables to derive the elastic and shear modulus, Poisson's ratio and damping coefficient. In addition, the procedure can be performed from room to high temperatures, rendering the test interesting to measure the elastic properties in a temperature range.

During the experiment, the samples are mechanically excited by a point strike and the resulting mechanical vibrations are recorded by a microphone. The recorded resonance frequencies can be used to calculate the elastic modulus according to ASTM E1876 [144], using the equations for disc-shaped specimens:

$$E_1 = \frac{12 \cdot \pi \cdot f_1^2 \cdot D^2 \cdot m \cdot (1 - \nu^2)}{{K_1}^2 \cdot h^3} \tag{3.15}$$

$$E_2 = \frac{12 \cdot \pi \cdot f_2^2 \cdot D^2 \cdot m \cdot (1 - \nu^2)}{{K_2}^2 \cdot h^3} \tag{3.16}$$

where f_1 and f_2 are the first and second resonant frequencies detected by the equipment according to the scheme displayed in Figure 3-7 respectively, D is the diameter, m is the mass and h is the sample thickness. K_1 and K_2 are the first and second geometric factors given by the cited standard. The value of the elastic modulus can then be calculated simply by the arithmetic average of E_1 and E_2:

$$E = \frac{E_1 + E_2}{2} \tag{3.17}$$

In this experiment, a disc shaped STF25 sample (Ø35 mm × 1 mm) obtained by tape casting was used. The test is performed automatically by the impulse excitation machine (GrindoSonic) starting at the room temperature and at every 10 K until 1000 °C, at the heating rate of 1 K/min. It is important to notice that the specimen's geometry changes during the measurement due to thermal expansion. The apparent geometry of the specimen as function of the temperature was calculated with respect to its thermal expansion coefficient, reported in the literature to be 11.9 × 10^{-6} K^{-1} in the range of 50 to 400 °C and 15.9 × 10^{-6} K^{-1} from 400 to 1000 °C [11], yields then a change in geometry of 1.3%, which appears to be negligible.

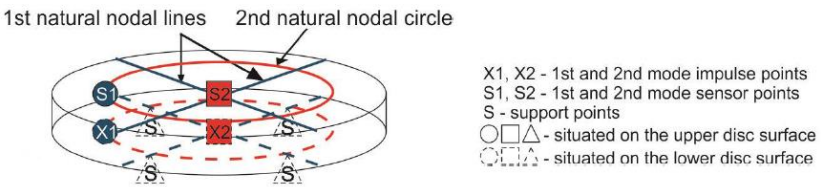

Figure 3-7 - Impulse and sensor position for disc-shaped specimens [134].

The impulse excitation technique can also be used to derive the coefficient of internal friction as a function of the temperature, which may be used to evaluate potential anelastic behaviour. The internal friction influences the damping of the elastic vibrations of a material excited by impulse. Consequently, the amplitude of the elastic vibrations A of a solid excited by impulse follows an exponential decay over a time t given by:

$$A = A_0 \exp(-\tau \cdot f_n \cdot t) \tag{3.18}$$

where A_0 is the natural frequency's initial amplitude of the excited solid, f_n is the resonant frequency, and τ is the damping ratio (damping coefficient). The exponential decay of the amplitudes is schematically illustrated in Figure 3-8. The coefficient of internal friction Q^{-1} is related to the damping ratio by $Q^{-1} = \tau/\pi$.

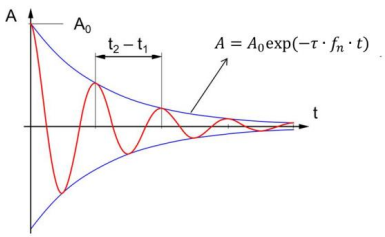

Figure 3-8 - Damped oscillations of an impulse-excited solid.

In order to obtain the internal friction Q^{-1} as a function of the temperature for STF25, a tape cast stripe with geometry 40 × 10 × 1 mm³ was tested into the same impulse excitation machine (GrindoSonic) starting at the room temperature and at every 10 K until 900°C. The amplitude of the frequencies generated by each impulse measurement was recorded for 0.5 s, from which the exponential decay can be extracted. In this case, for more precise measurements, the damping curve recorded by the equipment is fitted by an exponential decay function of the type:

$$y = a \exp\left(-\frac{x}{b}\right) \tag{3.19}$$

where $a = A_0$, $b = 1/(\tau \cdot f_n)$, and x is the time variable t. The fitting was realized via the data analysis software OriginPro 2015®, where the parameter b was obtained.

3.4.2 Compressive tests

Compressive or crushing tests are commonly used to assess compressive strength and elastic modulus of materials and frequently also used to characterize the stress-strain behavior of membrane materials [145, 146]. Within this work, the test was used to derive the anisotropy of the mechanical properties of the freeze dried specimens. In the test, the sample is uniaxially loaded in an electromechanical machine (INSTRON 1362) and the displacement during the test is measured with three ceramic extension rods located 120° to each other and positioned outside the specimen, which are connected to a linear variable differential transformer (Solartron Metrology). The test setup is displayed in Figure 3-9. The stress σ is calculated via:

$$\sigma = \frac{P}{A} \tag{3.20}$$

where P is the applied load and A is the specimen's cross-sectional area. Similarly, the strain ε can be calculated using:

$$\varepsilon = \frac{\Delta L}{L_0} \tag{3.21}$$

where ΔL is the measured displacement and L_0 is the initial height. The apparent elastic properties are obtained from the slope of unloading-curves in a non-destructive compressive test. For this study, 4 samples were loaded and un-loaded until 30 MPa in two different directions: parallel (out-of-plane direction or plane xy in Figure 3-2) and perpendicular (in-plane direction or planes xz and yz in Figure 3-2) to the freeze direction.

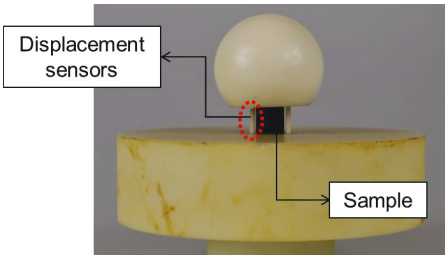

Figure 3-9 - Compressive test setup.

The apparent elastic moduli were obtained for the respective loading plane based on the relationship:

$$E_{app} = \frac{d\sigma}{d\varepsilon} \tag{3.22}$$

With the purpose to determine the average fracture stress, specimens were loaded until fracture in the in-plane (10 specimens) and out-of-plane (9 specimens) directions. The samples' displacement was also measured during the test in order to obtain the fracture strain. The tested specimens' dimensions are 6 × 6 × 4 mm³. It is expected that the apparent elastic modulus and average fracture stress in these two tested directions differ from each other since the microstructure is anisotropic.

3.4.3 Acoustic emission and optic observation of fracture

If a material is deformed under stress, acoustic signals might be emitted, indicating that some acoustic energy emitting event is happening in the structure. These sounds could be related to crack growth, friction, yielding, phase transition, corrosion, etc. Therefore acoustic emission observation can be an important method in terms of the investigation of a material's fracture mechanism. The currently used set-up includes a detection instrument (AMSY-5, Vallen Systeme), a preamplifier (AEP3/4, Vallen Systeme) and two acoustic sensors (25-80 kHz VS30-V, Vallen Systeme). The system permits to monitor the acoustic emission during the compressive test and to display it as hits / counts (beginning of an event) per unit of time. Furthermore, the amplitude and energy count of each hit is also measured and the data is processed on acoustic emission suite software (Valley Acoustic Emission Suite®).

With respect to this part of the investigation, two specimens were tested, each one in a distinct direction (in- and out-of-plane). Before the compressive test, the sensors were connected to platinum wires, which were physically attached to the specimens by a steel spring. Afterwards, the specimen was loaded via a compressive stress in the same electromechanical machine as described in section 2.2 until fracture and the acoustic emission was recorded meanwhile.

The observation of fracture was in addition conducted under a scanning electron microscope (ZEISS Supra 50 VP), where the specimens were tested via uniaxial compressive loading by an electromechanical component (Kammrath & Weiss). For this investigation, the surface of interest of each sample was prepared by ceramography, as described in section 3.3.7 to observe the pore structure and changes induced by loading. The crushing test was carried out at constant deformation rate (3 µm/s) for the two specimens, one loaded in the in-plane and the other in the out-of-plane direction. Images of the surface were recorded after fracture initiation, which required, for this purpose, the interruption of the loading. Further deformation was applied to the sample afterwards till failure.

3.4.4 Compressive creep

Steady-state creep behaviour was investigated on the basis of compressive tests with respect to the effect of the manufacturing technique (porosity and pore structure). The microstructures of interest are the ones obtained by tape casting and freeze-drying, this last one also concerning the influence of loading direction on the creep behaviour. In addition, a dense STF25 sample obtained by uniaxial pressing was used as reference for the creep parameters. This specimen was beforehand sintered at 1300 °C for 5 hours and the remnant porosity calculated by image analysis method (as described in Chapter 3) is 1.1 ± 0.1%. Furthermore, previous the creep tests, the flat surfaces of each specimen were polished in order to reduce roughness and obtain parallel contact surfaces.

Steady-state creep rates were obtained experimentally in compression at different temperatures and applied stresses. During the test, the specimens were heated up at a rate of 5 K/min to the testing temperature. Later, the stress was applied by an electromechanical machine (INSTRON 1362), meanwhile the deformation was monitored over time with a linear variable differential transformer (Solartron Metrology). The subsequent increment on the strain ε was calculated using:

$$\varepsilon = \ln\left(\frac{L}{L_0}\right) \tag{3.23}$$

where L and L_0 are the specimen's instantaneous and initial heights, respectively. The duration of the creep test should be long enough to reach constant deformation rate stage, i.e. steady-state creep. The creep rate is obtained by linear fitting of the strain in function of time after primary creep:

$$\varepsilon = \alpha + \dot{\varepsilon} \cdot t \tag{3.24}$$

where α is the intersection with the y-axis, $\dot{\varepsilon}$ is the creep rate (the slope of the linear fitting), and t is the time. The creep test conditions are summarized in Table 3-6.

Table 3-6 - Compressive creep test conditions

Manufacturing	Porosity [%]	Geometry	Temperatures [°C]	Stresses [MPa]
Pressing	1.1	Ø6 × 5 mm²	900, 950, 1000	15, 30
Tape casting	32	Ø4.8 × 2 mm²	850, 900, 950, 1000	15, 30, 45
Freeze drying (in-plane)	45	6 × 6 × 4 mm³	800	15
			900, 950, 1000	15, 30
Freeze drying (out-of-plane)	45	6 × 6 × 4 mm³	900, 950, 1000	15, 30

The complex test matrix along with the rather time consuming testing of each specimen limited the experimental creep data, hence, the activation energy and the stress exponent were derived from the experimental data via fitting with a global best equation that describes the behaviour of all STF25 materials (see also [147]). Consequently, the global fitting represents simultaneous curve fitting operations performed on multiple datasets. In other words, these operations return one value for activation energy and one for stress exponent by the fitting of all creep data, independent of the specimen, however, with associated, representative uncertainty (standard deviation), hence permitting an assessment of accuracy of procedure and data description. Therefore, in this case, it is assumed that the activation energy and the stress exponent are properties of the material and the porosity is considered to have a minor influence

on them. The global fitting is done in the data analysis software OriginPro® 2015 as described in [147] and in [148].

CHAPTER 4 Results and discussion

4.1 Powder and specimens characterization

This section concentrates on the characterization of the obtained powder properties and also the evaluation of the microstructure of the processed STF-X membrane and substrate materials. Emphasis is given to the characteristics that might influence the mechanical properties of the obtained specimens.

4.1.1 Powder properties

X-ray diffraction was used to characterize the phases that exist after calcination of the oxides. The results presented in Figure 4-1 reveal that the final materials contain the desired cubic perovskite phase. With exception of STF-25, the other compositions corresponded to a single phase, verifying that the solid state reaction is a successful procedure to fabricate the powders. A small count of an hexagon iron and strontium rich phase was indentified for STF-25. However, the phase may not have undisered effects on the functional and mechanical properties of the material, since its concentration might be rather low as indicated by the low intensity of the XRD peaks.

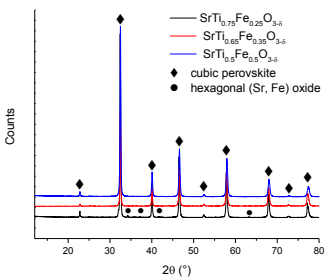

Figure 4-1 - XRD analysis for STF-X compositions after calcination.

Samples extracted from the slurries at different times during the milling process were used to determine particle size distribution and average particle size as a function of milling time. In Figure 4-2 STF-25 particle size distributions in percentage, here defined as *q*, are presented, as well as their cumulative sum, *Q(r)*. As can be seen, initially the powder can be represented by a bimodal dispersion with grains larger than 3 µm. As the milling progresses, the distribution approaches a normal distribution for all STF-X powder batches. The particle size distribution as a function of time for STF35 and STF50 can be found in the Appendix B.

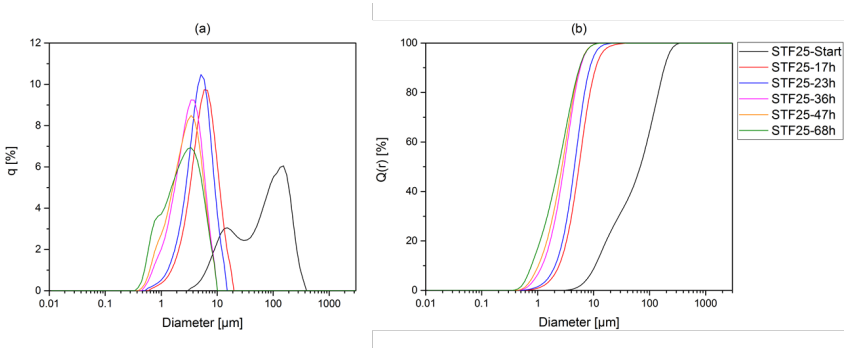

Figure 4-2 – (a) Particle size distribution and (b) its cumulative sum, STF-25 powder.

The results of the particle size analysis after the 72h milling time are summarized in Table 4-1. The values of D_{10} and D_{90} represent the particle size at which 10 and 90 percent, respectively, of the population are below. The average particle size lies within the range of 1 to 2.4 µm and the specific surface area between 1 – 5 m²/g.

Table 4-1 - Properties of the powders after 72h milling time.

	D_{10} [µm]	D_{50} [µm]	D_{90} [µm]	Specific Area [m²/g]
STF25	0.771	2.35	5.58	1.385
STF35	0.579	1.13	2.38	4.654
STF50	0.472	1.06	2.20	4.436

The dilatometry results of pressed STF-X samples are presented in Figure 4-3. Accordingly, the samples begin to shrink at temperatures above 800 °C, indicating that the sintering process begins at this point. Furthermore, the maximum densification for STF25 is

reached once the temperature exceeds 1350 °C. On the other hand, STF35 consolidates already above 1250 °C. At 1350 °C an abnormal behavior is observed, i.e. the sample starts to swell. The cause of the material's swelling might be attributed to oxygen release due to iron reduction at higher temperatures [36]. Since the microstructure is dense, the gas cannot escape, contributing to the coalescence and growth of pores.

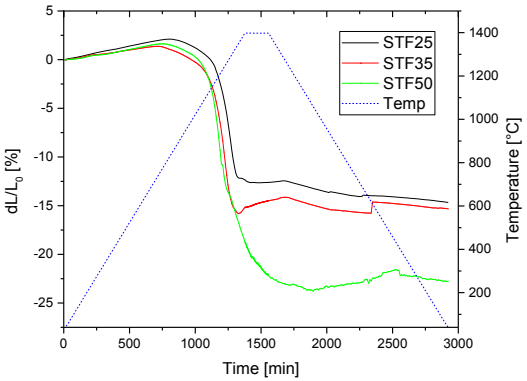

Figure 4-3 - Dilatometry analysis of pressed STF-X samples.

With respect to STF50, a less effective sintering was observed, since the specimen did not reach a full densification plateau as for the other two compositions. This effect might be associated to a lower green density of the pressed sample compared to the others, which was not determined prior to the test. Also, after the dilatometry test, the STF50 specimen developed a molten phase, which might indicate that temperatures in the range of 1400 °C are too high for the sintering process.

4.1.2 Microstructure of tape cast specimens

Polished and chemically etched cross-sections of sintered samples were analysed using scanning electron microscopy and the corresponding porosity was estimated using the image analysis software AnalySIS Pro®. Porosities for STF25, STF35, and STF50 are 1.9 ± 0.3 %, 2.0 ± 0.7 %, and 5.5 ± 0.5 %, respectively, which corresponds to densities of 5.08 ± 0.02 g/cm³, 5.11 ± 0.04 g/cm³, and 4.98 ± 0.03 g/cm³ respectively. The pores appear to be randomly distributed

within the samples' volume as seen in Figure 4-4, which displays the chemically etched, polished surfaces of STF-X samples analysed via scanning electron microscopy, visualizing grain boundaries. The average grain size estimated from image analysis are 1.2 µm, 0.6 µm, and 1.4 µm for STF25, STF35 and STF50, respectively. Among all samples, STF35 possessed the finest microstructure, followed by STF25 and STF50, which have similar average grain sizes. In addition, XRD investigations on sintered STF25 specimens revealed that the above mentioned hexagonal iron rich phase, present in the calcined powder, disappeared after sintering. A XRD diagram comparing the as-received powder with a sintered specimen is displayed in Appendix C.

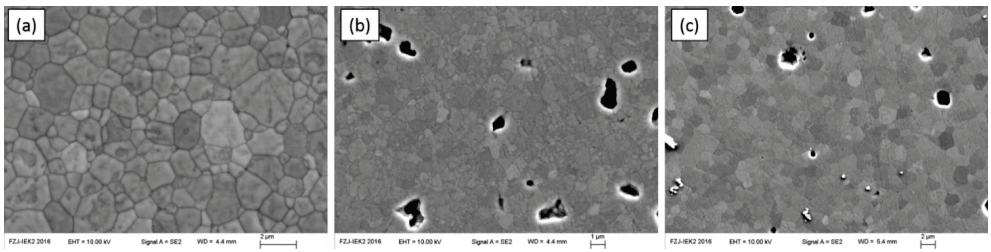

Figure 4-4 - SEM images of chemically etched STF-X samples; (a) STF25, (b) STF35, and (c) STF50.

With respect to the STF25 tape cast specimens produced with pore formers, their porosities were evaluated by a water immersion Archimedes' method, which derived an open porosity estimate of 32 ± 1%. Hence, the obtained open porosity is satisfactory for application as membrane supports. Furthermore, representative for all compositions, the polished cross-section of one tape cast STF25 porous sample was analyzed via scanning electronic microscopy, see Figure 4-5. The microstructure consists of randomly distributed pores and the derived average pore size estimated with the image analysis software AnaliSYS® is 7 ± 3 µm.

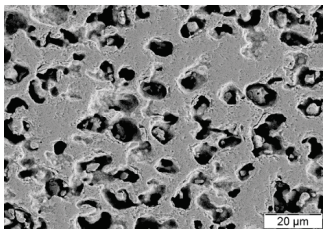

Figure 4-5 – SEM image of polished cross-section of a tape cast STF25 porous sample.

4.1.3 Microstructure of freeze dried STF25 specimens

Only one composition was selected for the freeze drying process. Figure 4-6 presents scanning microscopy images of the cross-sectional fracture surface of a freeze dried STF25 specimen in as-sintered state. As can be seen, the pore structure consists of elongated channels that mimic the ice crystals structure obtained during the freezing process. The apparent porosity estimated with the aid of the Archimedes' method is 31.8 ± 0.5% for a whole sample. The so-called "nucleation region" [149] appears to be rather dense after sintering, as can be seen in Figure 4-6 (c) and (d). The reason for the dense structure can be associated with the high surface area, caused by the fine porosity and sintering activity of STF-X materials, which led to a dense layer with closed porosity. Therefore, the method might be used directly to obtain asymmetric membrane structures.

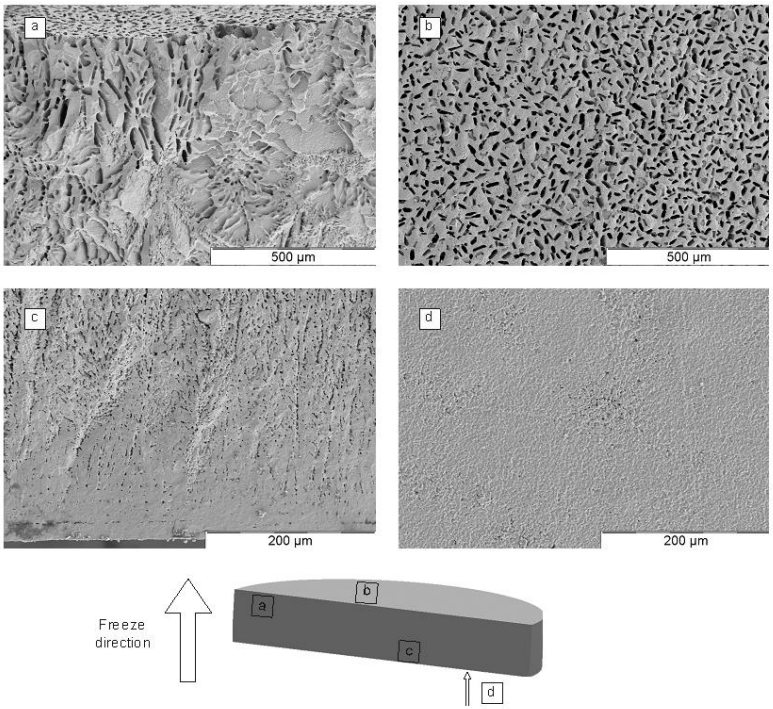

Figure 4-6 - SEM images of a fractured freeze dried STF25 sample, schematic image shows the positions where specimens were extracted and respective images were obtained, a) fracture surface cross-section, b) as-cast surface, c) fracture surface cross-section lower side and d) as-cast surface lower side.

Mercury intrusion porosimetry was also conducted for a machined specimen in order to characterize the pore structure regarding pore equivalent radius and distribution. Due to the nature of the technique, the results for pore aspect ratio are given in terms of an equivalent radius, as the pores were cylindrical. The cumulative porosity as function of equivalent pore radius is presented in Figure 4-7. Similarly, the distribution of the pore size according to the relative porosity volume is also included in Figure 4-7. Machined samples, which were cut from the interior of the whole freeze-dried bulk (see section 3.2.2), resulted in a porosity of 47% by mercury porosimetry and 45 ± 3 % by Archimedes' method. The diagrams presented below revealed that the majority (more than 85%) of the pores have an equivalent radius between 1 and 10 µm, and 12 % are in the region of 10 to 100 µm. It is noteworthy here to highlight that there is a small percentage of pores with an equivalent radius larger than 100 µm. Although the relative total volume of these pores is small in comparison to the majority, these might be crucial to the fracture stress, since they could be fracture origins.

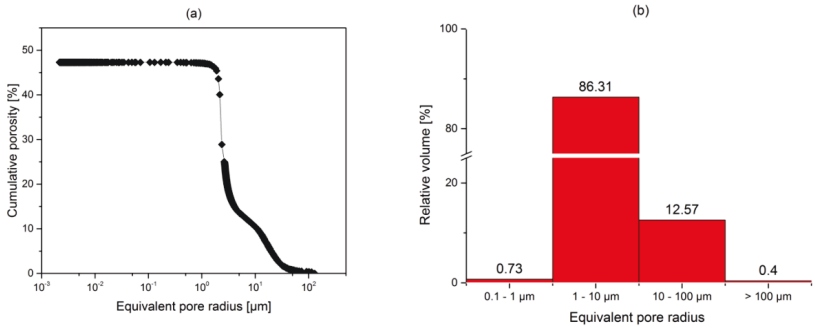

Figure 4-7 - Mercury intrusion porosimetry results: cumulative porosity as function of the equivalent pore radius (a) and relative volume as a function of equivalent pore size (b) of a machined freeze-dried specimen.

Figure 4-8 illustrates polished sections of the directions out-of-plane (parallel to the ice crystal growth) and in-plane (perpendicular to the ice crystal growth) planes of machined freeze-dried specimens. An image analysis software (AnlySIS pro ®) was used to determine the pore's length a, width b, aspect ratio χ_p, height L, and wall thickness t. The image analysis was conducted on 15 distinct SEM pictures, similar to Figure 4-8, captured in different positions of the polished surfaces, in total based on the identification and classification of 4830 pores. The

average outcome for the measured pore dimensions is summarized in Table 4-2 and the size distributions are portrayed in Figure 4-9. It is noteworthy to mention that the images presented in Figure 4-8 represent only the two-dimensional pore structure. Therefore, the image analysis in Table 4-2 does not cover entirely the 3D pore morphology of a real specimen volume and the experimental deviations with respect to pore dimensions might be larger than what has been determined.

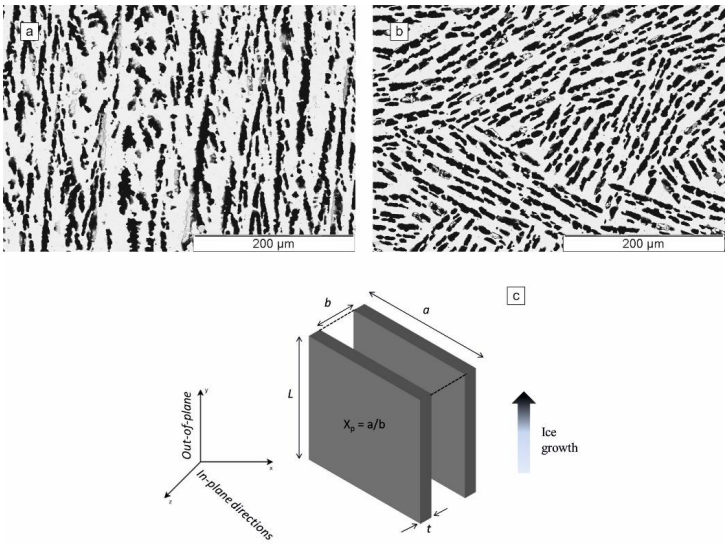

Figure 4-8 - Polished sections of a freeze dried specimen showing the (a) out-of-plane and (b) in-plane planes; (c) shows a schematic representation of the pore wall lamellas.

Table 4-2 - Results of the image analysis for the pore dimensions of the structures displayed on Figure 3.

	Symbol	Outcome of the image analysis
Pore height	L	18 ± 9 µm
Pore wall cross-sectional area	A_s	80 ± 47 µm²
Pore aspect ratio	χ_p	2 ± 0.6
Pore wall length	a	10 ± 3 µm
Pore width	b	4 ± 1µm
Wall thickness	t	8 ± 4 µm

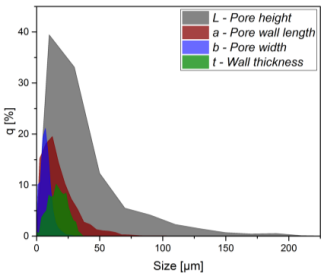

Figure 4-9 – Pore size distribution.

4.1.4 Phase Inversion

The phase inversion method was adapted in this work for the processing of STF25 asymmetric membranes with hierarchical porosity. A SEM image of a polished cross-section of such specimen is portrayed in Figure 4-10, where large finger-like pores across the thickness can be observed. The structure can be divided basically into two parts: a porous substrate and a rather dense membrane layer. The top part of the porous support, characterized by a fine porosity, corresponds to the side of the tape that was in constant contact with the water bath during the process. At this part, the solvent exchange took place creating small openings for the water penetration. Along the thickness, the pores grow in diameter towards the membrane layer as a result of the further solvent exchange. Also, remaining porosity is observed in the edges of the large pores and it is probably related to poor packing of the ceramic particles when the solvent was removed in the water bath. These details can be observed with better resolution in the panorama reconstructed with images along the cross-section with larger scale, which is found in the Appendix C.

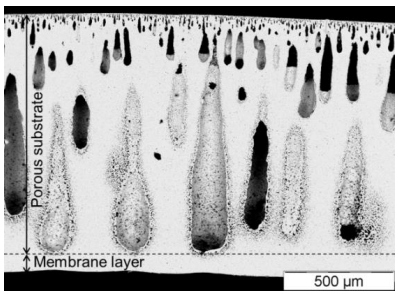

Figure 4-10 - SEM image of a polished cross-section of a phase inversion STF25 specimen.

The density of the specimens according to Archimedes' method is 4.04 ± 0.8 g/cm³, which represents a total porosity of 22 ± 1 %. Nevertheless, the same method yielded an apparent open porosity of 5 ± 1%. The rather low apparent open porosity compared to the total may be attributed to the fine porous layer formed on the top of the sample. This zone may have densified during sintering closing the path to the large pores. Also, due to the two-dimensional characterization of the microscopy imaging, it is not possible to confirm whether the pores are connected via a three-dimensional structure.

The pore structure analysis was conducted using the image analysis software AnalySIS® in order to obtain the pore dimensions and the results are summarized in Table 4-3. As it can be observed, the image analysis derived a rather low average pore equivalent diameter and pore length with a large standard deviation. In this case, the large amount of pores with sizes in the range of 1 to 2 µm in the upper part of the analyzed specimens, as well as the enclosed porosity around the finger-like pores, drags the average to a smaller pore size. However, large pore lengths were also identified and they correspond to sizes greater than 800 µm. Such large pores may have strong influence on the mechanical stability once they are potential spots for fracture initiation. Thus, in order to average the pore diameter weighting the pores with greater size, it is necessary to use another method where the pores with larger size have more weight in the average. In this case, the Sauter pore mean diameter offers a more effective pore size. The Sauter mean diameter converts the area of all pores as if they were a single sphere, and the diameter of this sphere would have the Sauter mean diameter [150]. This can be calculated by the following equation.

$$d_s = \frac{\sum_{i=0}^{N} n_i \cdot d_i^3}{\sum_{i=0}^{N} n_i \cdot d_i^2} \tag{4.1}$$

where N is the number of pores and d_i is the pore diameter at the position n_i, when the pore diameters are arranged in a crescent order. Consequently, the Sauter mean diameter is larger than the normal averaged equivalent circular diameter, since the large pores are weighted with a higher factor. Additionally, considering the large gradient of porosity, it is possible that the material's properties are a function of the relative position along the thickness. This, however, was not investigated in the scope of the present work.

Table 4-3 - Image analysis outcome of the pore dimensions of a phase inversion tape cast specimen.

	Average	Max	Min
Equivalent circular diameter [μm]	3 ± 2	332	0.8
Pore length [μm]	6 ± 4	862	1
Pore width [μm]	3 ± 2	249	0.7
Aspect ratio	1.6 ± 0.4	15	1
Sauter mean diameter [μm]	293	-	-

4.1.5 Summary

This section concentrates in the processing of STF-X powders and ceramics with distinct microstructures. The summary of the final remarks is presented below:

- The STF-X powders were produced via solid state reaction and it was verified that the chosen method was efficient, though simple, to obtain a single phase material with the desired cubic perovskite structure.
- Regarding STF25, though a small amount of an iron and strontium rich hexagonal phase appeared to be present in the powder, the sintering behavior of tape cast samples wasn't affected. The dilatometry analysis helped to understand the sintering behavior of the studied compositions and aided the further samples processing.
- The tape casting method was developed for the studied STF-X compositions and rather dense and porous specimens were successfully obtained. The microstructure analysis for the dense samples revealed rest porosity in the range of 1 to 5%, while the porous specimens had an apparent porosity of 32%.
- Porous supports for asymmetric membrane application were successfully developed for STF25 ceramics through the freeze-drying method. Scanning electron microscopy images verified channel like pores that spread through almost the whole specimen.
- The phase inversion tape casting method was adapted to produce porous STF25 asymmetric membranes. Although successful in order to obtain large finger-like pores and an apparent dense membrane layer, the apparent open porosity is rather low for application as oxygen transport membrane. This might be attributed to a fine porous zone at the top of the specimens, which should be removed to increase the open porosity. The

finger-like pores have maximum size in the range of 800 μm, which are relevant for the mechanical stability of such specimens.

4.2 Mechanical properties of $SrTi_{1-x}Fe_xO_{3-\delta}$ membranes: a room temperature study

This section summarizes mechanical characterization results of STF-X, with X = 25, 35, and 50% mol Fe, based on distinct standardized methods (depth-sensitive micro-indentation and ring-on-ring bending tests). The data assessed thereby also aid the prediction of reliability, subcritical crack growth and lifetime of the studied materials.

4.2.1 Indentation elastic modulus, hardness, and fracture toughness

In order to determine the effect of iron doping on STF-X materials in the densest state it is necessary to mitigate the microstructural effects that may influence the mechanical properties, such as porosity, grain boundaries, inclusions, etc. This can be done by the use of nano-indentation, since in this method very low loads can be applied.

Table 4-4 summarizes the results for a continuous multicycle nano-indentation testing on the same STF-X specimens used for micro-indentation. The nano-indentation elastic modulus E_{NIT} and hardness H_{NIT} corresponds to the average of all 20 measured points while E_{max} is the highest measured elastic modulus for each material. It is assumed here that E_{max} approaches the properties of the single crystal, once the penetration depth may be up to one order of magnitude lower than the average grain size. Therefore, the properties measured may correspond to the pure material, whereas the average value in a multicycle is still affected by materials flaws. The obtained values for E_{NIT} as a function of penetration depth for the STF25, STF35, and STF50 specimens are displayed in Figure 4-11. With increasing load, i.e. for higher penetration depths, the elastic properties tend to remain constant in the testing load range for all investigated specimens.

Table 4-4 - Continuous multicycle nanoindentation results for 10 cycles and loads increasing linearly from 5 to 50 mN.

	E_{NIT} [GPa]	E_{max} [GPa]	H_{NIT} [GPa]
STF25	230 ± 16	282	13 ± 1
STF35	223 ± 24	281	13 ± 1
STF50	216 ± 18	247	12 ± 2

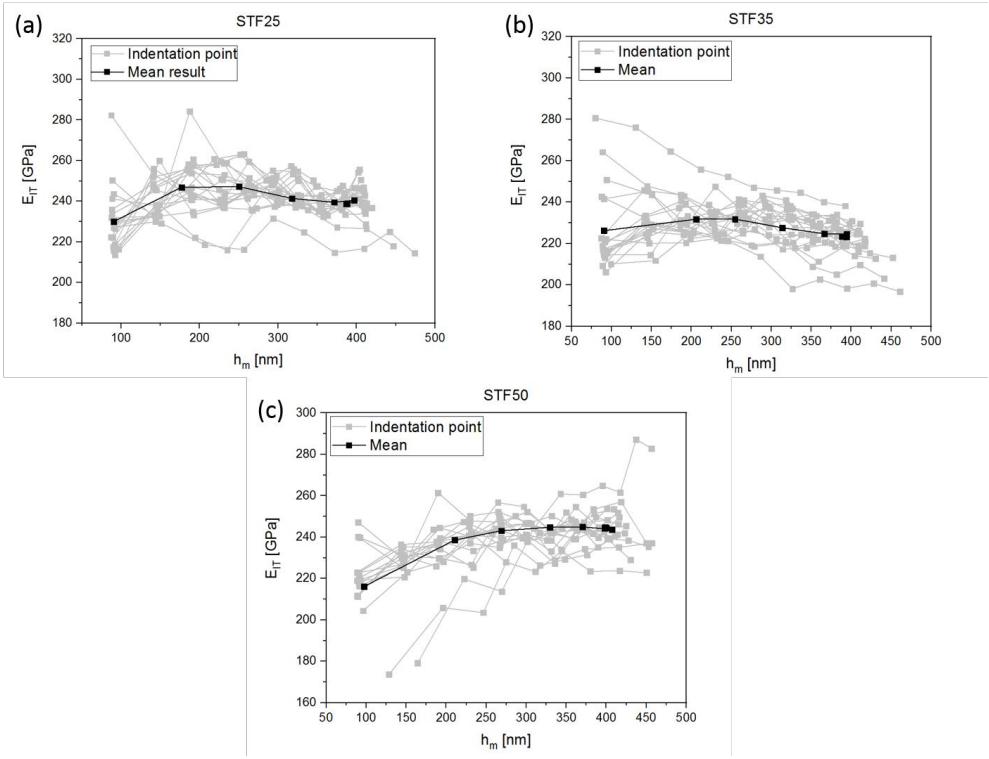

Figure 4-11 - Nano-indentation elastic modulus as a function of the penetration depth for a (a) STF25, (b) STF35, and (c) STF50 tape cast specimens (continuous multicycle load increasing from 5 to 50 mN).

It was expected that, with increasing iron content, the number of structural defects (oxygen vacancies) increases due to the partial substitution of Ti^{4+} by $Fe^{3+/4+}$, which may lead to less stability and, hence, to lower elastic properties. However, the estimated elastic moduli and hardness of all compositions showed no clear trend in relation to the Fe-content, while all average values agree within the range of uncertainty of the mentioned method. Yet, overall all parameters have a tendency to decrease slightly with the increasing iron content, which might indicate that the apparent elastic modulus and hardness of the considered STF-X materials is decreased slightly by the iron content. This might be confirmed by ab initio DFT calculations, which are, however, not within the scope of the current work.

Micro-indentation tests were carried out with a load of 1 N for the same STF-X dense tape cast samples addressing now the elastic modulus and hardness of the specimen (bulk), including

effects of remnant porosity and flaws. Additional tests with a load of 3 N were conducted to create cracks in all samples and hence to calculate the fracture toughness using the respective relationships presented in the experimental section for the median crack systems [151], which appeared to be appropriate since the ratio of crack length to indentation size was larger than 2. An indentation mark along with typical cracks obtained after the experiments is shown in Figure 4-12. The results of the indentation tests are presented in Table 4-5.

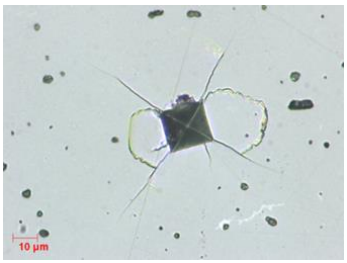

Figure 4-12 - Indentation on a dense STF25 tape casted sample, image after loading with 3 N.

Table 4-5 – Average indentation results and standard deviation for different samples; Young's modulus and hardness were estimated at 1 N load, while fracture toughness at 3 N.

	E_{IT} [GPa]	H_{IT} [GPa]	K_{IC} [MPa√m]
STF25	147 ± 10	9.8 ± 0.3	0.86 ± 0.09
STF35	123 ± 6	9.0 ± 1.0	0.80 ± 0.10
STF50	158 ± 10	9.3 ± 0.6	0.84 ± 0.06

Overall, the elastic modulus E_{IT} obtained for all STF-X specimens are smaller than the nano-indentation elastic modulus E_{NIT}. This result is expected, since the influence of the material's flaws on the mechanical properties is also accounted due to the larger size of the indenter, the higher loads and consequently, the larger tested volume. The micro-indentation elastic moduli obtained for STF25 and STF50 samples are in agreement with the values given in the work of Stournari [98], who quotes 165 ± 5 GPa and 157 ± 4 GPa for the compositions $SrTi_{0.70}Fe_{0.30}O_3$ and $SrTi_{0.5}Fe_{0.5}O_3$, respectively. Furthermore, the fracture toughness K_{IC} values are similar for all compositions and are within the limits of experimental uncertainty in agreement with the 0.93 ± 0.04 MPa√m reported for $SrTi_{0.70}Fe_{0.30}O_3$ [98] and 0.89 MPa√m [97, 113] reported for the end composition $SrTiO_3$.

STF35, however, shows a rather smaller micro-indentation elastic modulus when compared to the other two compositions. This might relate to the same microstructural effects that are acting reducing the elastic properties when the loads increase from the range of 50 mN (nano-indentation) to 1 N (current case). As mentioned in section 4.1.2, STF35 specimens have the smallest grain size, which are also smaller than the 1 N imprint size (in the range of 20 μm). Considering these circumstances, if the grain boundaries have a smaller elastic modulus than the grains itself, it is possible that the elastic properties of STF35 specimens are than influenced directly by the grain boundaries, deriving an even smaller elastic modulus. Still, it was not possible to obtain the elastic modulus of grain boundaries with the current applied methods.

4.2.2 Fracture strength and reliability of dense tape cast STF-X specimens

Fracture stress and materials' reliability were evaluated by ring-on-ring flexural tests at a rather high loading rate of 100 N/min to avoid possible subcritical crack growth influence onto the results. Being aware of the limits with respect to necessary specimen numbers of 30 suggested by industrial testing standards [142], the data (number of tests 11 to 14) were nevertheless analysed based on a Weibull statistics, where especially the Weibull modulus should therefore only be considered as an indication of the materials behaviour. The elastic modulus E_{RoR} and fracture strength σ_f, the characteristic strength σ_0, as well its lower and upper confidence bounds, and Weibull's modulus m of STF-X materials are summarized in Table 4-6. Furthermore, Figure 4-13 depicts the Weibull distribution for tape cast STF25, STF35, and STF50.

Table 4-6 - Ring-on-ring test results for STF-X materials.

	E_{RoR} [GPa]	σ_f [MPa]	σ_0 [MPa]	*Lower (95%)/upper (5%) confidence bounds for σ_0 [MPa]*	*m*	*Lower (95%)/upper (5%) confidence bounds for m*
STF25	108 ± 16	92 ± 9	98	88/109	7	4/10
STF35	98 ± 10	117 ± 15	125	112/140	6	4/9
STF50	122 ± 27	100 ± 15	99	85/114	4	2/6

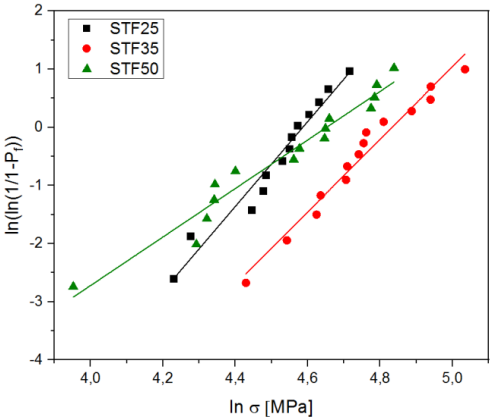

Figure 4-13 – Weibull distribution for the STF-X obtained using a loading rate of 100 N/min.

The elastic moduli obtained by ring-on-ring tests are smaller than those derived by depth-sensitive indentation (reduced to circa 75% of micro-indentation and 50% of nano-indentation results). This is expected since the indentation testing measures the properties of very small regions and may exclude the effect of porosity, which varied from 2 to 5% in the analysed samples, and other flaws, whereas the ring-on-ring test data reflect the effect of all flaws in the specimen and hence are typically lower and might on the other side be affected by frictional effects or unevenness [152]. These may increase the measurement uncertainties and raise the scatter of the measured strength up to 10% [152]. Hence, considering these boundary conditions, the difference between the results might be considered to be in an expected range. Similar observations were reported for low load indentation elastic modulus when compared to other techniques, as bending tests and impulse excitation [153, 154], where these differences can reach up to one order of magnitude. In addition, the same tendency observed in the micro-indentation tests is also reflected in the ring-on-ring results: the elastic modulus shows no clear trend with the composition for STF-X materials.

A comparison of the fracture strengths of the different materials requires a consideration of the microstructural boundary conditions, such as grain size, pore's size and distribution. Overall the fracture strength of the studied compositions appears to be similar within the limits of experimental uncertainty, both for average as well as characteristic value, also a similar behaviour can be observed for the rather comparable Weibull's moduli. Since the theoretical

strength should be proportional to the elastic modulus in a single crystal [83], it might have been expected that STF25 would have the highest fracture strength followed by STF35 and STF50. However, this was not observed for the tested specimens. Indeed, due to the larger tested volumes (tending towards the membrane components), flaws play a key role on the mechanical stability and, therefore, the effect of composition is mitigated.

Besides, as mentioned, the Weibull moduli are analogous for all materials within the limits of experimental uncertainty, indicating similar distribution of flaws that cause fracture, although larger specimen numbers would be required to confirm conclusions in this case. However, even though the distribution appears to be similar, STF35 specimens appear to have flaws of lower size compared to the other compositions, reflected in a slightly enhanced mechanical strength. Furthermore, it is noteworthy to mention that the characteristic strength of the studied materials in this work is larger than the values reported for other OTM materials. For instance, the characteristic strengths of $Ba_{0.5}Sr_{0.5}Co_{0.8}Fe_{0.2}O_{3-\delta}$ and $La_{0.6}Sr_{0.4}Co_{0.2}Fe_{0.8}O_{3-\delta}$ were reported in the literature as 86 ± 4 MPa and 73 ± 2 MPa, respectively [45].

Fractographic analysis of the samples was conducted using a confocal laser microscope, see Figure 4-14. The three-dimensional images reconstructed from the laser scanning microscopy enables the identification the flaws that might have initiated the fracture in the ring-on-ring tests. Therefore, the samples with the lowest fracture stresses from each composition (also regarding the tests under distinct loading rates) were selected for this investigation, since the largest defects can be expected for these specimens. In agreement with the highest stress during the bending tests existing at the surface, the main cause of fracture appeared to be pores localized at the sample's surface. Although just one half of the fracture surface is displayed in Figure 4-14, flaws of same size were observed in both fracture surfaces.

Furthermore, for a comparison, the size of the flaws can be estimated from the fracture toughness and individual fracture stress of the fractographically analysed sample using the following relationship [111] for the flaws displayed in Figure 4-14:

$$\sqrt{c} = \frac{K_{IC}}{Y\sigma_f} \tag{4.2}$$

where K_{IC} is the fracture toughness estimated by micro-indentation tests (see Table 4-5), σ_f the fracture stress of the displayed samples, c is the flaw size (here, the pore radius), and Y is a dimensionless factor, which depends on the crack and loading geometries and, for the current case, is approximately $1.12\sqrt{\pi}$ [111]. The derived results are compared to the fractographic results in Table 4-7 and it appears that the measured flaw size for STF25 and STF50 samples agrees with the result estimated using equation (4.2). The deviation between the measured and estimated flaw size for STF35 samples might rely on the difficulty to measure the defect size as well as its deviation from a half circular flaw, which is required for the application of equation (4.2) in this case.

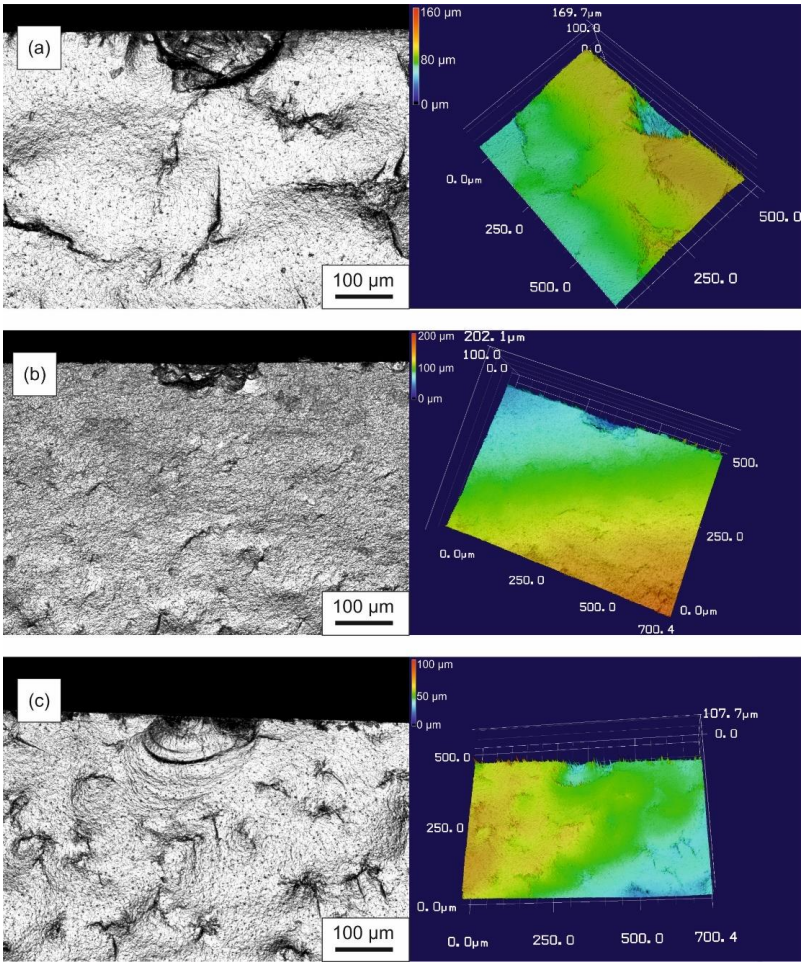

Figure 4-14 - Laser microscopy images of the flaws that may have originated the fracture in selected (a) STF25 (fracture stress 37 MPa), (b) STF35 (83 MPa), and (c) STF50 (44 MPa) samples.

Table 4-7 - Measured and estimated flaw sizes of samples with the lowest fracture strength for each composition.

Sample	σ_f [MPa]	Loading rate [N/min]	c [µm] – measured (Figure 4-14)	c [µm] – estimated (equation (4.2))
STF25	37	10	112	117 ± 7
STF35	83	100	88	23 ± 3
STF50	44	1	87	83 ± 4

4.2.3 Subcritical crack growth

Subcritical crack growth for STF-X materials was derived from ring-on-ring tests with different loading rates. Figure 4-15 shows the average fracture stresses as a function of the loading rate (number of specimens was too low for a Weibull analysis). The SCG parameter was calculated based on linear regression of the log-log data. The SCG parameters and their respective uncertainties are summarized in Table 4-8.

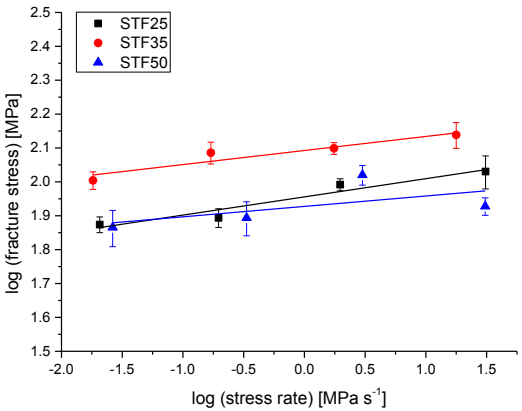

Figure 4-15 – Average fracture stresses of STF-X materials as a function of the loading rate.

Table 4-8 - SCG parameters for STF-X materials.

Material	*n* parameter	*D* parameter
STF25	18^{+5}_{-4}	90^{+4}_{-2}
STF35	23^{+7}_{-4}	124^{+3}_{-3}
STF50	32^{+569}_{-16}	85^{+7}_{-6}

Based on the tendency depicted in Table 4-8 and despite the high limit of uncertainty derived within the investigation of STF50, the studied materials are rather insensitive to subcritical crack growth. For instance, materials that are prone to subcritical crack growth, such

as soda lime glasses, possess values of n lower than 18 [114]. Overall, the n parameters for STF-X materials are slightly lower than for other investigated membrane materials. For $Ba_{0.5}Sr_{0.5}Co_{0.8}Fe_{0.2}O_{3-\delta}$ and $La_{0.6}Sr_{0.4}Co_{0.2}Fe_{0.8}O_{3-\delta}$ it was reported that n ~ 30-40 and n ~ 24-49 [45, 116], respectively.

4.2.4 Lifetime predictions

Stress-probability-time (SPT) diagrams were derived for STF-X materials, since the sensitivity to subcritical crack growth was assessed. Figure 4-16 displays an example of a SPT diagram for a lifetime of 1 year of dense STF-X materials, assuming the same conditions of manufacturing process and effective volume of the samples tested in this work. However, the STP diagrams can be estimated for any pertinent time regarding the desired lifetime for membrane systems. The Weibull's modulus for each composition was considered to be the same value obtained in ring-on-ring tests at a loading rate of 100 N/min. The dashed lines in Figure 4-16 represented the upper and lower uncertainty bounds derived from the 95% confidence interval of the characteristic strength estimated at 100 N/min; the deviation of n was also considered. Table 4-9 summarizes the derived tolerated stresses by STF-X materials at distinct failure probabilities, according to the diagram displayed in Figure 4-16 (superscript is worst, subscript is the best case)

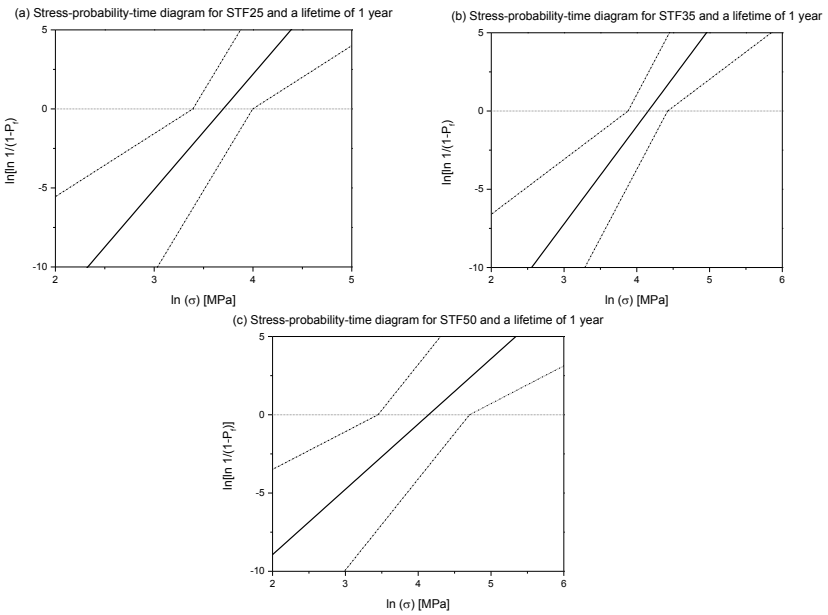

Figure 4-16 - SPT diagrams for a lifetime of 1 year: (a) STF25, (b) STF35, (c) STF50; the uncertainty intervals (best and worst case scenarios) are displayed as dashed lines.

Table 4-9 - Tolerated stresses for STF-X materials as a function of the failure probability for 1 year lifetime

	Tolerated stress σ [MPa]		
P_f	**STF25**	**STF35**	**STF50**
0.01	21^{+7}_{-6}	29^{+9}_{-7}	25^{+19}_{-13}
0.001	15^{+5}_{-4}	20^{+6}_{-5}	16^{+12}_{-8}
0.0001	11^{+4}_{-3}	14^{+4}_{-3}	10^{+8}_{-5}
0.00001	8^{+3}_{-2}	9^{+3}_{-2}	6^{+5}_{-3}

For further discussion of Figure 4-16, a minimum time of 1 year for operation is assumed for the membrane. In other words, every year the system has to be interrupted for monitoring and replacement of membranes to avoid in-operational failures. For this reason, the probability of failure within this 1 year must be kept low to avoid unpredicted system fallouts for maintenance. Hence, assuming a probability of failure of 10^{-3} for such a system STF, materials show similar

performance within the derived uncertainty, where the tolerated static stresses are 15^{+5}_{-4}, 20^{+6}_{-5}, and 16^{+12}_{-8} for STF25, STF35, and STF50, respectively.

4.2.5 Study on the uncertainty of the lifetime predictions

The relative uncertainty for the given lifetime of 1 year (circa 35% for STF25 and STF35 and more than 75% for STF50) unveils that the large scatter of strength, reflected in low m and broad confidence interval, have lowered the chosen method's accuracy. This scattering may be reduced by increasing the number of tested specimens and further scale up of the manufacturing technology towards industrial scale may increase the reproducibility of the manufactured structures. The tolerated stresses of STF-X materials as function of time with constant failure probability of 0.1% are derived from SPT diagrams and displayed in Figure 4-17 together with their respective relative uncertainty (uncertainty compared to the predicted stress) for the worst-case scenario. Here it is observed that this uncertainty increases for extended lifetime predictions as an effect of the strength scattering and SCG exponent error propagation.

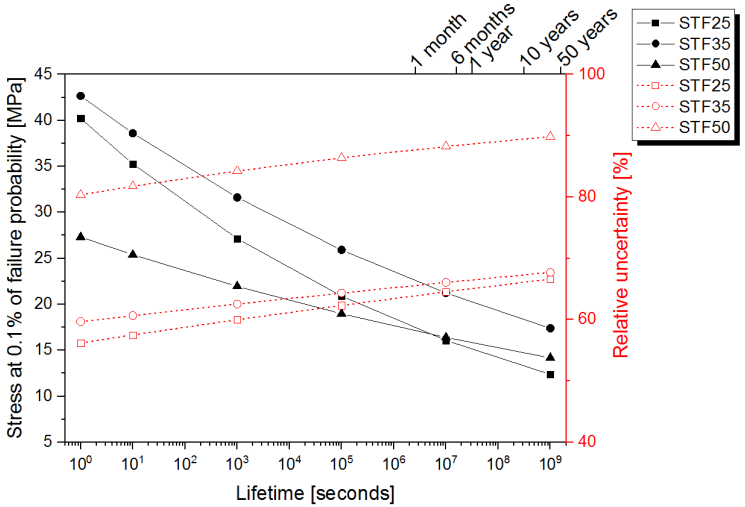

Figure 4-17 - Tolerated stresses at 0.1% failure probability and relative uncertainty at the worst case in function of the lifetime.

In conclusion, the interpretation of SPT diagrams can be very useful in regard to engineering design and development of strategies for quality assurance and failure prevention. Therefore, the SPT diagram presented in the current work may help designing a maintenance plan for membrane system using STF-X materials, once the lifetime is derived from the real stresses applied during operation.

4.2.6 Summary

The elastic behaviour, fracture toughness, and fracture strength of STF-X ceramics were investigated in the present section with respect to the influence of iron content in the mechanical properties of this class of materials. The final statements are presented below:

- The elastic modulus, obtained by depth-sensitive indentation testing and ring-on-ring flexural tests, shows no systematic tendency with respect to the Fe-substitution level within the experimental uncertainties.
- The average fracture stress is statistically the same for all STF-X compositions.
- The insensitivity to subcritical crack growth increases with Fe-content, however, being for all compositions on a very low level. Hence, all tested compositions are rather insensitive to subcritical crack growth.
- Time-dependent tolerated stresses for the investigated materials were also derived. For one year lifetime and a probability of failure of 0.1% STF25, STF35, and STF50 resist stresses up to 15 MPa.

4.3 Thermomechanical properties of dense $SrTi_{0.75}Fe_{0.25}O_{3-\delta}$

4.3.1 Apparent elastic modulus and fracture stress of dense STF25 at 900°C

Only STF25 was tested at elevated temperatures via ring-on-ring bending tests as representative for the STF-X materials, tests for porous materials at higher temperatures were not carried out since the materials behaviour should be comparable for dense and porous materials and the porosity effect at elevated temperatures should be the same as at RT. The results for the apparent elastic modulus E^* and average fracture stress σ_f assessed by ring-on-ring bending tests at 900°C and at distinct loading rates are displayed in Table 4-10. Note that the elastic modulus is time dependent and increases for faster loading rates and, therefore, the term "apparent elastic modulus" is preferred here. At the same time, a notable difference for the mechanical deformation Δ induced by stress can be seen at the stress-deformation curve for two distinct destructive tests displayed in Figure 4-18. Accordingly, the deformation that the specimen loaded at 100 N/min undergoes is smaller and rather linear when compared to a specimen loaded at 1 N/min. The distinct deformation might be a result of primary creep.

Table 4-10 - Mechanical properties of STF25 tape cast specimens at 900 °C.

Loading Rate	E^* [GPa]	σ_f [MPa]
1 N/min	53 ± 7	151 ± 12
100 N/min	85 ± 12	143 ± 16

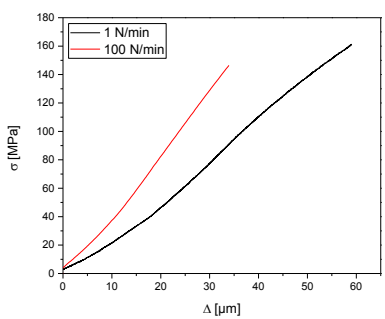

Figure 4-18 - Stress as a function of the deflection for STF25 tape cast specimens tested at 900 °C for distinctive loading rates.

Also, the fracture stresses determined at 1 and 100 N/min are similar considering the experimental uncertainty, with perhaps a slight tendency to decrease at higher loading rates. This indicates that the subcritical crack growth (SCG) sensitivity cannot be assessed at high temperatures as done for STF-X compositions at room temperature (see section 4.2). Indeed, as verified for the room temperature tests the estimation of SCG sensitivity aids lifetime prediction, since it joins the fracture strength and time. For this reason, in general, inferences in the lifetime of specimens loaded at room temperature could be obtained. However, the same indirect procedure for lifetime determination cannot be repeated for high temperature measurements.

Moreover, when these results are compared with the results reported in section 4.2, in which the fracture stresses were investigated for STF25 at room temperature, the average fracture stress increases considerably at 900°C. A comparison of the respective results is displayed in Figure 4-19. At this point, possible stress relaxations might be induced by anelastic behaviour. Such cause of anelastic relaxation has not been reported for STF25, hence, considering also the creep results that are reported later, it appears reasonable that the possible mechanisms unchaining anelastic relaxation is a result of primary creep. This might also contribute to the enhanced the apparent stability at higher temperature. Due to the high energy released at fracture, it was not possible to reconstruct the specimens at the test and identify the possible fracture origin, as done in Figure 4-14.

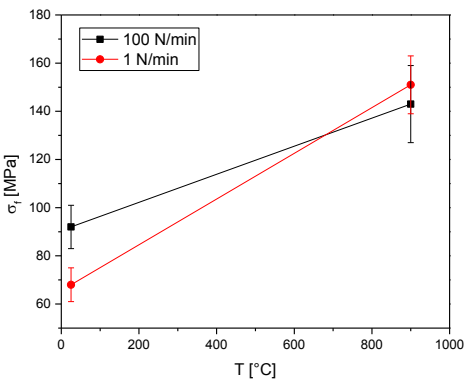

Figure 4-19 – Average fracture stress as a function of the temperature at distinct loading rates for STF25.

4.3.2 Impulse excitation technique study to identify the predominant mechanism for stress relaxation

The impulse excitation was used in the current work to determine the elastic modulus of dense tape cast samples and its coefficient of internal friction as a function of temperature. At room temperature, the obtained Young's modulus of a disc-shaped STF25 specimen is 136.0 ± 0.1 GPa, which is good agreement with the results obtained for this material with depth-sensitive micro-indentation, which yielded an Young's modulus of 147 ± 10 GPa. Following ASTM 1876-01, it was also possible to estimate the Poisson's ratio for such kind of specimen [144]. The Poisson's ratio obtained by interpolation of the resonant frequencies with results presented in the standard [144] is 0.239, hence, slightly larger than the 0.230 ratio reported for pure $SrTiO_3$ [113].

Figure 4-20 presents the Young's modulus obtained by impulse excitation technique as a function of the temperature. It is possible to see that the frequencies decrease quasi linearly with increasing temperature as can be seen in Figure 4-20, although there are indications of kinks at approximately 600°C and 800°C. Although the reason for these observed kinks is unknown, they may indicate a change in the elastic behaviour of STF25 materials. This change might be associated with the stress relaxations discussed in the previous section rather than a phase change. A phase change effect can be excluded, since STF-X compositions (X < 50) does not undergo phase transformations in the temperature range of 25 to 1000°C, according to the work of Stournari [98]. It is also noteworthy to mention that the specimen broke during cooling, indicating a possible micro-cracking during the test due to the continuously impulse hits, which might have influence on the observed kinks.

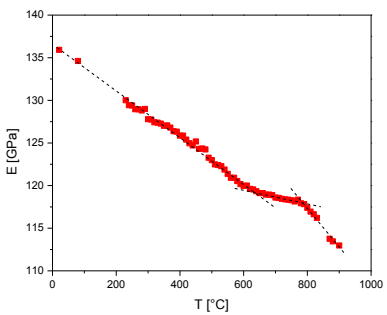

Figure 4-20 - Young's modulus as a function of temperature obtained by impulse excitation technique.

In order to study the unusual behaviour of the mechanical properties of STF25, the impulse excitation technique was repeated to investigate the variation of the internal friction with the temperature. The internal friction describes the force resisting the motion between the atoms of a solid material during deformation. Hence, the higher the coefficient of internal friction Q^{-1}, the greater are the forces resisting deformation. Also, the internal friction coefficient is an important property which gives information in respect to the anelastic behaviour of solids, as also discussed in Chapter 2.

The results of the internal friction coefficient experimentally obtained by impulse excitation and damping are displayed in Figure 4-21. As it can be observed the coefficient of internal friction increases from room temperature until 180°C, where a peak is observed. Afterwards, it shows a relatively small peak at 390°C, decreases to a minimum at 500°C and rises rapidly again from 700°C to 900°C. Therefore, this study reveals a tendency to anelasticity at temperatures in the range of 100 – 300°C and above 700°C, where the material might possess appreciable creep behaviour.

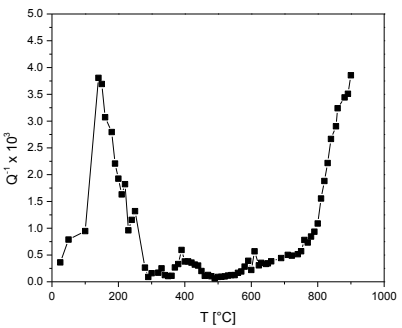

Figure 4-21 - Internal friction factor as function of the temperature.

As discussed in section 4.5.1, the reason for enhanced fracture stress of STF25 at 900°C compared to room temperature was attributed to anelasticity (creep), which promotes stress relaxations. Also, as mentioned in Chapter 2, undoped $SrTiO_3$ may have anelastic behaviour associated with oxygen vacancy hoping at 100 - 200 °C at reducing atmospheres [155].

According to [155], a loss peak was also observed in the range of temperatures between 100 and 200 °C and increases with decreasing oxygen partial pressure, i.e. increasing concentration of $V_O^{\cdot\cdot}$. Therefore, it is also possible that the observed peak in Figure 4-21 in the same temperature range is related to oxygen vacancy hoping since the iron doping in STF-X compositions enhance the concentration of these defects.

The second rise in the internal fiction coefficient above 700°C might be related to primary creep. In this case, the temperature may be high enough to promote dislocations movement and anelastic behaviour associates to the resisting deformation of a softer structure. Once again, the reason for a strong primary creep deformation might be related to the increased chemical defect concentration, such as oxygen vacancies, due to lattice oxygen release.

4.3.3 Summary

In the present section, results concerning the mechanical properties and its implications for STF25 specimens were assessed in regards to oxygen transport membrane application. The final remarks are summarized below:

- Mechanical properties of dense tape cast STF25 were obtained at high temperature by ring-on-ring flexural tests. The apparent elastic modulus revealed to be time dependent and increases with increasing loading rate.
- Average fracture stress estimated by ring-on-ring at different loading rates at 900 °C is higher than the result obtained at room temperature. A possibly explanation for this anomaly may be related to the anelastic relaxation or associated to primary creep.
- Impulse excitation tests confirmed the possibility of an existent anelastic behavior at high temperature and primary creep may be the cause for this effect.

4.4 Elasticity, strength, and reliability of porous $SrTi_{0.75}Fe_{0.25}O_{3-\delta}$ specimens

This section concentrates on the mechanical properties of STF25 porous supports obtained by different manufacturing techniques, aiming to derive the influence of microstructure on the mechanical stability of such supports. STF25 was chosen as representative for all STF-X, since overall the mechanical properties of the dense variants appeared to be similar and STF25 seems to be the worst case scenario (see Figure 4-17). Also, STF25 can be applied as substrate for oxygen transport membranes produced with STF35 or STF50, since these materials are compatible in terms of thermal expansion [11].

With respect to the mechanical properties of porous supports, specimens for the mechanical tests were obtained by tape casting, freeze-drying, and phase inversion tape casting. The fracture stress and reliability of STF25 porous samples were assessed through ring-on-ring bending tests at a loading rate of 100 N/min. This loading rate was chosen to mitigate the possible influence of subcritical crack growth on the obtained results. The thereby obtained Young's moduli E_{RoR}, average fracture strengths σ_f are displayed in Table 4-11, together with the average specimens' density ρ and pore length. For comparison among these properties, the specific Young's modulus E_{RoR}/ρ and specific average fracture stress σ_f/ρ were calculated. The results from tape cast dense STF25 specimens are also summarized in Table 4-11 for reference. Note that, indentation testing was not carried out for the porous materials since typically the macroscopic elastic modulus is more representative for the global behavior of the specimens, whereas the materials property was already assessed for the dense variations. Typically fracture toughness cannot be assessed for porous materials using indentation testing due to local crushing, however, a number of studies have verified that the porosity effect is similar for fracture toughness and strength [134, 154], hence, the current study concentrated on assessing the materials fracture stress. Also, for freeze-dried specimens, the dense regions observed in the as-received samples were removed before the tests (see section 3.2.2).

Table 4-11 - Average ring-on-ring tests results at a loading of 100 N/min.

Processing	ρ [g/cm³]	P [%]	E_{RoR} [GPa]	E_{RoR}/ρ [GPa·cm³/g]	σ_f [MPa]	σ_f/ρ [GPa·cm³/g]
Tape casting porous	3.52 ± 0.06	32 ± 1	35 ± 9	10 ± 3	52 ± 7	15 ± 2
Freeze-drying	3.60 ± 0.03	31 ± 1	39 ± 13	11 ± 4	22 ± 4	8 ± 1
Phase inversion	4.04 ± 0.08	22 ± 1	52 ± 9	13 ± 2	33 ± 9	8 ± 2
Tape casting dense*	5.07 ± 0.02	1.9 ± 0.3	108 ± 16	21 ± 4	117 ± 15	18 ± 2

*results from section 4.2

For the discussion of the results summarized in Table 4-11, the following assumptions are made:

i) Grain size and distribution are similar for all specimens manufactured by the different techniques, since sintering conditions were the same.
ii) Aside from the porosity and pore structure, the flaw concentration and distribution is the same for all specimens. These flaws include inclusions, impurities, second phases, etc.
iii) The gradient of porosity characteristic for phase inversion cast specimens does not have a key role on the determination of the mechanical properties, since these specimens were tested with the denser side (membrane side) at tension, i.e. the denser side was in contact with the support ring.

Therefore, the only variable in the microstructure of the tested specimens should be the porosity, pore size and its distribution. The normalized Young's moduli E_{RoR}/ρ are similar for all distinct specimens and smaller than the same normalized property obtained for dense tape cast specimens, indicating that the overall dependency of the elastic modulus is more complex than considered in the calculation of this simple ratio. In addition, the lower porosity of phase inversion cast specimens compared to tape cast and freeze-drying reflects a higher elastic modulus, but this is not valid for the strength. This result implies that the pore sizes do not have a significant influence on the Young's modulus, the porosity being the crucial parameter for the reduction of the elastic properties.

Contrarily to the Young's modulus, the average fracture stress appears to depend not only on the porosity, but also pore size, i.e. although stresses are increased by the reduced area /

volume of porous materials, failure is biased strongly by the largest defects whereas elastic deformation is an integral property related to all pores. As consequence, specimens containing pores with larger average length reveal a decreased mechanical stability. For instance, the specific average stress is statistically equal for dense tape cast and porous tape cast and is superior to the freeze-dried and the phase inversion tape cast specimens. The rather low specific average fracture stress of the specimens obtained by these last two methods is associated with the hierarchical porosity, characterized by channel-like long pores. This result was expected, since pores act as stress concentrators and, hence, reduce the resistance to crack propagation. Fractography analysis, however, was not possible because of the fracture surface irregularity to confirm if the introduced porosity is also the cause of fracture origin.

The distributions of the fracture stress of each single specimen as function of failure probability according to Weibull statistics are portrayed in Figure 4-22, where the 95% confidence interval is displayed graphically as dashed lines. The Weibull distribution parameters and their upper and lower confidence bounds are summarized Table 4-12. The characteristic strength σ_0 follows the same tendency as the average fracture strength and decreases with increasing pore length. The Weibull moduli, however, are statistically similar for all processing methods within the 95% confidence interval and are rather low, especially for phase inversion tape casting specimens. Since the Weibull modulus indicates the reliability in terms of fracture stress and it is direct related to the scattering of the obtained results (and maximum flaw sizes), lower m reflects the inhomogeneity on the studied materials. This is due to both limited maturity of the sample manufacturing process as well as low number of specimens per test series (10 against the minimum of 30 specimens, which is recommended for an accurate Weibull analysis). Therefore, improvement of the ceramic processing in direction of industrial mass production is required gaining a more homogeneous microstructure, where the porosity is better distributed and the flaws concentration is diminished.

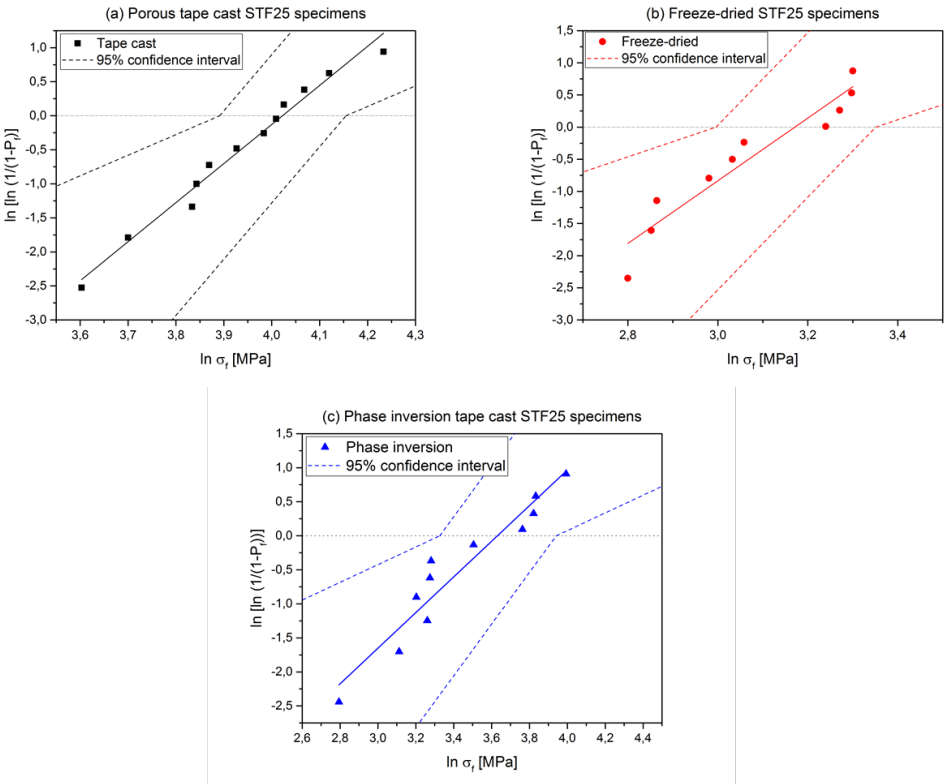

Figure 4-22 - Weibull distributions of the fracture stress of a) tape cast porous, b) freeze-dried, and c) phase inversion tape cast specimens.

Table 4-12 - Weibull distribution parameters for specimens obtained by distinct processing.

Processing	σ_0 [MPa]	*Lower (95%)/upper (5%) confidence bounds for σ_0 [MPa]*	*m*	*Lower (95%)/upper (5%) confidence bounds for m*
Tape casting	56	49/64	5.7	3.0/8.3
Freeze-drying	24	20/29	4.9	2.4/7.2
Phase inversion	38	28/52	2.6	1.3/3.8

Although the strength as a measure of mechanical stability of tape cast porous STF25 specimens is higher than the other investigated microstructures, the oxygen flux may be influenced by pore size and shape. Thus, in addition to the mechanical properties, the oxygen permeation should also be addressed in order to derive the performance of STF25 asymmetric

membranes. The results of permeation tests conducted on asymmetric membranes obtained by the three investigated processing methods is necessary to create a criterion for materials and microstructure selection.

4.4.1 Summary

In the current section, the impact of the microstructure on the mechanical stability of STF25 porous supports was addressed. The final remarks are:

- The distinct process routes lead to different critical flaw concentration and types, in this case, porosity and pore size. These flaws, although desired in a certain level for a positive effect on gas transport [38], are detrimental for the mechanical stability.
- The apparent Young's modulus decreases with increasing porosity and it is similar for all porous substrates, independent of the manufacturing method. Hence, the pore size does not appear to play a key role on the degradation of the elastic properties.
- The average fracture stress, on the other hand, is lower for the microstructures with the maximal pore length.

4.5 Anisotropic mechanical properties of $SrTi_{0.75}Fe_{0.25}O_{3-\delta}$ ice templated substrates

The mechanical properties of hierarchical porous oxygen transport membrane supports manufactured via freeze drying were also investigated as a function of the loading direction. In general a similar behaviour could be expected for the phase inversion method, hence the results might be considered to be representative for both. Here, particular emphasis has been given on the crack propagation in order to understand the mechanisms promoting fracture in the in- and out-of-plane directions. The studies are supported by characterizations via complementary acoustic emission detection and in-situ observation under scanning electron microscope during crushing tests. A newly developed scheme and theoretical model for fracture in each direction is discussed.

4.5.1 Apparent elastic properties and compressive strength

Compressive tests were used in current work to obtain the apparent elastic modulus and fracture stress of freeze dried specimens in two different directions: perpendicular (in-plane) and parallel (out-of-plane) to the freezing direction. As expected, the mechanical properties of freeze dried specimens are linked to the pore alignment and, thus, are distinctively depending on the loading direction. The load-displacement curves obtained from the compressive tests are presented in Figure 4-23. A kink is also observed typically in the curves obtained for the in-plane direction at higher loads, which might be related to pores collapsing.

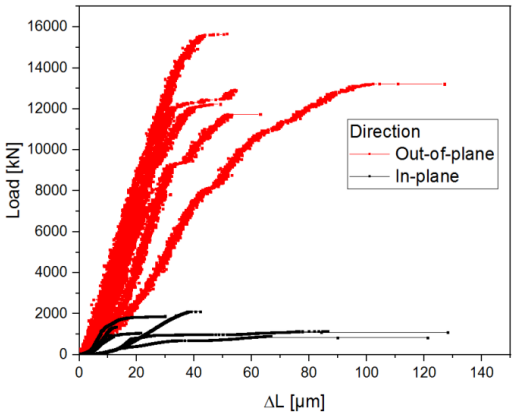

Figure 4-23 - Load-displacement curves obtained from the compressive tests.

The load-displacement curves shown in Figure 4-23 might be divided into three stages. At the start of the loading the specimen and sensors settle down in a limited low stress regime and this can be recognized by a non-linear load-deformation portion of some curves. This stage does not represent elastic deformation of the specimen and it is not considered in the derivation of the elastic modulus.

The second stage can be distinguished as a linear increase of the displacement as function of the load. This region of the curve appears to be the representation of the specimen's elastic behavior and its slope is used to derive the elastic modulus. As the loading continues, a third stage defined by a plateau is observed. This stage is typical for cellular materials [156, 157] and is featured by the collapse of the pore walls. Here, a critical load is reached, under which the pore walls show brittle fracture. At this stage, the deformation is not recovered by unloading, since the specimen has experienced fracture. Note, although the second regime is linked to the elastic modulus it will also be influenced by non-elastic effects related for example to failure of individual pore walls or micro-crack formation and hence a more accurate method to determine the elastic properties is the use of the unloading slope as discussed below.

Some authors [157, 158] mentioned the existence of a fourth stage for cellular materials that appears after the plateau (3^{rd} stage) with further load increase. At this point, the collapsed cell walls are compressed against each other causing densification. Therefore, the materials itself is compressed and the load-strain portion of the curve increases abruptly. This stage is not

observed in the load-displacement curves presented in Figure 4-23 since the mechanical test was stopped after this apparent specimens' failure.

Figure 4-24 displays the stress-strain curve during a loading/unloading cycle of a non-destructive compressive test in function of testing direction, where a hysteresis is observed. This hysteresis can be attributed to specimen's settle down effects, pore wall damage, unevenness of the sample, etc. For these reasons, the slope of the unloading curve is used to calculate the apparent elastic modulus E_{app}. The values of apparent elastic modulus E_{app}, average compressive fracture stress σ_c, and fracture strain ε as a function of the testing direction are presented in Table 4-13. Here, the out-of-plane direction is mechanically more stable under compression, where the apparent elastic modulus is three times higher and the fracture stress approximately five times higher. In addition, the deterioration in the mechanical stability of hierarchically porous structures is also in agreement with the studies of Lichtner et al. [149], who reported that the compressive fracture stress and elastic properties are circa 4 to 5 times higher for the out-of-plane direction. It is also noteworthy to mention that, during loading in both directions, permanent damage of the pore walls may occur. For this reason, even for small stresses (linear part of the load-displacement curves shown in Figure 4-23), the deformation may not be entirely recovered if the load is removed.

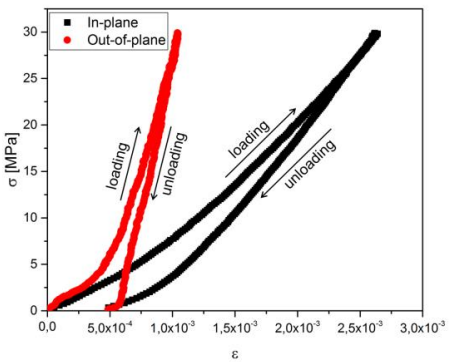

Figure 4-24 - Stress-strain curve showing a loading and unloading cycle in one specimen in both studied directions.

Table 4-13 - Compressive test results for freeze dried specimens as function of the testing direction.

Direction	E_{app} [GPa]	σ_c [MPa]	ε at fracture [%]
In-plane	18 ± 1	54 ± 14	0.4 ± 0.2
Out-of-plane	59 ± 2	273 ± 84	4.5 ± 0.9

The strain at fracture derived from the destructive tests (see Figure 4-23) reveals that the out-of-plane direction possesses a slightly higher tolerance for deformation before failure. Consequently, this strain tolerance may provide some advantages in the engineering design of membrane components. Indeed, oxygen transport membrane modules may have a complex architecture [28] and the thermal expansion mismatch of the ceramic membrane and module components may lead to failure. These mismatches can be certainly accommodated by the freeze-dried porous supports in the out-of-plane direction under compression. Moreover, as substrate for an asymmetric membrane, freeze-dried structures are still interesting, although the supported dense membrane layer is expected to be less strain tolerable. Despite, if the supported membrane layer is kept thin enough to enhance oxygen permeation (suggested in order of tens of micrometers thick [18]), the elastic energy release rate induced in the layer during the substrate deformation should be smaller than the fracture energy and hence prevent cracking [159].

In addition to the conventional compressive tests, further analysis of fracture behavior was conducted with help of acoustic emission recording and in-situ crushing test under scanning electronic microscope. The acoustic emission results for the in- and out-of-plane directions are displayed in Figure 4-25. For both cases, peaks of emissions are already detected in the early stage of loading and may indicate settling effects or friction, although damage on the pore walls before specimen's rupture is also possible. Accordingly, for the in-plane case, multiple events of high amplitude emissions are recorded for a stress of 26 MPa. At the later stage (above 70 MPa), a drop of stress occurs combined with a series of high amplitude peaks, which shows the start of the densification stage, where the collapsed pore walls are compressed against each other. On the other hand, for the out-of-plane loading, some low amplitude emissions are recorded in the very beginning of the test and retaken, with higher intensity, on the range of stresses between 150 and 200 MPa. Again, the first group of acoustic signals may be associated with settling effects between machine and specimen, whereas the later set of emissions may indicate the initial stage of failure. These emissions are more intense above 250 MPa.

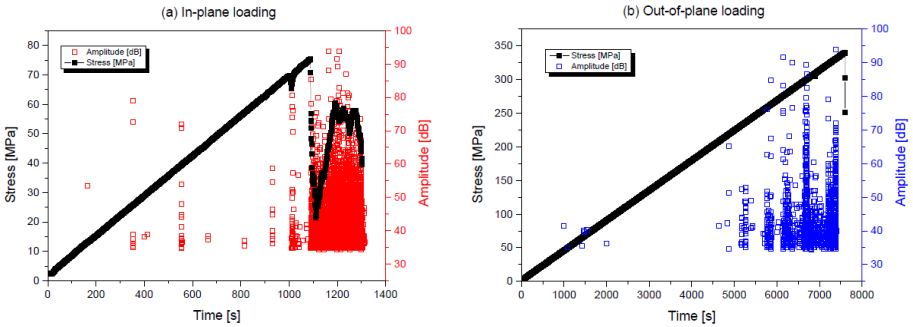

Figure 4-25 - Acoustic emission recorded during crushing tests, a) in-plane and b) out-of-plane loading.

In order to illustrate the occurrence of the anisotropic fracture behavior, in-situ electron microscopy images were captured during stepwise applied compressive loads up to 300 N. Figure 4-26 displays these results obtained for the out-of-plane direction. Under these conditions and after compressive load is applied, the pore walls begin to collapse, causing permanent damage. Figure 4-27, as well, presents scanning electron microscopy pictures of a similar compressive test, however, with load applied on the in-plane direction. The images show the evolution of damage of the porous structure after two sets of deformation. After the initial loading stage, it can be observed that, some pore walls start to fall apart. The same point is observed after subsequent second loading stage. At this stage, the previous damage propagates at 45° and the pore walls start to slide upon each other.

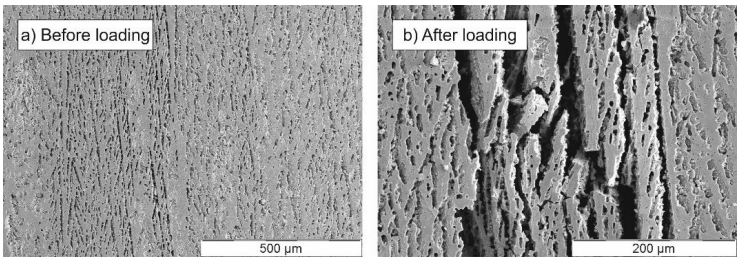

Figure 4-26 - SEM pictures of a loaded specimen in the out-of-plane direction, a) before and b) after a loading step.

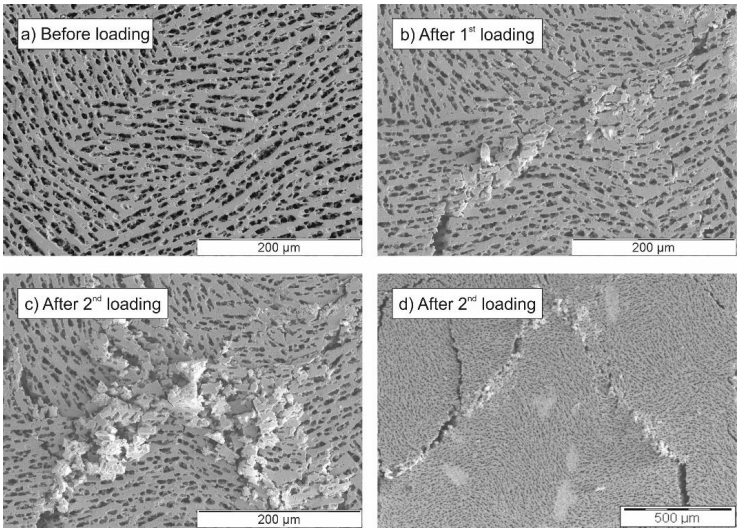

Figure 4-27 - SEM pictures of a loaded specimen in the in-plane direction, a) before loading , b) after first loading step, c) and d) same location after second loading step.

4.5.2 Applicability of distinct models for the fracture behaviour of ice templated structures

The results presented in the previous section revealed a large anisotropy of the mechanical loading limit of freeze dried specimens. Therefore, it can be expected that distinctively different fracture mechanisms occur for the different directions. The discussion of the possible fracture mechanisms is separated for the two cases and is presented below.

Elastic properties

Elastic properties in out-of-plane direction can be understood with a rough approximation adapted from the models for honeycombs from Gibson and Ashby [156, 157]. The authors derived the ratio between a material Young's E_s modulus and the elastic modulus of perfect hexagonal honeycombs in the out-of-plane direction E_{out}. In fact, according to this work this ratio is approximately equivalent to the relative density ρ^* of a perfect hexagonal honeycomb structure:

$$\frac{E_{out}}{E_s} \cong \rho^* \tag{4.3}$$

The Young's modulus of STF25 can be taken from previous results obtained in section 4.2.1 and is equal to 147 ± 10 GPa. In this case, the ratio E_{out}/E_s is equal to 0.40, which is slightly smaller than the relative density of the tested specimens (ρ^* = 0.55).

In the case of loading in the in-plane direction, each pore wall of a freeze dried ceramic may be submitted to a bending stress, similar to structural honeycombs [157]. Therefore, the total in-plane strain is a combination of the deformations of each pore wall lamella submitted to bending stresses due to the presence of a compressive stress. Gibson and Ashby [157] also derived for perfect hexagonal honeycombs the relationship between the elastic modulus of the perfect hexagonal honeycomb and the bulk material:

$$\frac{E_{in}}{E_s} \cong 2.3(\rho^*)^3 \tag{4.4}$$

From equations (4.3) and (4.4), the following relationship can be obtained:

$$\frac{E_{in}}{E_{out}} \cong 2.3(\rho^*)^2 \tag{4.5}$$

The ratio calculated with equation (4.5) is 0.70, which is rather higher than the ratio between the apparent elastic moduli obtained experimentally and displayed in Table 4-13, being 0.31. Ideally Gibson's and Ashby's approach can only be used in the case of freeze-dried structures with a geometry correction factor, since the pores deviate from perfect hexagons. However, the derivation of such factor is not included in the scope of this work. Still, this approach aids the understanding of the materials behavior, illustrating that the in-plane mechanical properties have to be inferior.

Also, comparing the apparent elastic properties obtained in flexural tests, as described in section 4.2.2, these lie between the apparent elastic moduli derived in the compressive tests as function of the different loading direction. In this case, the stress distribution during a bending

loading varies from compression to pure tensile within the sample thickness. Therefore, the mechanism of deformation in each pore wall is distinct depending on the local stress, influencing the derived apparent elastic properties.

Out-of-plane fracture mechanism

The out-of-plane fracture behavior of freeze dried specimens was investigated by Porter et al. [160], who suggested that the fracture due to uniaxial compressive loading is caused by pore wall buckling. Therefore, the compressive strength may be estimated by a modified Euler's buckling equation and is a function of the pore aspect ratio $\chi_p = a/b$ [160, 161]:

$$\sigma_{cr} = \frac{\pi^2 q^2 E}{(kL)^2}\left[\frac{A_s^2}{3b^2}\left(\frac{1}{\chi_p}\right)^2 + \frac{A_s}{2}\left(\frac{1}{\chi_p}\right) + \frac{b^2}{4}\right] \tag{4.6}$$

where E is the material's elastic modulus, q is an empirical factor that incorporates experimental unknowns, k is a constant related to the geometry of the ends (assuming that the pore ends are fixed, $k = 0.5$), L is the pore length, and $A_s = a \cdot t$ is the lamellar wall cross-sectional area.

Equation (4.6) shows that the out-of-plane compressive strength of freeze-dried structures decreases with the pore length. Considering this fact, it is expected that the longer pores in the tested specimens break first and may be the cause for fracture. Therefore, with help of equation (4.6), a rough estimation of the compressive stress, can be derived. Here, the worst case predicted by the model occurs for the longest pore walls, which are in the range of 27 µm (see Table 3-2). In this case, for the results of pore geometries displayed in Table 3-8 and the elastic modulus of 147 GPa reported for STF25, the estimated minimum fracture stress, for A_s = 80 µm² and χ_p = 2, is σ_{cr} = 120 MPa. This result is substantially lower than the experimental outcome of 273 ± 84 MPa obtained in the crushing tests. However, the acoustic emission results displayed in Figure 4-25 show that the pore walls fracture already for stresses below 200 MPa, which may be associated to isolated pore wall failures. Also, although not discussed here, shear stresses may appear on the pore walls, causing earlier rupture.

The hypothesis of pore wall buckling is also confirmed by the in-situ compressive test performed in a scanning electronic microscope. In Figure 4-26, it can be observed that the walls

collapsed apparently by unstable deflection, suggesting that the wall fracture occurred by buckling. This may also indicate the reason for higher mechanical parameters in this direction. Here, the pore walls act together as columns constricting the deformation and the permanent damage appears first at higher stresses when compared to the in-plane direction.

In-plane Fracture mechanism

Considering that the pore walls are submitted to bending stresses, the crack in such structures may start once one or more pore walls fail because their module of rupture has been reached. A schematic representation of the loading effect in each pair of parallel pore walls is suggested in Figure 4-28.

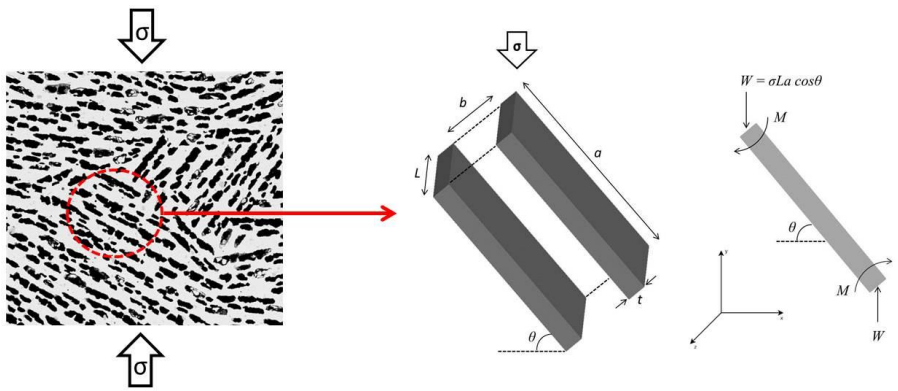

Figure 4-28 - Schematic representation of uniaxial compressive load in a freeze dried structure in the direction perpendicular to the ice growth.

From the state of stresses depicted in Figure 4-28, the forces loading each pair of pore walls may be written as:

$$W = \sigma La \cos\theta \tag{4.7}$$

where σ is the stress compressing the bulk and θ is the rotation angle of the pores in relation to the this stress. Similarly, the force moment arising from the loading is:

$$M = \frac{Wa\cos\theta}{2} \tag{4.8}$$

Therefore, from the applied mechanics, pore wall fails once the maximum tensile stress exceeds the module of rupture [157]. This maximum tensile stress is caused by a maximum force moment M_{max}, which is given by:

$$\sigma_f = \frac{M_{max}y}{I} = \frac{M_{max}(b+2t)}{2I} \tag{4.9}$$

where I is the area moment of inertia. Substituting equation (4.7) in equation (4.8) and implying that pure brittle fracture occurs, it can be shown that:

$$\sigma_{cr} = \frac{2M_{max}}{a^2 L\cos^2\theta} \tag{4.10}$$

where σ_{cr} is the compressive fracture stress.

Furthermore, the area moment of inertia for the represented pair of pore walls is estimated by [162]:

$$I = \frac{L}{12}[(b+t)^3 - b^3] \tag{4.11}$$

Granted that the equations (4.9), (4.10), and (4.11) are combined, the ratio between the compressive strength of freeze dried specimens and the bending module of rupture can be derived:

$$\frac{\sigma_{cr}}{\sigma_f} = \frac{(b+t)^3 - b^3}{3a^2\cos^2\theta\,(b+2t)} \tag{4.12}$$

Finally, the crushing stress predicted by equation (4.12) is a function of the orientation of the pore walls. For example, the smallest crushing stress estimated with this relationship occurs for θ = 0°. Indeed, it is also suggested that the pore walls collapse before the material's failure,

which indicate that the first walls that break are the ones oriented at $\theta = 0°$. Moreover, equation (4.12) depicts that increasing the pore wall thickness t and decreasing the pore width a are effective ways to enhance the in-plane compressive fracture stress.

Nevertheless, an accurate prediction of the material failure is not trivial through equation (4.12), once the pores in this plane are randomly oriented with respect to the normal loading and the pore geometry has an arbitrary distribution with large deviation (see Table 3-8). Also, the module of rupture σ_f cannot be predicted due to the small volume of the pore wall. Despite, an insight of the effect of pore dimensions and orientation can be presumed with the suggested relationship. Of course the less mechanically stable walls are the ones with the minimum thickness and largest width. In the worst-case scenario, these walls are the first to be damaged with increasing compressive stress, provided all walls have the same density.

The verification of the suggested model can be done by altering the structure properties, such as pore wall thickness and pore geometry. Add to this, the determination of the material properties for the pore wall small volume is still necessary for a more precise prediction of the in-plane compressive stress. These also aid the understanding of the exact fracture mechanism and the optimization of the proposed equations. Withal, the proposed model might assist the derivation of the mechanical stability for distinct hierarchically porous microstructures.

4.5.3 Summary

The mechanical properties anisotropy of freeze-dried porous supports was addressed in this section, with special emphasis on the fracture mechanism as a function of the loading direction. The final remarks are:

- The apparent elastic modulus obtained in the loading in the out-of-plane direction is around three orders of magnitude larger than the respective property in the in-plane direction, while the average fracture stress is around a factor five larger.
- Acoustic emission and in situ compressive tests under a scanning electronic microscope revealed permanent damage of the pore walls compressed in both studied planes even before complete failure of the sample.
- In-plane and out-of-plane fracture initiation and propagation were observed at the in situ compressive test. Pore wall collapsing through buckling is most likely the main reason for

fracture initiation in the out-of-plane direction, while the pore walls rupture in the in-plane direction is caused by bending.

- An equation to predict the failure in function of the pore orientation for the in-plane direction was suggested.

4.6 Creep behaviour of dense and porous of $SrTi_{0.75}Fe_{0.25}O_{3-\delta}$

One critical mechanical characteristic for oxygen transport membrane application is creep deformation, once it induces structural instability and may cause failure in the long-term operation. The steady-state creep deformation rate was investigated for STF25 specimens produced by three different methods: pressing, tape casting with pore formers, and freeze drying. For the later one, creep behaviour was studied in different directions, since it was verified that the mechanical stability is anisotropic with respect to the pore orientation.

For all tested samples, a strong primary creep deformation has been observed in the initial 5 hours of load application. An example of a creep curve, i.e. strain in function of time can be found in the Appendix D (Figure D-1). For instance, at 950 °C and under a compressive stress of 15 MPa, rapid nonlinear deformations of ~ 0.06%, 0.3%, and 0.6% are perceived for the pressed, tape cast, and freeze-dried specimens, respectively, after the first five hours of test. These high primary creep deformations may have great influence on the fracture mechanical behaviour of STF25 at high temperatures. As addressed in section 4.5.1, the average fracture stress at 900 °C increases when compared to room temperature experiments. The reason was attributed to stress relaxations due to possible anelastic behaviour caused by primary creep. After the creep tests and aided by the studies on the internal friction coefficient (see Figure 4-21), anelasticity seems to arise from primary creep and may be responsible for the enhanced mechanical properties of STF25 at high temperatures.

The steady-state creep rates for the distinct studied STF25 specimens are summarized in Table D-1 (Appendix D). As expected, the creep rates are lower for the dense materials (pressed) than for the porous (tape cast and freeze dried) at the same temperature and stress. This difference accounts to circa one order of magnitude. With respect to the freeze-dried specimens, the creep rate is comparatively higher for the in-plane direction (pores perpendicular to the loading direction), where it can be up to 20 times higher than the out-of-plane direction. This reflects again lower mechanical stability compared to the out-of-plane properties.

In general, STF25 seems to be more resistant in terms of steady-state creep when compared to other membrane candidates. For example, reported steady creep rates for dense BSCF and dense LSCF were $4.9 \cdot 10^{-8}$ s^{-1} and $1.5 \cdot 10^{-8}$ s^{-1}, respectively, at 900 °C and under 30 MPa [26, 118]. Under these same conditions, the dense STF25 steady-state creep rate is

comparable to dense STF30, for which $8.0 \cdot 10^{-9}$ s^{-1} has been reported [98]. However, an accurate comparison is not feasible, since the average grain sizes of both studied materials are different (approximately 0.5 µm for STF25 and 8 µm for STF30 [98]). The experimental uncertainties for the creep rates are derived from the linear fitting of strain-time curves. However, it was also demonstrated before that the experimental uncertainty is in the range of 20% for multiple tests under the same conditions [98].

The creep rates normalized with respect to the relative density ρ^* for an applied stress of 30 MPa are displayed in Figure 4-29. According to these results, the out-of-plane steady-state creep rate of the freeze-dried specimen is comparable to that of the tape cast specimen, even though the pore size in the latter case is smaller (for more details, see Chapters 3 and 4). The 1% strain per year restriction discussed in Chapter 2 is also displayed in Figure 4-29 and STF25 specimens do not reach values close to this limitation. Still, design modifications that reduce the stress during membrane operation may enable the application of the investigated mixed ionic electronic conductors.

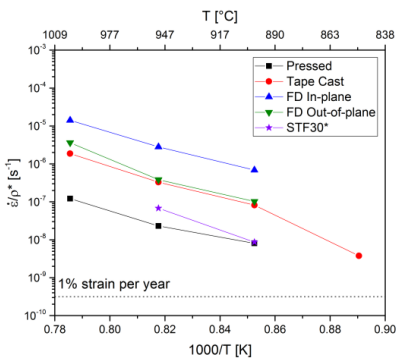

Figure 4-29 - Normalized creep rates by relative density under 30 MPa applied stress; *corresponds to the results in [98].

4.6.1 Correction of creep rate for porous materials

Porosity usually increases the deformation rate during the steady-state creep, since pores reduce the effective area of the specimen and pore walls may concentrate stresses, elevating the creep rate [163, 164]. In this case, the macroscopic applied stress is locally intensified at the pore walls, once their contact area (local where stress is transferred) is small leading to locally higher

stresses [165]. Hence, the applied stress is intensified by a stress intensification factor φ ($\varphi \geq 1$), increasing the steady-state creep rate, which may be described by the relationship [165]:

$$\dot{\varepsilon} = A\left(\frac{1}{d}\right)^{m}(\varphi \cdot \sigma)^{n}\exp\left(-\frac{E_a}{RT}\right) \tag{4.13}$$

The existence of a stress intensification factor was already used in the modelling of the densification process of hot pressing and electric field-assisted sintering [165-167]. In this case, the linear deformation rate $\dot{\varepsilon}$ of the specimen during sintering is directly related to the densification rate. In the current work, the intensification factor φ is assumed to be simply equal to $1/\rho^*$, $0 \leq \rho^* \leq 1$ being the relative density. Note that the correct estimation of the stress intensification factor may require use of finite elements simulation, as discussed by Montes et al. [166] which, however, is not within the scope of this work. Granted that the real local stresses may be intensified, the strain rate for the porous specimens was corrected by the equation (4.13), i.e. the creep rate was derived as function of the calculated apparent intensified stress.

4.6.2 Steady-state creep parameters

The creep rates as a function of the temperature and applied corrected stress for the tape cast porous specimens are displayed in Figure 4-30 (a) and (b). In fact, as mentioned before, the real stresses in low density bodies, such as tape cast and freeze-dried specimens, are intensified due to the smaller contact area between particles. For this reason, the corrected stresses in Figure 4-30 were obtained by simply multiplying the applied stress by $1/\rho^*$, where ρ^* is the specimen's relative density. According to an Arrhenius' fitting of the creep rate logarithm in function of the inverse temperature, the activation energy for creep is 453 ± 30 kJ/mol. Similarly, the linear fitting of the creep rate logarithm in function of the applied corrected stress logarithm yielded a stress exponent of 3.5 ± 0.7. This value outlines that the mechanism controlling steady-state creep for STF25 is associated with dislocation glide/climb [120], which means that creep rate should be independent of grain size. Here, it is important to notice that the significant uncertainties of the creep parameters arise partly from the apparent small specimen's deformation, which lies within the compliance of the testing equipment.

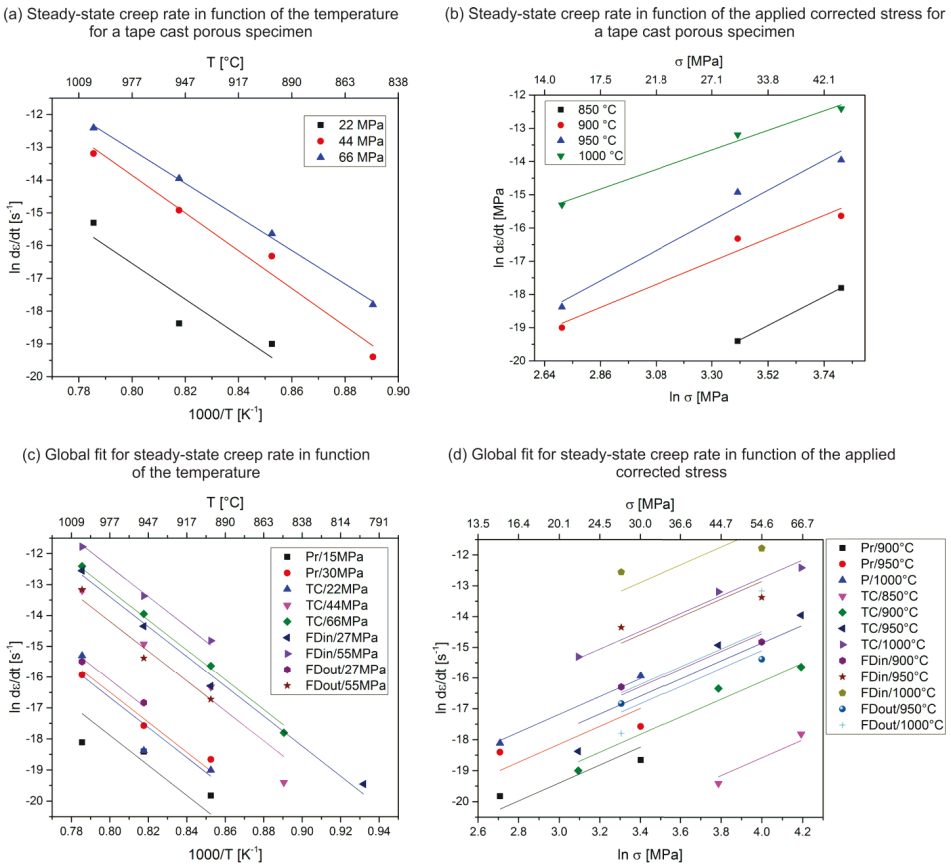

Figure 4-30 – (a) Arrhenius' fitting the steady-state creep rate in function of temperature and (b) linear fitting of the applied corrected stress for a tape cast porous specimen; (c) and (d) correspond to a global fit of the steady-state creep rate of all tested specimens. Pr, TC, FDin, and FDout correspond to the pressed, tape cast, freeze-dried (in-plane), and freeze-dried (out-of-plane) specimens, respectively.

With the purpose to estimate the creep parameters of STF25, despite the limited experimental data, it is reasonable to assume that the activation energy and stress exponent is a material property and invariable with the microstructure. This assumption is reasonable, once the diffusing specimens and diffusion paths should be the same and porosity does not influence the stress exponent [43, 168]. Therefore, these parameters can be obtained via global fitting of the creep rates as function of temperature and applied corrected stresses for all experimental data, i.e. all specimens. The global single slope fittings are displayed in Figure 4-30 (c) and (d) and yielded an activation energy of 402 ± 25 kJ/mol, which is lower to some extent than reported for STF30

(477 ± 22 kJ/mol) [42]. The obtained activation energy might relate to cation diffusion once it lies within the range of the activation energies for self-diffusion of Sr^{2+} and Ti^{4+} in perovskite related structures [128, 169, 170].

The derived stress exponent of 2.9 ± 0.4 confirms that steady-state creep for STF25 is mainly controlled by dislocation mechanisms, although a small contribution of diffusional creep should not be excluded. Also, for the similar composition STF30, the reported stress exponent was equal to 2.4 ± 0.2 at 950°C [42], which agrees with the results in the current work. More important, the creep parameters obtained through global fitting of the experimental data agree with the values obtained for the tape cast porous specimen alone. Therefore, regardless of the limited creep data for each single specimen, a global fitting may be a good approach for the estimation of the steady-state creep parameters.

The microstructure of the specimens post creep tests can be seen in Figure 4-31, where the SEM images of the polished cross-sections of these specimens are portrayed. The pressed and tape cast specimens appear to have no alteration in the microstructure. The freeze-dried specimens, on the other hand, possess cracks along the pore walls. These cracks may have originated through the mechanisms already discussed in Chapter 5. Accordingly, the damage in the pore walls appears before the critical fracture stress due to bending/buckling forces, which was observed in an in-situ crushing test. These mechanisms may also explain the reason for enhanced creep deformation resistance in the out-of-plane direction.

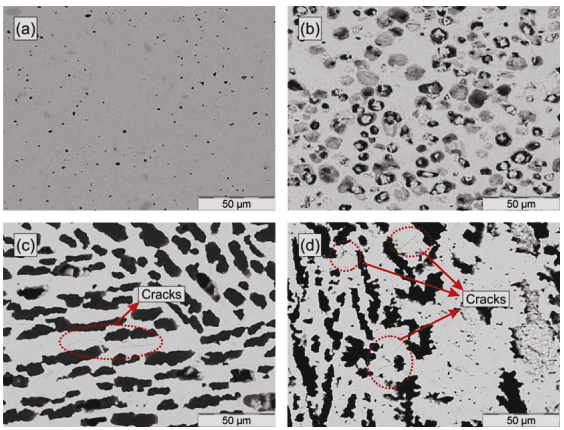

Figure 4-31 - Polished cross-sections of the specimens after the creep tests: (a) pressed, (b) tape cast, (c) freeze-dried in-plane, and (d) freeze-dried out-of-plane. Cracks can be observed in the pore walls in (c) and in (d).

Changes in the grain size and texture of the tested samples were investigated using EBSD. The EBSD orientation map obtained for the pressed STF25 specimen, in the cross-section parallel to the loading direction, is displayed in Figure 4-32. The EBSD maps obtained for the other tested specimens can be found in the Appendix E. The orientation maps correspond to an inverse pole figure (IPF), in which each colour correlates to a specific crystal orientation according to the Euler angle based colour scale. The IPF maps show no preferential grain orientation or texture that could arise from a non-uniform long-term applied stress at the testing temperatures. In this case, it can be assumed that the material had undergone homogeneous deformation. Furthermore, the grain size was obtained by analysis of the EBSD orientation maps and is 0.5 ± 0.4 µm, 0.4 ± 0.2 µm, 0.5 ± 0.3 µm for the pressed, tape cast and freeze-dried specimens, respectively. According to these results, the grain size is statistically similar for all tested specimens. At last, grain elongation, which is typical observed for diffusional creep, is not observed in Figure 4-32 or in any other EBSD orientation map obtained for the tested specimens.

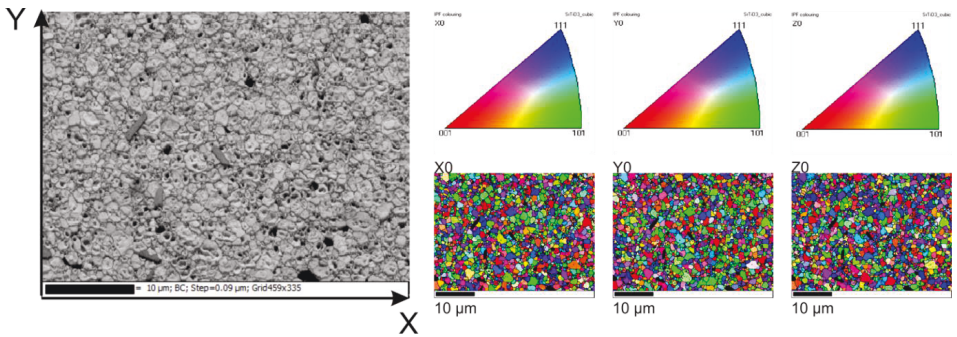

Figure 4-32 - EBSD orientation map for the pressed STF25 specimen after creep test.

4.6.3 Summary

Creep behaviour, which is an important characteristic for the membrane operation, was investigated for dense and porous STF25 specimens. The final assertions are:

- Creep tests were conducted for dense and porous STF25 specimens obtained by tape casting and freeze-drying. As expected, the creep rates obtained for porous samples were much higher than for dense samples.

- Anisotropy was observed for the creep results of freeze-dried specimens with respect to the tested direction.
- Activation energy and stress exponent were obtained via global fitting of all creep rates investigated at different temperatures and applied stresses, which seems to be a good approach to describe the material's creep behavior. The results derived this way were 402 ± 25 kJ/mol for the activation energy and 2.9 ± 0.4 for the stress exponent.

CHAPTER 5 Conclusions and Outlook

The study and understanding of the mechanical behaviour of oxygen transport membranes and supports is necessary to aid materials selection and engineering of optimized microstructure and designs. For this purpose, the class of materials based on the system **$SrTi_{1-x}Fe_xO_{3-\delta}$ (STF-X)**, with x = 0.25, 0.35 and 0.5 was systematically investigated in regards to its processability by distinct industrial relevant methods and mechanical stability at the possible membrane operation conditions.

The developed processing method concentrated on scalable powder production via solid state reaction. According to the powder characterization, this rather simple and economic viable method verified to be successful for the necessary batch production of STF-X powders in kilogram-scale. The desired single cubic perovskite phase was obtained for all compositions by heat treatment at 1100 C. Also, the powder properties, such as particle size distribution and surface area, were tailored by wet milling according to the needs of the further processing steps.

Tape casting was selected in this work in order to obtain dense reference samples for the study of the STF-X elasticity and strength in function of the iron content. As desired, specimens with porosity smaller than 5% were successfully obtained. The average grain sizes of the sintered samples were in the range of 1.2 – 1.4 μm for STF25 and STF50, while STF35 remained with a finer grained structure with average size of 0.6 μm. Moreover, suitable STF25 porous specimens, essential for the applicability of supported asymmetric membranes, were successfully implemented through tape casting, freeze-drying, and phase inversion tape casting. Indeed, the use of 30 wt% corn starch as pore former in the conventional tape casting procedure yielded an apparent porosity of 32%, which remains in the desired level for employment as porous support. Furthermore, hierarchically porous specimens with a channel like porosity of 31.8 ± 0.5% across the specimen thickness were produced via freeze-drying. Phase inversion tape casting, on the other hand, leads to a finger-like porosity in the range of 22%.

The final remarks with respect to the mechanical properties are summarized separately below for each distinctive aim of the current work.

Influence of iron content on the mechanical properties of dense STF-X materials

With the purpose to understand the influence of iron doping on the mechanical stability of STF-X materials, the elastic behaviour of dense tape cast specimens of each compositions were investigated in the present work. The elastic modulus, obtained by depth-sensitive indentation testing and ring-on-ring flexural tests, shows no systematic tendency with respect to the Fe-substitution level within the experimental uncertainties. Nano-indentation results also confirm this trend, although the maximum elastic modulus obtained by the technique shows a tendency to decrease with increasing iron content. Withal, this dependence disappears for the effective mechanical properties of the specimens measured using macro-mechanical methods.

In regards to the mechanical stability of STF-X components, the fracture stress was assessed via ring-on-ring bending tests. The results reflect no compositional effect, being the microstructure the crucial factor influencing the strength. The insensitivity to subcritical crack growth, however, appears to increase with Fe-content, although it remains for all compositions on a very low level. A worst-case scenario based on the confidential interval taking the empirical uncertainty in account, shows a tolerable static stress for STF35 of 20 MPa for a lifetime of 1 year and a failure probability of 0.1%. This load would qualify STF35 for small-scale applications with regular maintenance intervals of less than 1 year. Still, the lifetime prediction approach described in this work must be adapted to loads defined by realistic membrane module design and application conditions.

Enhanced fracture stress of dense STF25 at 900 °C

The mechanical stability of STF25 was investigated close to the suggested oxygen transport membranes operation conditions, i.e. elastic behaviour and fracture stress at 900 °C. These properties were assessed for dense tape cast STF25 specimens by ring-on-ring flexural tests at two distinct loading rates. The apparent elastic modulus increases with increasing loading rates, which appears to be time dependent. In addition, average fracture stress estimated by ring-on-ring at different loading rates at 900 °C is 143 ± 16 MPa, which is considerable higher

compared to the same property at room temperature for the same specimen type (92 ± 8 MPa). These results indicate a possible anelastic behaviour acting towards stress relaxation.

This unexpected anelasticity was further confirmed by impulse excitation tests at increased temperature, where the coefficient of internal friction was obtained from the damping curves. In fact, the coefficient of internal friction showed a peak at 180 °C and 390 °C and increases above 700 °C, revealing the range of temperatures where anelasticity might occur. Although the actual reason for the reported anelastic behaviour is still unknown, primary creep may be the cause for the increase beyond 700 °C and the loss peaks at 180°C and 390°C may be associated to oxygen vacancy hopping. However, to ensure this assumption, impulse excitation tests need to be repeated under lower oxygen partial pressures. If the internal friction peaks become more eminent under this condition, the hypothesis of oxygen hopping unchaining anelasticity might be confirmed.

Influence of porosity and pore structure on the mechanical properties of STF25 porous supports

The mechanical stability of STF25 porous supports obtained by distinct manufacturing methods was assessed with ring-on-ring bending tests. The apparent Young's modulus appears to decrease with increasing porosity, as the distinct methods derived different relative densities. Granted that, phase inversion tape cast specimens showed the highest Young's modulus, derived from the densest microstructure.

The average fracture stress, on the other hand, is lower for the microstructures with the largest pore length. Hence, phase inversion tape casting shows the weakest samples. This result is expected, since pores act as stress concentrators decreasing the mechanical stability. Nevertheless, as exemplified by the experimental results for STF25, STF-X asymmetric membranes obtained by any of the investigated manufacturing methods are still attractive, since the mechanical stability appears to satisfy the demands in real applications [169, 170].

With respect to the fracture strength, tape cast specimens showed the best results. However, the microstructure influence of the porous support on the oxygen permeation rates must be evaluated to face the trade-off between mechanical stability and transport properties regarding gas exchange.

Anisotropic mechanical properties of freeze-dried porous STF25

Mechanical properties of hierarchical porous oxygen transport membrane supports manufactured via freeze drying are investigated as a function of the loading direction, exemplified for STF25. Indeed, the mechanical stability of freeze-dried specimens displays anisotropy, where the mechanical stability in the in-plane direction (load applied perpendicular to the pores) appears to have a lower stability. The studies were supported by characterizations via complementary acoustic emission detection and in-situ observation inside a scanning electron microscope during crushing tests. These investigations revealed permanent damage of the pore walls compressed in both studied planes already at half of the failure stress.

In order to understand the mechanism of fracture in each plane, a newly developed scheme and theoretical model for fracture in each direction was discussed. Out-of-plane (load applied parallel to the pores) fracture starts with pore wall collapsing through buckling, which was also confirmed by the in situ compressive test. The pore walls rupture in the in-plane direction is caused by bending mode and an equation to predict the failure in function of the pore orientation is suggested. Indeed, the main influencing factors on the mechanical stability could be extracted and the model aids, as guideline, the processing of hierarchically porous supports. Withal, future works concerning the investigation of the reported anisotropy as a function of porosity and pore structure, such as variable pore wall dimensions, can support the theoretical models.

Creep behavior of dense and porous STF25

Another important characteristic for the membrane operation is the resistance to creep deformation. Indeed, membranes could face relative high-pressure gradients at high temperatures, depending on the application. For this reason, steady-state creep was investigated for STF25 membrane and substrate materials obtained by distinct manufacturing methods.

The activation energy for the creep process, as well as the stress exponent, were obtained for a tape cast porous STF25 specimens by single linear fittings of the experimental data. The activation energy for steady-state creep derived this way is 453 ± 30 kJ/mol and the stress exponent is 3.5 ± 0.7. In addition, a global slope fitting was applied separately for the creep data

for all material variants, which is a reasonable approach in order to describe the creep behaviour and overcome the rather large uncertainties due to the limited experimental data for each single tested specimen. This approach yielded an activation energy of 453 ± 30 kJ/mol and a stress exponent of 2.9 ± 0.4, implying that STF25 might undergo dislocation creep.

The microstructure analysis after creep tests via SEM and EBSD showed no noticeable change and IPF orientation maps also indicate that the grains have not acquired a preferential texture after the test, emphasizing the hypotheses of dislocation creep. Freeze-dried specimens, on the other hand, possessed cracks on the pore walls. This might be a consequence of the mechanisms of fracture that these structures undergo, as verified at room temperature, than rather a consequence of creep.

Outlook

Collectively concluding, STF-X is a promising candidate as oxygen transport membrane material and the data presented here can aid the designing process of module layout tailored to a specific application. Still, further investigations addressing the STF-X mechanical properties would aid its potential application in gas separation components. Therefore, it is suggested that, for the upcoming studies in the system STF-X, the following points should be covered (also illustrated in Figure 5-1):

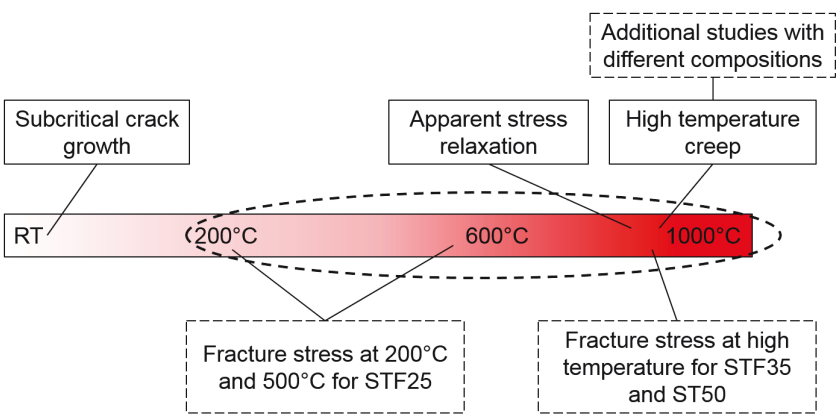

Figure 5-1 - Outlook on the mechanical characterization of STF-X materials.

- The mechanical properties of the compositions STF35 and STF50 at high temperatures (above 800 °C) must be obtained, gathering information on fracture stress and creep behaviour.
- The fracture stress of STF-X materials should be studied at 200 °C, where a loss peak was reported in the impulse excitation testing, and at 500°C, where the intern friction reached its minimum. Desired is also the fracture stress and coefficient of intern friction under lower oxygen partial pressures. The mechanical behaviour obtained under these conditions aids the understanding of the unexpected increasing in the fracture stress.
- Also desired is a study on controlling creep deformation by adding barriers to dislocation climb/glide. In this case, a small addition of precipitates might enhance the resistance to creep deformation for STF-X based ceramics.
- With respect to the porous substrates and development of asymmetric membranes, the gas permeation flux in these structures should be assessed. This investigation may support the development of a criterion for material and microstructure selection based on functional and mechanical performance.

List of symbols

Category	Symbol	Description
Oxygen transport through a membrane	j_{O_2}	Oxygen flux [mol·m^{-2}·s^{-1}]
	R	Universal gas constant [8.314 J·mol·K^{-1}]
	T	Temperature [K]
	F	Faraday constant [96485.3365 C·mol^{-1}]
	L	Length [m]
	p_{O_2}	Oxygen partial pressure
	σ	Conductivity [S·m^{-1}]
	L_C	Characteristic thickness [m]
	D	Diffusion coefficient [m²·s^{-1}]
	k	Surface exchange coefficient [m·s^{-1}]
Stress and strain	E	Young's modulus [GPa]
	σ	Stress [MPa]
	ε	Strain [-]
	σ_f	Fracture stress [MPa]
Weibull statistics	σ_0	Characteristic strength [MPa]
	P_f	Probability of rupture [-]
	m	Weibull's modulus [-]
	C_l	Characteristic strength lower bound [MPa]
	t_l	Lower bound constant for the characteristic strength [-]
	C_u	Characteristic strength upper bound [MPa]
	t_u	Upper bound constant for the characteristic strength [-]
	D_l	Weibull modulus lower bound [-]
	l_l	Lower bound constant for the Weibull modulus [-]
	D_u	Weibull modulus upper bound [-]
	l_u	Upper bound constant for the Weibull modulus [-]
Criterion for fracture	U	Total energy [J·m^{-1}]
	U_M	Mechanical work [J·m^{-1}]
	U_s	Energy necessary to form a new surface [J·m^{-1}]
	γ	Surface energy [J·m^{-1}]
	c	Half of a crack size [m]
	K	Stress intensity factor [MPa·√m]
	Y	Crack geometry factor [-]
	K_{IC}	Fracture toughness [MPa·√m]
Subcritical crack growth	$\dot{\sigma}$	Stress rate [MPa·s^{-1}]
	D	Subcritical crack growth constant [-]
	n	Subcritical crack growth exponent [-]
Creep	$\dot{\varepsilon}$	Creep rate [s^{-1}]
	A	Creep constant [-]
	d	Grain size [µm]
	p	Grain size exponent [-]
	n	Stress exponent [-]

	E_a	Activation energy [kJ·mol^{-1}]
	Ω	Vacancy concentration [m^{-3}]
	D_L	Lattice diffusivity [m²·s^{-1}]
	D_G	Grain boundary diffusivity [m²·s^{-1}]
	δ	Grain boundary width [m]
	φ	Stress intensity factor [-]
Indentation	E_{MIT}, E_{NIT}	Indentation elastic modulus [GPa]
	H_{IT}	Indentation hardness [GPa]
	P	Indentation load [N]
Ring-on-ring	F	Applied load [N]
	s	Displacement [m]
	r_1, r_2	Radius of the loading and supporting ring, respectively [m]
	r_3	Specimen's radius [m]
	E_{RoR}	Elastic modulus obtained by ring-on-ring bending tests [GPa]
Impulse excitation	E_1, E_2	Elastic constants [GPa]
	f_1, f_2	First and second resonant frequencies [Hz]
	K_1, K_2	First and second geometric factors
	D	Diameter [m]
	m	Mass [g]
	υ	Poisson's coefficient [-]
	h	Thickness [m]
	A	Amplitude [dB]
	$\tan\theta$	Loss tangent [-]
	Q^{-1}	Coefficient of internal friction [-]
Pore geometry	L	Pore height [m]
	A_s	Pore wall cross-sectional area [m²]
	χ_p	Pore aspect ratio [-]
	a	Pore wall length [m]
	b	Pore width [m]
	t	Wall thickness [m]
	θ	Pore orientation angle [°]
Mechanical models for fracture behavior on freeze-dried structures	σ_c	Average compressive fracture stress [MPa]
	ρ^*	Relative density [-]
	E_s	Young's modulus [GPa]
	E_{out}	Apparent elastic modulus measured in the out-of-plane direction [GPa]
	E_{in}	Apparent elastic modulus measured in the in-plane direction [GPa]
	σ_{cr}	Compressive strength [MPa]
	q	Correction factor [-]
	k	Buckling geometry constant [-]
	M	Force moment [N·m]
	I	Moment of inertia [m^4]

List of abbreviations

OTM	Oxygen transport membrane
PSA	Pression swing adsorption
STF-X	$SrTi_{1-x}Fe_xO_{3-\delta}$
BSCF	$Ba_{1-x}Sr_xCo_{1-y}Fe_yO_{3-\delta}$
LSCF	$La_{1-x}Sr_xCo_{1-y}Fe_yO_{3-\delta}$
SCG	Subcritical crack growth
SPT	Stress-probability-time diagram
MEK	Methyl-ethyl-ketone
XRD	X-ray diffraction
BET	Brunauer-Emmett-Teller method
ECD	Equivalent circular diameter
SEM	Scanning electron microscope
DFT	Density functional theory
IPF	Inverse pole figure

Appendix A

Table A-1 - Creep parameters for distinct controlling mechanisms [111, 120].

Creep mechanism	***p***	***n***	**Diffusion path**
Dislocation Creep			
Dislocation glide, climb controlled	0	4 – 5	Lattice
Dislocation glide, glide controlled	0	3	Lattice
Dissolution of dislocation loops	0	4	Lattice
Dislocation climb without glide	0	3	Lattice
Dislocation climb by pipe diffusion	0	5	Dislocation core
Diffusional creep			
Nabarro-Herring creep	2	1	Lattice
Coble creep	3	1	Grain boundary
Sliding accommodated by intragranular flow across the grains	1	1	Lattice/Grain boundary
Grain boundary sliding			
With glassy phase at the boundary	3	1	Liquid phase
Without liquid phase	2 – 3		Grain boundary

Appendix B

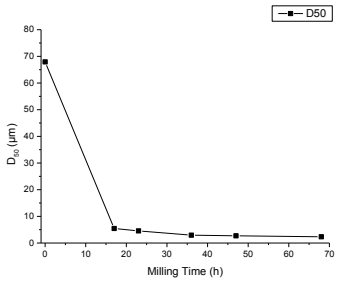

Figure B-1 Average particle size as a function of milling time, STF-25 powder

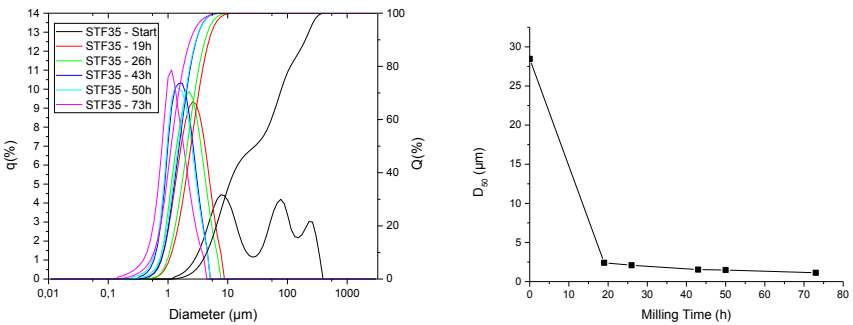

Figure B-2 - Particle size distribution and average grain size in function of milling time for the STF-35 powder

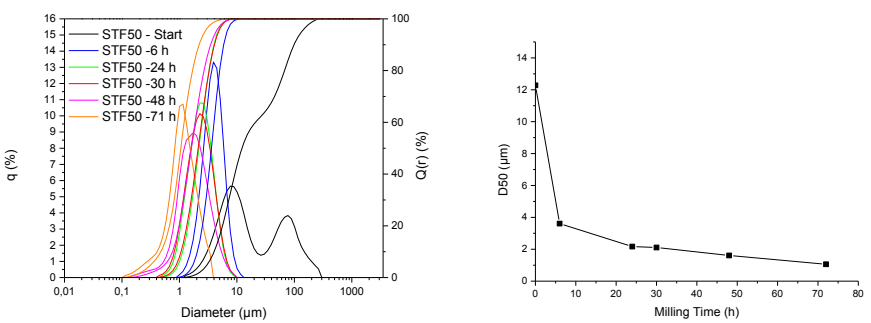

Figure B-3 - Particle size distribution and average grain size in function of milling time for the STF-50 powder

Appendix C

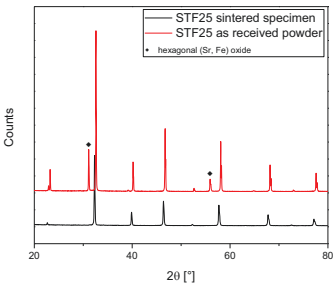

Figure C-1 - XRD pattern comparing the as calcined STF25 powder with a sintered tape cast STF25 specimen.

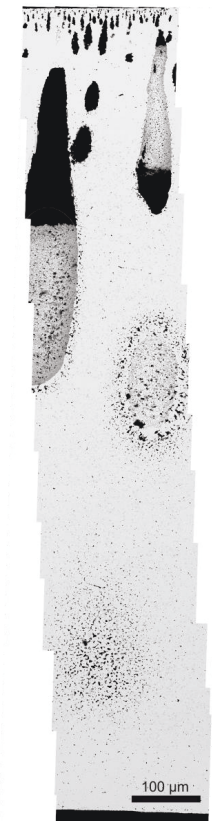

Figure C-2 - SEM panorama of polished cross-section from a phase inversion tape cast STF25 specimen.

Appendix D

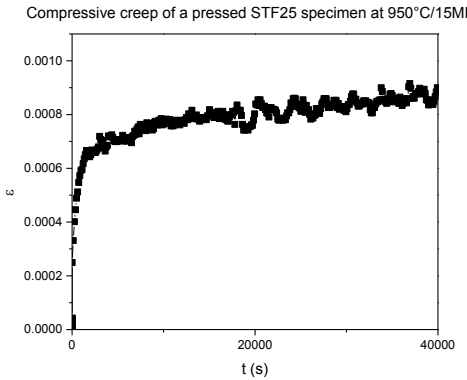

Figure D-1 - Strain as function of time for a pressed STF25 specimen under compressive stress of 15 MPa at 950°C.

Table D-1 -Steady-state creep rate of STF25 specimens as function of temperature and applied stress. Uncertainty derived from linear fitting of the data using OriginPro 2015®.

Specimen	T [°C]	$\dot{\varepsilon}$ [s^{-1}]		
		15 MPa	30 MPa	45 MPa
Pressed	900	$2.5 \pm 0.1 \cdot 10^{-9}$	$7.88 \pm 0.03 \cdot 10^{-9}$	-
	950	$1.0 \pm 0.1 \cdot 10^{-9}$	$2.3 \pm 0.1 \cdot 10^{-8}$	-
	1000	$1.35 \pm 0.01 \cdot 10^{-8}$	$1.2 \pm 0.1 \cdot 10^{-7}$	-
Tape Cast	850	-	$3.76 \pm 0.05 \cdot 10^{-9}$	$1.859 \pm 0.005 \cdot 10^{-8}$
	900	$5.59 \pm 0.03 \cdot 10^{-9}$	$8.16 \pm 0.01 \cdot 10^{-8}$	$1.621 \pm 0.001 \cdot 10^{-7}$
	950	$1.046 \pm 0.006 \cdot 10^{-8}$	$3.305 \pm 0.006 \cdot 10^{-7}$	$8.73 \pm 0.01 \cdot 10^{-7}$
	1000	$2.527 \pm 0.004 \cdot 10^{-7}$	$1.869 \pm 0.001 \cdot 10^{-6}$	$4.076 \pm 0.003 \cdot 10^{-6}$
Freeze dried (in-plane)	800	$3.6 \pm 0.1 \cdot 10^{-9}$	-	-
	900	$8.36 \pm 0.01 \cdot 10^{-8}$	$3.67 \pm 0.01 \cdot 10^{-7}$	-
	950	$5.870 \pm 0.004 \cdot 10^{-7}$	$1.563 \pm 0.002 \cdot 10^{-6}$	-
	1000	$3.532 \pm 0.004 \cdot 10^{-6}$	$7.67 \pm 0.01 \cdot 10^{-6}$	-
Freeze dried (out-of-plane)	900	-	$5.45 \pm 0.01 \cdot 10^{-8}$	-
	950	$4.89 \pm 0.02 \cdot 10^{-8}$	$2.093 \pm 0.003 \cdot 10^{-7}$	-
	1000	$1.864 \pm 0.001 \cdot 10^{-7}$	$0.002 \cdot 10^{-6}$	-

Appendix E

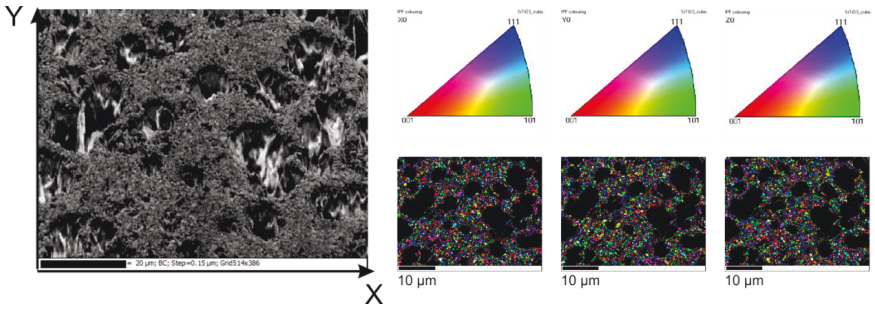

Figure E-1 - EBSD orientation map for the tape cast STF25 specimen after creep test.

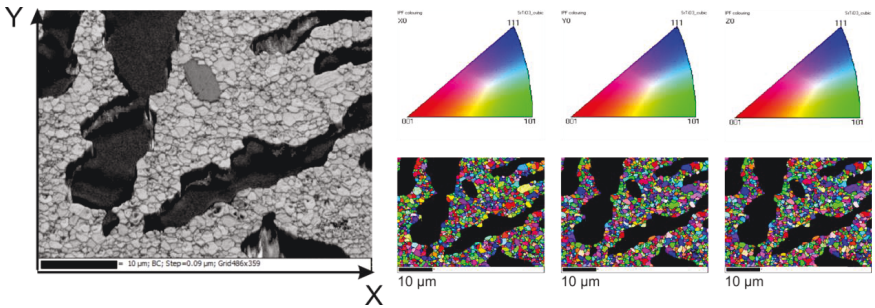

Figure E-2 EBSD orientation map for the freeze dried STF25 specimen (in-plane direction) after creep test.

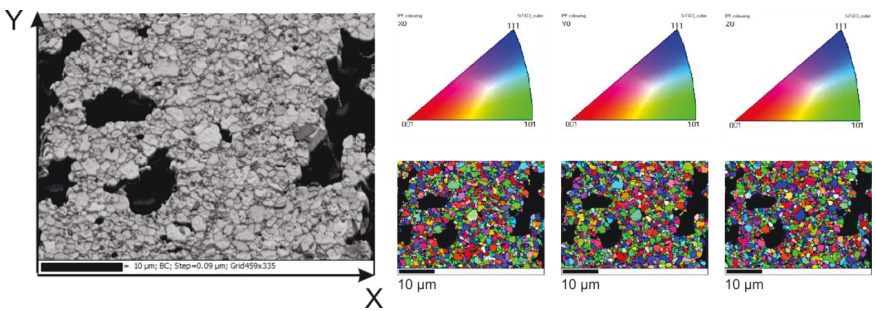

Figure E-3 EBSD orientation map for the freeze-dried STF25 specimen (out-of-plane direction) after creep test.

References

[1] J. Sunarso, S. Baumann, J.M. Serra, W.A. Meulenberg, S. Liu, Y.S. Lin, J.C.D. da Costa, Mixed ionic-electronic conducting (MIEC) ceramic-based membranes for oxygen separation, Journal of Membrane Science 320(1-2) (2008) 13-41.

[2] A.C. Bose, Inorganic Membranes for Energy and Environmental Applications, Springer New York2010.

[3] B.C.H. Steele, Ceramic ion conducting membranes, Current Opinion in Solid State and Materials Science 1(5) (1996) 684-691.

[4] P.N. Dyer, R.E. Richards, S.L. Russek, D.M. Taylor, Ion transport membrane technology for oxygen separation and syngas production, Solid State Ionics 134(1–2) (2000) 21-33.

[5] C.F. Miller, J. Chen, M.F. Carolan, E.P. Foster, Advances in ion transport membrane technology for Syngas production, Catalysis Today 228 (2014) 152-157.

[6] C.S. Chen, S.J. Feng, S. Ran, D.-c. Zhu, W. Liu, H.J.M. Bouwmeester, Conversion of Methane to Syngas by a Membrane-Based Oxidation–Reforming Process, Angewandte Chemie International Edition 42(42) (2003) 5196-5198.

[7] S.G. Jadhav, P.D. Vaidya, B.M. Bhanage, J.B. Joshi, Catalytic carbon dioxide hydrogenation to methanol: A review of recent studies, Chemical Engineering Research and Design 92(11) (2014) 2557-2567.

[8] W. Wang, S. Wang, X. Ma, J. Gong, Recent advances in catalytic hydrogenation of carbon dioxide, Chemical Society Reviews 40(7) (2011) 3703-3727.

[9] B. Hu, C. Guild, S.L. Suib, Thermal, electrochemical, and photochemical conversion of CO2 to fuels and value-added products, Journal of CO2 Utilization 1(Supplement C) (2013) 18-27.

[10] W. Deibert, M.E. Ivanova, S. Baumann, O. Guillon, W.A. Meulenberg, Ion-conducting ceramic membrane reactors for high-temperature applications, Journal of Membrane Science 543(Supplement C) (2017) 79-97.

[11] F. Schulze-Küppers, S.F.P. ten Donkelaar, S. Baumann, P. Prigorodov, Y.J. Sohn, H.J.M. Bouwmeester, W.A. Meulenberg, O. Guillon, Structural and functional properties of $SrTi_{1-x}Fe_xO_{3-d}$ ($0 \leq x \leq 1$) for the use as oxygen transport membrane, Separation and Purification Technology 147 (2015) 414-421.

[12] F. Schulze-Küppers, S. Baumann, W.A. Meulenberg, D. Stöver, H.P. Buchkremer, Manufacturing and performance of advanced supported $Ba_{0.5}Sr_{0.5}Co_{0.8}Fe_{0.2}O_{3-\delta}$ (BSCF) oxygen transport membranes, Journal of Membrane Science 433(0) (2013) 121-125.

[13] B. Cales, J.F. Baumard, Oxygen semipermeability and electronic conductivity in calcia-stabilized zirconia, Journal of Materials Science 17 (1982).

[14] B. Cales, J.F. Baumard, Mixed conduction and defects structure of ZrO_2-Y_2O_3-CeO_2 solid solution, J. Eletrochem. Soc. 131(10) (1984).

[15] P. Maas, N. Nauels, L. Zhao, P. Markewitz, V. Scherer, M. Modigell, D. Stolten, J.F. Hake, Energetic and economic evaluation of membrane-based carbon capture routes for power plant processes, International Journal of Greenhouse Gas Control 44(Supplement C) (2016) 124-139.

[16] K. Aasberg-Petersen, I. Dybkjær, C.V. Ovesen, N.C. Schjødt, J. Sehested, S.G. Thomsen, Natural gas to synthesis gas – Catalysts and catalytic processes, Journal of Natural Gas Science and Engineering 3(2) (2011) 423-459.

[17] C. Karakaya, R.J. Kee, Progress in the direct catalytic conversion of methane to fuels and chemicals, Progress in Energy and Combustion Science 55 (Supplement C) (2016) 60-97.

[18] S.M. Hashim, A.R. Mohamed, S. Bhatia, Current status of ceramic-based membranes for oxygen separation from air, Advances in Colloid and Interface Science 160(1–2) (2010) 88-100.

[19] R. Kriegel, M. Schulz, K. Ritter, L. Kiesel, U. Pippardt, M. Stahn, I. Voigt, Advanced membrane design for oxygen separation, Fraunhofer Institute for Ceramic Technologies and Systems IKTS, Frankfurt am Main, 2011, pp. 114-117.

[20] D.R. Thompson, L.E. Bool, J.C. Chen, OXYGEN ENHANCED COMBUSTION FOR NOx CONTROL, 2004, p. Medium: ED.

[21] H. Wang, Y. Cong, W. Yang, Oxygen permeation study in a tubular $Ba_{0.5}Sr_{0.5}Co_{0.8}Fe_{0.2}O_{3-\delta}$ oxygen permeable membrane, Journal of Membrane Science 210(2) (2002) 259-271.

[22] P. Zeng, R. Ran, Z. Chen, H. Gu, Z. Shao, S. Liu, Novel mixed conducting $SrSc_{0.05}Co_{0.95}O_{3-\delta}$ ceramic membrane for oxygen separation, AIChE Journal 53(12) (2007) 3116-3124.

[23] X. Zhu, H. Wang, W. Yang, Novel cobalt-free oxygen permeable membrane, Chemical Communications (9) (2004) 1130-1131.

[24] J.X. Yi, H.L. Lein, T. Grande, S. Yakovlev, H.J.M. Bouwmeester, High-temperature compressive creep behaviour of the perovskite-type oxide $Ba_{0.5}Sr_{0.5}Co_{0.8}Fe_{0.2}O_{3-\delta}$, Solid State Ionics 180(36) (2009) 1564-1568.

[25] V. Stournari, S.F.P. ten Donkelaar, J. Malzbender, T. Beck, L. Singheiser, H.J.M. Bouwmeester, Creep behavior of perovskite-type oxides $Ba_{0.5}Sr_{0.5}(Co_{0.8}Fe_{0.2})_{1-x}Zr_xO_{3-\delta}$, Journal of the European Ceramic Society 35(6) (2015) 1841-1846.

[26] B. Rutkowski, J. Malzbender, T. Beck, R.W. Steinbrech, L. Singheiser, Creep behaviour of tubular $Ba_{0.5}Sr_{0.5}Co_{0.8}Fe_{0.2}O_{3-\delta}$ gas separation membranes, Journal of the European Ceramic Society 31(4) (2011) 493-499.

[27] S.M. Fang, C.Y. Yoo, H.J.M. Bouwmeester, Performance and stability of niobium-substituted $Ba_{0.5}Sr_{0.5}Co_{0.8}Fe_{0.2}O_{3-\delta}$ membranes, Solid State Ionics 195(1) (2011) 1-6.

[28] M.F. Carolan, P.N. Dyer, K.B. Dyer, M.A. Wilson, T.R. Ohrn, D. Peterson, C.M.-P. Chen, K.G. Rackers, Planar ceramic membrane assembly and oxydation reactor system, US 2008/0085236 A1 2008.

[29] M. Lipińska-Chwałek, G. Pećanac, J. Malzbender, Creep behaviour of membrane and substrate materials for oxygen separation units, Journal of the European Ceramic Society 33(10) (2013) 1841-1848.

[30] C. Gaudillere, J. Garcia-Fayos, J.M. Serra, Enhancing oxygen permeation through hierarchically-structured perovskite membranes elaborated by freeze-casting, Journal of Materials Chemistry A 2(11) (2014) 3828-3833.

[31] O. Ravkina, T. Klande, A. Feldhoff, Investigation of Zr-doped BSCF perovskite membrane for oxygen separation in the intermediate temperature range, Journal of Solid State Chemistry 201 (2013) 101-106.

[32] P. Haworth, S. Smart, J. Glasscock, J.C. Diniz da Costa, High performance yttrium-doped BSCF hollow fibre membranes, Separation and Purification Technology 94 (2012) 16-22.

[33] Y. Zou, F. Schulze-Küppers, J. Malzbender, Creep behavior of porous $La_{0.6}Sr_{0.4}Co_{0.2}Fe_{0.8}O_{3-\delta}$ oxygen transport membrane supports, Ceramics International 41(3, Part A) (2015) 4064-4069.

[34] Z. Shao, W. Yang, Y. Cong, H. Dong, J. Tong, G. Xiong, Investigation of the permeation behavior and stability of a $Ba_{0.5}Sr_{0.5}Co_{0.8}Fe_{0.2}O_{3-\delta}$ oxygen membrane, Journal of Membrane Science 172(1–2) (2000) 177-188.

[35] J.M. Serra, J. Garcia-Fayos, S. Baumann, F. Schulze-Küppers, W.A. Meulenberg, Oxygen permeation through tape-cast asymmetric all-$La_{0.6}Sr_{0.4}Co_{0.2}Fe_{0.8}O_{3-\delta}$ membranes, Journal of Membrane Science 447(0) (2013) 297-305.

[36] P. Niehoff, S. Baumann, F. Schulze-Küppers, R.S. Bradley, I. Shapiro, W.A. Meulenberg, P.J. Withers, R. Vaßen, Oxygen transport through supported $Ba_{0.5}Sr_{0.5}Co_{0.8}Fe_{0.2}O_{3-\delta}$ membranes, Separation and Purification Technology 121 (2014) 60-67.

[37] G. Pećanac, S. Baumann, J. Malzbender, Mechanical properties and lifetime predictions for $Ba_{0.5}Sr_{0.5}Co_{0.8}Fe_{0.2}O_{3-\delta}$ membrane material, Journal of Membrane Science 385–386(0) (2011) 263-268.

[38] S. Baumann, J.M. Serra, M.P. Lobera, S. Escolástico, F. Schulze-Küppers, W.A. Meulenberg, Ultrahigh oxygen permeation flux through supported $Ba_{0.5}Sr_{0.5}Co_{0.8}Fe_{0.2}O_{3-\delta}$ membranes, Journal of Membrane Science 377(1–2) (2011) 198-205.

[39] B.X. Huang, J. Malzbender, R.W. Steinbrech, L. Singheiser, Mechanical properties of $La_{0.58}Sr_{0.4}Co_{0.2}Fe_{0.8}O_{3-\delta}$ membranes, Solid State Ionics 180(2–3) (2009) 241-245.

[40] M. Lipinska-Chwalek, J. Malzbender, A. Chanda, S. Baumann, R.W. Steinbrech, Mechanical characterization of porous $Ba_{0.5}Sr_{0.5}Co_{0.8}Fe_{0.2}O_{3-d}$, Journal of the European Ceramic Society 31(15) (2011) 2997-3002.

[41] J. Malzbender, Mechanical aspects of ceramic membrane materials, Ceramics International 42(7) (2016) 7899-7911.

[42] S.F.P. ten Donkelaar, V. Stournari, J. Malzbender, A. Nijmeijer, H.J.M. Bouwmeester, High-temperature compressive creep behaviour of perovskite-type oxides $SrTi_{1-x}Fe_xO_{3-\delta}$, Journal of the European Ceramic Society 35(15) (2015) 4203-4209.

[43] K. Kwok, H.L. Frandsen, M. Søgaard, P.V. Hendriksen, Mechanical reliability of geometrically imperfect tubular oxygen transport membranes, Journal of Membrane Science 470 (2014) 80-89.

[44] S. Baumann, F. Schulze-Küppers, S. Roitsch, M. Betz, M. Zwick, E.M. Pfaff, W.A. Meulenberg, J. Mayer, D. Stöver, Influence of sintering conditions on microstructure and oxygen permeation of $Ba_{0.5}Sr_{0.5}Co_{0.8}Fe_{0.2}O_{3-\delta}$ (BSCF) oxygen transport membranes, Journal of Membrane Science 359(1–2) (2010) 102-109.

[45] G. Pećanac, S. Foghmoes, M. Lipińska-Chwałek, S. Baumann, T. Beck, J. Malzbender, Strength degradation and failure limits of dense and porous ceramic membrane materials, Journal of the European Ceramic Society 33(13–14) (2013) 2689-2698.

[46] R. Merkle, J. Maier, How Is Oxygen Incorporated into Oxides? A Comprehensive Kinetic Study of a Simple Solid-State Reaction with SrTiO3 as a Model Material, Angewandte Chemie International Edition 47(21) (2008) 3874-3894.

[47] Y. Chiang, D.P. Birnie, W.D. Kingery, Physical Ceramics: Principles for Ceramic Science and Engineering, Second ed., John Wiley & Sons1997.

[48] V.V. Kharton, A.P. Viskup, A.V. Kovalevsky, E.N. Naumovich, F.M.B. Marques, Ionic transport in oxygen-hyperstoichiometric phases with K_2NiF_4-type structure, Solid State Ionics 143(3–4) (2001) 337-353.

[49] V. Kharton, A. Kovalevsky, E. Tsipis, A. Viskup, E. Naumovich, J. Jurado, J. Frade, Mixed conductivity and stability of A-site-deficient Sr (Fe, Ti)$O_{3-\delta}$ perovskites, Journal of Solid State Electrochemistry 7(1) (2002) 30-36.

[50] K. Wiik, S. Aasland, H.L. Hansen, I.L. Tangen, R. Ødegård, Oxygen permeation in the system $SrFeO_{3-x}$–$SrCoO_{3-y}$, Solid State Ionics 152–153 (2002) 675-680.

[51] H.J.M. Bouwmeester, A.J. Burggraaf, Chapter 10 Dense ceramic membranes for oxygen separation, in: A.J. Burggraaf, L. Cot (Eds.), Membrane Science and Technology, Elsevier1996, pp. 435-528.

[52] P. Prigorodov, $SrTi_{1-x}Fe_xO_{3-d}$ als Membranwerkstoff zur Sauerstoffbereitstellung - Herstellung und Charakterisierung, Institut für Gesteinhüttenkunde, RWTH-Achen, Aachen, 2013.

[53] M. James, D. Cassidy, K.F. Wilson, J. Horvat, R.L. Withers, Oxygen vacancy ordering and magnetism in the rare earth stabilised perovskite form of "$SrCoO_{3-\delta}$", Solid State Sciences 6(7) (2004) 655-662.

[54] P. Zeng, R. Ran, Z. Chen, W. Zhou, H. Gu, Z. Shao, S. Liu, Efficient stabilization of cubic perovskite $SrCoO_{3-\delta}$ by B-site low concentration scandium doping combined with sol–gel synthesis, Journal of Alloys and Compounds 455(1) (2008) 465-470.

[55] J.E. ten Elshof, H.J.M. Bouwmeester, H. Verweij, Oxygen transport through $La_{1-x}Sr_xFeO_{3-\delta}$ membranes. I. Permeation in air/He gradients, Solid State Ionics 81(1) (1995) 97-109.

[56] Y. Zou, W. Araki, M. Balaguer, J. Malzbender, Elastic properties of freeze-cast $La_{0.6}Sr_{0.4}Co_{0.2}Fe_{0.8}O_{3-\delta}$, Journal of the European Ceramic Society 36(7) (2016) 1651-1657.

[57] S. Diethelm, J. Van herle, Oxygen transport through dense $La_{0.6}Sr_{0.4}Fe_{0.8}Co_{0.2}O_{3-\delta}$ perovskite-type permeation membranes, Journal of the European Ceramic Society 24(6) (2004) 1319-1323.

[58] J.F. Vente, S. McIntosh, W.G. Haije, H.J.M. Bouwmeester, Properties and performance of $Ba_xSr_{1-x}Co_{0.8}Fe_{0.2}O_{3-\delta}$ materials for oxygen transport membranes, Journal of Solid State Electrochemistry 10(8) (2006) 581.

[59] H.J.M. Bouwmeester, A.J. Burggraaf, Dense Ceramic Membranes for Oxygen Separation, Handbook of Solid State Electrochemistry1997.

[60] S. Baumann, W.A. Meulenberg, H.P. Buchkremer, Manufacturing strategies for asymmetric ceramic membranes for efficient separation of oxygen from air, Journal of the European Ceramic Society 33(7) (2013) 1251-1261.

[61] S. Molin, W. Lewandowska-Iwaniak, B. Kusz, M. Gazda, P. Jasinski, Structural and electrical properties of Sr(Ti, Fe)$O_{3-\delta}$ materials for SOFC cathodes, Journal of Electroceramics 28(1) (2012) 80-87.

[62] W. Jung, H.L. Tuller, Impedance study of SrTi1−xFexO3−δ (x=0.05 to 0.80) mixed ionic-electronic conducting model cathode, Solid State Ionics 180(11) (2009) 843-847.

[63] A. Rothschild, W. Menesklou, H.L. Tuller, E. Ivers-Tiffée, Electronic Structure, Defect Chemistry, and Transport Properties of $SrTi_{1-x}Fe_xO_{3-y}$ Solid Solutions, Chemistry of Materials 18(16) (2006) 3651-3659.

[64] V.V. Kharton, A.V. Kovalevsky, A.P. Viskup, J.R. Jurado, F.M. Figueiredo, E.N. Naumovich, J.R. Frade, Transport Properties and Thermal Expansion of $Sr_{0.97}Ti_{1-x}Fe_xO_{3-\delta}$ (x=0.2–0.8), Journal of Solid State Chemistry 156(2) (2001) 437-444.

[65] Y. Takeda, K. Kanno, T. Takada, O. Yamamoto, M. Takano, N. Nakayama, Y. Bando, Phase relation in the oxygen nonstoichiometric system, $SrFeO_x$ ($2.5 \leq x \leq 3.0$), Journal of Solid State Chemistry 63(2) (1986) 237-249.

[66] L.A. Dunyushkina, E.A. Mashkina, I.Y. Nechaev, A.A. Babkina, N.O. Esina, B.V. Zhuravlev, A.K. Demin, Influence of acceptor doping on ionic conductivity in alkali earth titanate perovskites, Ionics 8(3) (2002) 293-299.

[67] J. Mizusaki, M. Okayasu, S. Yamauchi, K. Fueki, Nonstoichiometry and phase relationship of the $SrFeO_{2.5}SrFeO_3$ system at high temperature, Journal of Solid State Chemistry 99(1) (1992) 166-172.

[68] A. Rothschild, S.J. Litzelman, H.L. Tuller, W. Menesklou, T. Schneider, E. Ivers-Tiffée, Temperature-independent resistive oxygen sensors based on $SrTi_{1-x}Fe_xO_{3-\delta}$ solid solutions, Sensors and Actuators B: Chemical 108(1) (2005) 223-230.

[69] S. Steinsvik, R. Bugge, J.O.N. GjØNnes, J. TaftØ, T. Norby, The Defect Structure of $SrTi_{1-x}Fe_xO_{3-y}$ (x = 0–0.8) Investigated by Electrical Conductivity Measurements and Electron Energy Loss Spectrocospy (EELS), Journal of Physics and Chemistry of Solids 58(6) (1997) 969-976.

[70] S. Steinsvik, T. Norby, P. Kofstad, Electrical conductivity and defect structure in the system SrTi1−xFexO3−y (x=0.1–0.8), Augustinus Buchhandlung, Aachen, Germany, 1995.

[71] R.E. Mistler, E.R. Twiname, Tape Casting: Theory and Practice, Wiley2000.

[72] A.L. da Silva, A.M. Bernardin, D. Hotza, Forming of thin porcelain tiles: A comparison between tape casting and dry pressing, Ceramics International 40(2) (2014) 3761-3767.

[73] M. Yu, J. Zhang, X. Li, H. Liang, H. Zhong, Y. Li, Y. Duan, D.L. Jiang, X. Liu, Z. Huang, Optimization of the tape casting process for development of high performance alumina ceramics, Ceramics International 41(10, Part B) (2015) 14845-14853.

[74] S. Deville, Freeze-Casting of Porous Ceramics: A Review of Current Achievements and Issues, Advanced Engineering Materials 10(3) (2008) 155-169.

[75] S. Deville, Ice-templating, freeze casting: Beyond materials processing, Journal of Materials Research 28(17) (2013) 2202-2219.

[76] S. Deville, E. Saiz, A.P. Tomsia, Ice-templated porous alumina structures, Acta Materialia 55(6) (2007) 1965-1974.

[77] S. Deville, E. Saiz, A.P. Tomsia, Freeze casting of hydroxyapatite scaffolds for bone tissue engineering, Biomaterials 27(32) (2006) 5480-5489.

[78] W. He, H. Huang, J.-f. Gao, L. Winnubst, C.-s. Chen, Phase-inversion tape casting and oxygen permeation properties of supported ceramic membranes, Journal of Membrane Science 452 (2014) 294-299.

[79] C.A. Smolders, A.J. Reuvers, R.M. Boom, I.M. Wienk, Microstructures in phase-inversion membranes. Part 1. Formation of macrovoids, Journal of Membrane Science 73(2) (1992) 259-275.

[80] H. Fang, C. Ren, Y. Liu, D. Lu, L. Winnubst, C. Chen, Phase-inversion tape casting and synchrotron-radiation computed tomography analysis of porous alumina, Journal of the European Ceramic Society 33(10) (2013) 2049-2051.

[81] T. Liu, Y. Wang, Y. Zhang, S. Fang, L. Lei, C. Ren, F. Chen, Steam electrolysis in a solid oxide electrolysis cell fabricated by the phase-inversion tape casting method, Electrochemistry Communications 61(Supplement C) (2015) 106-109.

[82] W. He, H. Huang, J.-f. Gao, L. Winnubst, C.-s. Chen, Phase-inversion tape casting and oxygen permeation properties of supported ceramic membranes, Journal of Membrane Science 452(0) (2014) 294-299.

[83] W.D. Kingery, H.K. Bowen, D.R. Uhlmann, Introduction to ceramics, Wiley1976.

[84] J.K. Mackenzie, The Elastic Constants of a Solid containing Spherical Holes, Proceedings of the Physical Society. Section B 63(1) (1950) 2.

[85] R.M. Spriggs, Expression for Effect of Porosity on Elastic Modulus of Polycrystaline Refractory Materials, Particurlarly Aluminium Oxide, Journal of the American Ceramic Society 44(12) (1961) 628-629.

[86] R.W. Rice, Extension of Exponential Porosity Depence of Strength and Elastic-Moduli, Journal of the American Ceramic Society 59(11-1) (1976) 536-537.

[87] J.C. Wang, Young Modulus of Porous Materials. 1: Theoretical Derivation of Modulus Porosity Correlation, Journal of Materials Science 19(3) (1984) 801-808.

[88] K.K. Phani, S.K. Niyogi, A.K. Maitra, M. Roychaudhury, Strength and Elastic-Modulus of a Porous Brittle Solid - an Acoustoultrasonic Study, Journal of Materials Science 21(12) (1986) 4335-4341.

[89] K.K. Phani, S.K. Niyogi, Young Modulus of Porous Brittle Solids, Journal of Materials Science 22(1) (1987) 257-263.

[90] A.R. Boccaccini, Z. Fan, A new approach for the Young's modulus-porosity correlation of ceramic materials, Ceramics International 23(3) (1997) 239-245.

[91] B.X. Huang, V. Vasechko, Q.L. Ma, J. Malzbender, Thermo-mechanical properties of $(Sr,Y)TiO_3$ as anode material for solid oxide fuel cells, Journal of Power Sources 206 (2012) 204-209.

[92] J. Wachtman, D. Lam, Young's modulus of various refractory materials as a function of temperature, Journal of the American Ceramic Society 42(5) (1959) 254-260.

[93] J.B. Wachtman, W.E. Tefft, D.G. Lam, C.S. Apstein, Exponential Temperature Dependence of Young's Modulus for Several Oxides, Physical review 122(6) (1961) 1754-1759.

[94] B.X. Huang, J. Malzbender, R.W. Steinbrech, E. Wessel, H.J. Penkalla, L. Singheiser, Mechanical aspects of ferro-elastic behavior and phase composition of $La_{0.58}Sr_{0.4}Co_{0.2}Fe_{0.8}O_{3-\delta}$, Journal of Membrane Science 349(1–2) (2010) 183-188.

[95] H.L. Lein, Ø.S. Andersen, P.E. Vullum, E. Lara-Curzio, R. Holmestad, M.-A. Einarsrud, T. Grande, Mechanical properties of mixed conducting $La_{0.5}Sr_{0.5}Fe_{1-x}Co_xO_{3-\delta}$ ($0 \leq x \leq 1$) materials, Journal of Solid State Electrochemistry 10(8) (2006) 635-642.

[96] B.X. Huang, Thermomecanical properties of mixed ion-electron conducting membrane materials, RWTH Aachen University, Aachen, 2010.

[97] O. Bernard, M. Andrieux, S. Poissonnet, A.M. Huntz, Mechanical behaviour of ferroelectric films on perovskite substrate, Journal of the European Ceramic Society 24(5) (2004) 763-773.

[98] V.K. Stournari, Thermo-mechanical Properties of Mixed Ionic-Electronic Conducting Membranes for Energy Applications, Falkutät für Maschinenwesen, Rheinisch-Westfälische Technische Horschule Aachen, Jülich, 2015.

[99] H. Rached, D. Rached, M. Rabah, R. Khenata, A.H. Reshak, Full-potential calculation of the structural, elastic, electronic and magnetic properties of $XFeO_3$ (X=Sr and Ba) perovskite, Physica B: Condensed Matter 405(17) (2010) 3515-3519.

[100] J.D. Ferry, Viscoelastic properties of polymers, Third ed., John Wiley & Sons1980.

[101] R. Lakes, Viscoelasticity Notes. http://silver.neep.wisc.edu/~lakes/VEnotes.html. (Accessed June 6th 2017).

[102] M. Matsuzawa, S. Horibe, J. Sakai, Anelasticity and strength in zirconia ceramics, Key Engineering Materials 280-283(II) (2005) 967-972.

[103] R.J. Harrison, S.A.T. Redfern, E.K.H. Salje, Dynamical excitation and anelastic relaxation of ferroelastic domain walls in $LaAlO_3$, Physical Review B 69(14) (2004) 144101.

[104] W. Schranz, Superelastic softening in perovskites, Physical Review B 83(9) (2011) 094120.

[105] F. Cordero, A. Franco, V.R. Calderone, P. Nanni, V. Buscaglia, Anelastic spectroscopy for studying O vacancies in perovskites, Journal of the European Ceramic Society 26(14) (2006) 2923-2929.

[106] D. Brunner, S. Taeri-Baghbadrani, W. Sigle, M. Rühle, Surprising Results of a Study on the Plasticity in Strontium Titanate, Journal of the American Ceramic Society 84(5) (2001) 1161-1163.

[107] A.A. Griffith, The phenomena of rupture and flow in solids, Philosophical transactions of the royal society of london. Series A, containing papers of a mathematical or physical character 221 (1921) 163-198.

[108] W. Weibull, A Statistical Distribution Function of Wide Applicability, Journal of Applied Mechanics 103 (1951) 33.

[109] DIN EN 843-5 Hochleistungskeramik - Mechanische Eigenschaften monolitischer Keramik bei Raumtemperatur, Teil 5: Statistische Auswertung, DIN Deutsches Institut für Normung e.V., 2007.

[110] B.X. Huang, J. Malzbender, R.W. Steinbrech, L. Singheiser, Discussion of the complex thermo-mechanical behavior of $Ba_{0.5}Sr_{0.5}Co_{0.8}Fe_{0.2}O_{3-\delta}$, Journal of Membrane Science 359(1–2) (2010) 80-85.

[111] D.J. Green, An Introduction to the Mechanical Properties of Ceramics, Cambridge University Press1998.

[112] B. Rutkowski, Mechanical properties and microstructure of dense ceramic membranes for oxygen separation in zero-emission power plant, RWTH Aachen University, 2012.

[113] K.-H. Yang, N.-J. Ho, H.-Y. Lu, Deformation Microstructure in (001) Single Crystal Strontium Titanate by Vickers Indentation, Journal of the American Ceramic Society 92(10) (2009) 2345-2353.

[114] S.R. Choi, J.A. Salem, F.A. Holland, Estimation of Slow Crack Growth Parameters for Constant Stress-Rate Test Data of Advanced Ceramics and Glass by the Individual Data and Arithmetic Mean Methods, NASA Technical Memorandum 107369, 1997.

[115] M.W. Barsoum, Fundamentals of Ceramics, McGraw Hill1997.

[116] G. Pećanac, S. Baumann, J. Malzbender, Mechanical properties and lifetime predictions for $Ba_{0.5}Sr_{0.5}Co_{0.8}Fe_{0.2}O_{3-\delta}$ membrane material, Journal of Membrane Science 385–386 (2011) 263-268.

[117] N. Nagabhushana, T. Nithyanantham, S. Bandopadhyay, J. Zhang, Subcritical Crack Growth Behavior of A Perovskite-Type Oxygen Transport Ceramic Membrane, International Journal of Applied Ceramic Technology 8(2) (2011) 390-397.

[118] B.X. Huang, R.W. Steinbrech, S. Baumann, J. Malzbender, Creep behavior and its correlation with defect chemistry of $La_{0.58}Sr_{0.4}Co_{0.2}Fe_{0.8}O_{3-\delta}$, Acta Materialia 60(6–7) (2012) 2479-2484.

[119] G. Pećanac, L. Kiesel, J. Malzbender, Steady-state creep of porous and an extended analysis on the creep of dense BSCFZ perovskite, Journal of Membrane Science 456 (2014) 134-138.

[120] W. Roger Cannon, T.G. Langdon, Creep of ceramics, Journal of Materials Science 18(1) (1983) 1-50.

[121] A.H. Chokshi, Diffusion creep in oxide ceramics, Journal of the European Ceramic Society 22(14–15) (2002) 2469-2478.

[122] F.R.N. Nabarro, Report of a Conference on the Strength of Solids Physical Society, London, 1948, pp. 75-90.

[123] C. Herring, Diffusional Viscosity of a Polycrystalline Solid, Journal of Applied Physics 21(5) (1950) 437-445.

[124] R.L. Coble, A Model for Boundary Diffusion Controlled Creep in Polycrystalline Materials, Journal of Applied Physics 34(6) (1963) 1679-1682.

[125] Y.s. Na, J.-H. Lee, Interpretation of viscous deformation of Zr-based bulk metallic glass alloys based on Nabarro-Herring creep model, 2006.

[126] A.P. Hynes, R. Doremus, Theories of Creep in Ceramics, 1996.

[127] D.R. Thompson, L.E. Bool, J.C. Chen, Oxygen enhanced combustion for NOx control, Praxair Inc, 2004.

[128] K. Kleveland, A. Wereszczak, T.P. Kirkland, M.A. Einarsrud, T. Grande, Compressive creep performance of $SrFeO_3$, Journal of the American Ceramic Society 84(8) (2001) 1822-1826.

[129] P.T. Bretheau, J. Castaing, J. Rabier, P. Veyssière, Mouvement des dislocations et plasticité à haute température des oxydes binaires et ternaires, Advances in Physics 28(6) (1979) 835-1014.

[130] J.X. Yi, H.L. Lein, T. Grande, S. Yakovlev, H.J.M. Bouwmeester, High-temperature compressive creep behaviour of the perovskite-type oxide $Ba_{0.5}Sr_{0.5}Co_{0.8}Fe_{0.2}O_{3-\delta}$, Solid State Ionics 180(36–39) (2009) 1564-1568.

[131] P.P. Ewald, 50 Years of X-ray Diffraction, N.V.A. Oosthoek's Uitgeversmaatschappij, Utrecht, the Netherlands, 1962.

[132] G. Eshel, G.J. Levy, U. Mingelgrin, M.J. Singer, Critical Evaluation of the Use of Laser Diffraction for Particle-Size Distribution Analysis, Soil Science Society of America Journal 68(3) (2004) 736-743.

[133] S. Lowell, J.E. Shields, Powder surface area and porosity, Springer Science & Business Media2013.

[134] V. Vasechko, Thermo-Mechanical Investigations of Reoxidation-Stable Material Concepts for Solid Oxide Fuel Cells, Fakultät für Maschinenwesen, RWTH Aachen University, 2014.

[135] ISO 14250:2000 Steel - Metallographic characterization of duplex grain size and distributions, 2000.

[136] W.C. Oliver, G.M. Pharr, An improved technique for determining hardness and elastic modulus using load and displacement sensing indentation experiments, Journal of Materials Research 7(06) (1992) 1564-1583.

[137] J. Gubicza, A. Juhasz, J. Lendvai, A new method for hardness determination from depth sensing indentation tests, Journal of materials research 11(12) (1996) 2964-2967.

[138] J.F. Nonemacher, H. Zheng, M. Finsterbusch, J. Malzbender, M. Krüger, Microstructure and properties investigation of garnet structured $Li_7La_3Zr_{12}O_{12}$ for solid state batteries, Unpublished manuscript (2017).

[139] G.R. Anstis, P. Chantikul, B.R. Lawn, D.B. Marshall, A Critical Evaluation of Indentation Techniques for Measuring Fracture Toughness: I, Direct Crack Measurements, Journal of the American Ceramic Society 64(9) (1981) 533-538.

[140] G.D. Quinn, R.C. Bradt, On the Vickers Indentation Fracture Toughness Test, Journal of the American Ceramic Society 90(3) (2007) 673-680.

[141] ASTM C1499-05: Standard Test Method for Monotonic Equibiaxial Flexural Strength of Advanced Ceramics at Ambient Temperature, ASTM International, West Conshohocken, PA, 2005.

[142] ASTM C1239-07: Standard Practice for Reporting Uniaxial Strength Data and Estimating Weibull Distribution Parameters for Advanced Ceramics, ASTM International, West Conshohocken, PA, 2007.

[143] G.J. Hahn, S.S. Shapiro, Statistical models in engineering John Wiley & Sons, New York, 1967.

[144] ASTM, ASTM E 1876-01 Standard test method for dynamic Young's modulus, shear modulus, and Poisson's ratio by impulse excitation of vibration, 2005.

[145] W. Araki, J. Malzbender, Ferroelastic deformation of $La_{0.58}Sr_{0.4}Co_{0.2}Fe_{0.8}O_{3-\delta}$ under uniaxial compressive loading, Journal of the European Ceramic Society 33(4) (2013) 805-812.

[146] W. Araki, Y. Arai, J. Malzbender, Transitions of $Ba_{0.5}Sr_{0.5}Co_{0.8}Fe_{0.2}O_{3-\delta}$ and $La_{0.58}Sr_{0.4}Co_{0.2}Fe_{0.8}O_{3-\delta}$, Materials Letters 132 (2014) 295-297.

[147] Y. Zou, F. Schulze-Küppers, M. Balaguer, J. Malzbender, M. Krüger, Creep behavior of porous La0.6Sr0.4Co0.2Fe0.8O3-δ substrate material for oxygen separation application, Journal of the European Ceramic Society.

[148] K. Niihara, R. Morena, D.P.H. Hasselman, Evaluation ofK Ic of brittle solids by the indentation method with low crack-to-indent ratios, J Mater Sci Lett 1(1) (1982) 13-16.

[149] A. Lichtner, D. Roussel, D. Jauffrès, C.L. Martin, R.K. Bordia, Effect of Macropore Anisotropy on the Mechanical Response of Hierarchically Porous Ceramics, Journal of the American Ceramic Society 99(3) (2016) 979-987.

[150] J. Sauter, Die Grössenbestimmung der im Gemischnebel von Verbrennungskraftmaschinen vorhandenen Brennstoffteilchen, VDI-Verlag1926.

[151] C.B. Ponton, R.D. Rawlings, Vickers indentation fracture toughness test: Part 1 - Review of literature and formulation of standardised indentation toughness equations, Materials Science and Technology 5(9) (1989) 865-872.

[152] R. Bermejo, P. Supancic, C. Krautgasser, R. Morrell, R. Danzer, Subcritical crack growth in Low Temperature Co-fired Ceramics under biaxial loading, Engineering Fracture Mechanics 100(Supplement C) (2013) 108-121.

[153] H.-J. Kim, Y.-G. Kweon, Elastic modulus of plasma-sprayed coatings determined by indentation and bend tests, Thin Solid Films 342(1) (1999) 201-206.

[154] V. Vasechko, B. Huang, Q. Ma, F. Tietz, J. Malzbender, Thermomechanical properties of Y-substituted $SrTiO_3$ used as re-oxidation stable anode substrate material, Journal of the European Ceramic Society 34(15) (2014) 3749-3754.

[155] F. Cordero, A. Franco, V. Calderone, P. Nanni, V. Buscaglia, Anelastic spectroscopy for studying O vacancies in perovskites, 2006.

[156] M.F. Ashby, R.F.M. Medalist, The mechanical properties of cellular solids, Metallurgical Transactions A 14(9) (1983) 1755-1769.

[157] L.J. Gibson, M.F. Ashby, Cellular Solids: Structure and Properties, Cambridge University Press1999.

[158] A. Ojuva, M. Järveläinen, M. Bauer, L. Keskinen, M. Valkonen, F. Akhtar, E. Levänen, L. Bergström, Mechanical performance and CO_2 uptake of ion-exchanged zeolite A structured by freeze-casting, Journal of the European Ceramic Society 35(9) (2015) 2607-2618.

[159] T. Keuter, D. Roehrens, N.H. Menzler, R. Vaßen, Redox-Stable High-Performance Thin-Film Solid Oxide Fuel Cell, ECS Transactions 68(1) (2015) 2001-2009.

[160] M.M. Porter, R. Imperio, M. Wen, M.A. Meyers, J. McKittrick, Bioinspired Scaffolds with Varying Pore Architectures and Mechanical Properties, Advanced Functional Materials 24(14) (2014) 1978-1987.

[161] F.P. Beer, E.R. Johnston, J.T. DeWolf, Mechanics of Materials, McGraw-Hill, New York, 2002.

[162] A.E. Haas, T. Verschoyle, Introduction to theoretical physics, Constable & company ltd.1928.

[163] E.W. Andrews, L.J. Gibson, M.F. Ashby, The creep of cellular solids, Acta Materialia 47(10) (1999) 2853-2863.

[164] E.W. Andrews, J.S. Huang, L.J. Gibson, Creep behavior of a closed-cell aluminum foam, Acta Materialia 47(10) (1999) 2927-2935.

[165] J. Langer, M.J. Hoffmann, O. Guillon, Direct comparison between hot pressing and electric field-assisted sintering of submicron alumina, Acta Materialia 57(18) (2009) 5454-5465.

[166] J.M. Montes, F.G. Cuevas, J. Cintas, A new expression for the effective pressure on powders under compression, Computational Materials Science 36(3) (2006) 329-337.

[167] A.S. Helle, K.E. Easterling, M.F. Ashby, Hot-isostatic pressing diagrams: New developments, Acta Metallurgica 33(12) (1985) 2163-2174.

[168] K. Kwok, D. Boccaccini, Å.H. Persson, H.L. Frandsen, Homogenization of steady-state creep of porous metals using three-dimensional microstructural reconstructions, International Journal of Solids and Structures 78 (2016) 38-46.

[169] Z. Wang, S.-i. Karato, K. Fujino, High temperature creep of single crystal strontium titanate ($SrTiO_3$): a contribution to creep systematics in perovskites, Physics of the Earth and Planetary Interiors 79(3) (1993) 299-312.

[170] D. Singh, M. Lorenzo-Martín, G. Chen, F. Gutiérrez-Mora, J.L. Routbort, High-temperature deformation behavior in $SrTiO_3$ ceramics, Journal of the European Ceramic Society 27(11) (2007) 3377-3384.

Index of Figures

Index of Tables

Acknowledgments

This work was accomplished in the Institute of Energy and Climate Research, Materials Synthesis and Processing (IEK-1) and Microstructure and Properties (IEK-2), at the Forschungszentrum Jülich GmbH between March 2015 and February 2018.

Hereby I want to express my gratitude to the people, without whom this thesis would not be possible.

At first, I would like to thank my father, my mother, and my brother. Their love, support, and encouragement strengthened me throughout these three years.

I would also like to thank my supervisor and head of IEK-1 Univ.-Prof. Dr.-Ing. O. Guillon for his orientation and advising and the head of IEK-2 Univ.-Prof. Dr.-Ing. L. Singheiser for providing the infrastructure and the necessary conditions to realize this PhD work. Special thanks are also given to members of my committee Univ.-Prof. Dr. M. Krüger und Univ.-Prof. Dr. rer. nat. R. Telle.

I gratefully acknowledge my scientific advisors Dr. J. Malzbender, Dr. F. Schulze-Küppers, and Dr. S. Baumann for their valuable support during these three years. The friendly scientific discussions followed by their incentive were really appreciated.

Gratitude is also expressed to Dr. E. Wessel, Dr. D. Grüner, and Dr. D. Seebold for their cooperation with the structural characterization, as well as to Mr. M. Zigner and Dr. Y. J. Sohn for their help with phase analysis, to Ms. D. Liebert for her assistance with the mechanical tests, and to Mr. S. Heinz and Mr. M. Kappertz for his help with samples preparation. I would like to thank specially Ms. T. Osipova not only for her aid in the mechanical characterization, but also for her friendship and guidance during my PhD work.

The colleagues and friends from Forschungszentrum Jülich were essential and collaborated immensely to my personal and professional growth in life. These outstanding people motivated my scientific work and inspired me to always carry on. My kindly thanks are given to my colleagues and friends for the priceless help and productive discussions: Dr. V. Stournari, Dr. G. Pećanac, Dr. A. Böhm, Dr. J. Wei, Dr. Y. Zou, Dr. S. Stille, S. von Helden, Dr. M. F. Hasanabi, Dr. V. Ebrahimzade, G. Yan, F. Zheng, U. Unije, J. G. Pereira da Silva, Y. Liu, J. Brendt, U. Gude, and K. Mielke.

I would like to thank three esteemed friends that faithfully supported and motivated me during my PhD: J. Nonemacher, F. Martins, and Dr. Z. Wu.

At last, the financial support by Conselho Nacional de Desenvolvimento Científico e Tecnológico (CNPq) and Deutscher Akademischer Austauschdienst (DAAD) are kindly acknowledged.

Abstract

Pure oxygen is considered to be an important commodity and its demand is expected to rise in the upcoming years. Therefore, interest in a new, scalable technology for air separation based on oxygen transport membranes has increased. Indeed, ceramic oxygen transport membranes can possess remarkable advantages compared to existing state-of-the-art processes for oxygen production in small and medium scale. Typically, such membranes have to be operated at 800 - 900 °C and under high pressure gradients, which challenges significantly the chemical and mechanical stability of the respective brittle ceramics components.

Thus, the current work concentrates on the mechanical properties of a promising perovskite material for mixed conducting oxygen transport membranes based on $SrTi_{1-x}Fe_xO_{3-\delta}$, (STF-X) with x = 0.25, 0.35 and 0.5. The dense membrane materials, synthesized through solid state reaction route and processed via tape casting, were characterized with respect to their mechanical behavior via depth-sensitive indentation testing and ring-on-ring flexural tests. No tradeoff between functional and mechanical properties is observed for the studied dense materials. Ring-on-ring tests conducted at different loading rates gave access to subcritical crack growth sensitivity and aided the prediction of the materials' lifetime through stress-time-probability diagrams, where $SrTi_{0.65}Fe_{0.35}O_3$ revealed the best performance among the studied compositions.

The mechanical properties of dense tape cast $SrTi_{0.75}Fe_{0.25}O_{3-\delta}$ were derived at 900°C with help of ring-on-ring flexural tests carried out at two distinct loading rates: 1 and 100 N/min. The apparent elastic modulus appeared to be time dependent. The average fracture stress estimated on the basis of the data was rather loading rate invariant and higher than the same property obtained at room temperature. Thus, it appears that $SrTi_{0.75}Fe_{0.25}O_{3-\delta}$ possesses an anelastic behavior that might be associated with oxygen release and/or primary creep deformation.

In addition, porous $SrTi_{0.75}Fe_{0.25}O_{3-\delta}$ specimens, representative for use as porous substrate for supported asymmetric oxygen transport membranes, were produced through tape casting, freeze drying, and phase inversion casting. The first method yielded a random distributed porosity with spherical pores reaching a value of 32%. Freeze-drying and phase inversion, however, derived a channel-like porosity in the same level. Ring-on-ring bending tests were employed in order to derive elasticity and fracture stresses of the manufactured samples. In order

to investigate the effect of anisotropy of the mechanical properties for freeze-dried specimens, compressive testing was used yielding apparent elastic modulus and fracture stresses in the transverse (out-of-plane) and longitudinal (in-plane) direction, verifying a strong dependency onto pore orientation. The lower mechanical stability in the in-plane direction appears to be associated with bending mode of the pore walls, being a result of a lower resistance to crack initiation. Acoustic emissions recorded during compressive tests indicated continuous damage of the pore walls before complete failure of the specimen, which could also be confirmed by complementary in-situ compressive tests in a scanning electronic microscope. Also, creep behavior of pressed, tape cast, and freeze-dried $SrTi_{0.75}Fe_{0.25}O_{3-\delta}$ specimens was investigated and the experimental creep parameters were obtained. The results derived a stress exponent in the range of 2 with a large primary creep deformation (in the range of 0.03 to 0.6%). Therefore, it is suggested that $SrTi_{0.75}Fe_{0.25}O_{3-\delta}$ undergoes a combination of diffusive and dislocation creep.

Kurzfassung

Reiner Sauerstoff ist ein wichtiger Rohstoff. Es wird erwartet dass der Bedarf in folgenden Jahren zunimmt. Deswegen ist das Interesse an einer neuen und skalierbaren Technologie für Lufttrennung auf Basis von Sauerstoff-Permeationsmembranen angestiegen. Tatsächlich können Sauerstoff-Permeationsmembranen bemerkenswerte Vorteile im Vergleich zu existierenden Prozessen auf dem neuesten Stand für Sauerstoffproduktion in kleiner oder mittlerer Skala darstellen. Typischerweise werden diese Membrane bei 800 – 900°C und hohen Druckgradienten betrieben, so dass hohe chemische und mechanische Stabilität grundlegende Anforderungen an die jeweiligen spröden keramischen Komponenten sind.

Deshalb fokussiert die vorliegende Arbeit auf die mechanischen Eigenschaften eines vielversprechenden Werkstoffes für mischleitende Sauerstoff-Permeationsmembranen auf Basis von $SrTi_{1-x}Fe_xO_{3-\delta}$, (STF-X), mit x = 0,25, 0,35 und 0,5. Die durch Festkörperreaktion synthetisierten und durch Foliengießen hergestellte dichten Materialien wurden bezüglich der mechanischen Stabilität mit einem instrumentierten tiefen-sensitiven Härtemessverfahren und Doppelring-Biegungstest charakterisiert. Eine etwaige negative Wechselwirkung zwischen funktionellen und mechanischen Eigenschaften wurde für die untersuchten dichten Materialien nicht beobachtet. Die aufgrund von Doppelringtests bei unterschiedlichen Belastungsraten ermittelte Empfindlichkeit hinsichtlich unterkritischem Risswachstum erlaubte eine unterstützende Vorhersage der Lebensdauer der untersuchten Probenmaterialien anhand von sogenannten Spannung-Zeit-Wahrscheinlichkeit-Diagrammen, wobei $SrTi_{0,65}Fe_{0,35}O_{3-\delta}$ die beste Performance aller Zusammensetzungen zeigte.

Darüber hinaus erfolgte die Bestimmung der mechanischen Eigenschaften von $SrTi_{0,75}Fe_{0,25}O_{3-\delta}$ bei Hochtemperatur über Doppelringtests bei zwei verschiedenen Belastungsraten, und zwar 1 und 100 N/min. Der scheinbare elastische Modul zeigte ein zeitabhängiges Verhalten. Die auf Basis der experimentellen Daten ermittelte Bruchfestigkeit ist unabhängig von der Belastungsgeschwindigkeit und höher als dieselbe Eigenschaft bei Raumtemperatur. Folglich scheint es, dass $SrTi_{0,75}Fe_{0,25}O_{3-\delta}$ anelastisches Verhalten zeigt, das mit der Sauerstofffreisetzung und/oder Primärkriechen verbunden sein kann.

Poröse $SrTi_{0.75}Fe_{0.25}O_{3-\delta}$ Proben, die repräsentativ für die Anwendung als poröser Substrat für asymmetrische geträgerte Sauerstoff-Permeationsmembranen sein sollen, wurden durch

Foliengießen, Gefriergießen und Phase-Inversion-Gießen hergestellt. Die erste Methode resultierte in einem Material mit einer zufälligen kugelförmigen Porosität, die bei 32% lag. Gefriergießen und Phase-Inversion-Gießen, auf der anderen Seite, führten zu einer kanalförmigen Porenstruktur. Doppelringtests erlaubten die Abschätzung der elastischen Module sowie der Bruchfestigkeit der hergestellten Proben. Außerdem erfolgte die Untersuchung der Anisotropie der mechanischen Eigenschaften gefriergegossener Probe anhand von Drucktests in Abhängigkeit von der Belastungsrichtung. Die geringe mechanische Stabilität der in-plane-Richtung (senkrecht zu den Poren) scheint ein Resultat der Biegung der Porenwände zu sein, wobei ein geringer Wiederstand gegen Risswachstum zu erwarten ist. Akustische Emissionen, die während eines Drucktests aufgenommen wurden, zeigten eine kontinuierliche Schädigung der Porenwände vor dem Bruch der Proben. Dies wurde auch mithilfe einer komplementären in-situ Druckuntersuchung im Rasterelektronmikroskop bestätigt.

Außerdem wurde das Kriechverhalten gepresster, foliengegossener und gefriergegossener $SrTi_{0,75}Fe_{0,25}O_{3-\delta}$ Probe untersucht und die experimentellen Kriechparameter wurden ermittelt. Die Ergebnisse lieferten einen Spannungsexponenten von 2 sowie eine große Primärkriechen-Verformung (zwischen 0,03 und 0,6%). Die Resultate implementieren, dass $SrTi_{0,75}Fe_{0,25}O_{3-\delta}$ eine Kombination von Diffusions- und Versetzungskriechen zeigt.

Band / Volume 437
Characterization of High Temperature Polymer Electrolyte Fuel Cells
Y. Rahim (2018), iii, 162 pp
ISBN: 978-3-95806-359-4

Band / Volume 438
Lattice Boltzmann Simulation in Components of Polymer Electrolyte Fuel Cell
J. Yu (2018), ii, 173 pp
ISBN: 978-3-95806-360-0

Band / Volume 439
Quantitative Luminescence Imaging of Solar Cells
V. Huhn (2018), 155 pp
ISBN: 978-3-95806-363-1

Band / Volume 440
Characterization of Phosphoric Acid Doped Polybenzimidazole Membranes
Y. Lin (2018), II, IV, 140 pp
ISBN: 978-3-95806-364-8

Band / Volume 441
Degradation Study of SOC Stacks with Impedance Spectroscopy
Y. Yan (2018), 135 pp
ISBN: 978-3-95806-367-9

Band / Volume 442
Future Grid Load of the Residential Building Sector
L. Kotzur (2018), xxi, 213 pp
ISBN: 978-3-95806-370-9

Band / Volume 443
Yttriumoxid-Dünnschichten als Tritium-Permeationsbarriere
J. Engels (2018), 252 pp
ISBN: 978-3-95806-371-6

Band / Volume 444
Inverse conditioning of a high resolution integrated terrestrial model at the hillslope scale: the role of input data quality and model structural errors
S. Gebler (2018), xxii, 160 pp
ISBN: 978-3-95806-372-3

Band / Volume 445
Cathode Stability and Processing in Inert Substrate-Supported Solid Oxide Fuel Cells
E. Matte (2018), viii, 178 pp
ISBN: 978-3-95806-373-0

Band / Volume 446
Aging and Degradation Behavior of Electrode Materials in Solid Oxide Fuel Cells (SOFCs)
X. Yin (2018), x, 103 pp
ISBN: 978-3-95806-374-7

Band / Volume 447
TRENDS 2017
Transition to Renewable Energy Devices and Systems
D. Stolten, R. Peters (Eds.) (2018), 206 pp
ISBN: 978-3-95806-376-1

Band / Volume 448
3D simulation of impurity transport in a fusion edge plasma using a massively parallel Monte-Carlo code
J. Romazanov (2018), xvi, 149 pp
ISBN: 978-3-95806-377-8

Band / Volume 449
Projektbericht Adelheid – aus dem Labor heraus in die Lüfte
D. Stolten, R. Peters (Eds.) (2018), xxi, 321 pp
ISBN: 978-3-95806-378-5

Band / Volume 450
Microstructure and Thermomechanical Properties of $SrTi_{1-x}Fe_xO_{3-\delta}$ Oxygen Transport Membranes and Supports
R. Oliveira Silva (2019), vi, 148 pp
ISBN: 978-3-95806-381-5

Energie & Umwelt / Energy & Environment
Band / Volume 450
ISBN 978-3-95806-381-5

Mitglied der Helmholtz-Gemeinschaft

JÜLICH
Forschungszentrum